

2. EXPLANATORY NOTES¹

Shipboard Scientific Party²

INTRODUCTION

Information assembled in this chapter will help the reader understand the basis for our preliminary conclusions and also enable the interested investigator to select samples for further analysis. This information concerns only shipboard operations and analyses described in the site reports in the Leg 207 *Initial Reports* volume of the *Proceedings of the Ocean Drilling Program* (ODP). Methods used by various investigators for shore-based analyses of Leg 207 data will be described in the individual contributions published in the *Scientific Results* volume and in publications in various professional journals.

Authorship of Site Chapters

The separate sections of the site chapters were written by the following shipboard scientists (authors are listed in alphabetical order; no seniority is implied):

Background and Objectives: Erbacher, Mosher
Operations: Malone, Pettigrew
Lithostratigraphy: Bostock, Glatz, Henderiks, Junium, Le Callonnet, MacLeod, Sexton, Thurow
Biostratigraphy: Danelian, Mutterlose, Nishi, Norris, Wise
Paleomagnetism: Ogg, Suganuma
Composite Depths: Bice, Janecek
Sedimentation and Accumulation Rates: Henderiks, Junium, MacLeod, Mutterlose, Sexton
Organic Geochemistry: Forster, Meyers, Sturt
Inorganic Geochemistry: Brumsack, Wilson
Physical Properties: Berti, O'Regan
Downhole Logging: Heidersdorf, Rea

¹Examples of how to reference the whole or part of this volume.

²Shipboard Scientific Party addresses.

Drilling Operations

Three standard coring systems were used during Leg 207, the advanced piston corer (APC), the extended core barrel (XCB), and the rotary core barrel (RCB). These standard coring systems and their characteristics are summarized in the “Explanatory Notes” chapters of various previous *Initial Reports* volumes as well as a number of *Technical Notes*. The Leg 139 *Initial Reports* volume (Davis, Mottl, Fisher, et al., 1992) includes a particularly detailed description. Most cored intervals were ~9.6 m long, which is the length of a standard core barrel. In other cases, the drill string was advanced, or “washed ahead,” without recovering sediments to advance the drill bit to a target depth where core recovery needed to be resumed.

Drilled intervals are referred to in meters below rig floor (mbrf), which are measured from the kelly bushing on the rig floor to the bottom of the drill pipe, and meters below seafloor (mbsf), which are calculated. When the seafloor consists of sediment, the mbrf depth of the seafloor is determined with a mudline core, assuming 100% recovery for the cored interval in the first core. Water depth is calculated by subtracting the distance from the rig floor to sea level from the mudline measurement in mbrf. This water depth usually differs from precision depth recorder measurements by up to several meters. The mbsf depths of core tops are determined by subtracting the seafloor depth (in mbrf) from the core top depth (in mbrf). The resulting core top datums in mbsf are the ultimate reference for any further depth calculation procedures.

Drilling Deformation

When cores are split, intervals in some cores may show signs of significant sediment disturbance, including the concave-downward appearance of originally horizontal bedding, haphazard mixing of lumps of different lithologies (mainly at the tops of cores), fluidization, and flow-in. Core deformation may also occur during retrieval, because of changes in pressure and temperature as the core is raised, and during cutting and core handling on deck.

Curatorial Procedures and Sample Depth Calculations

Numbering of sites, holes, cores, and samples follows the standard ODP procedure. A full curatorial identifier for a sample consists of the leg, site, hole, core number, core type, section number, and interval in centimeters measured from the top of the core section. For example, a sample identification of “207-1257A-1H-1, 10–12 cm,” represents a sample removed from the interval between 10 and 12 cm below the top of Section 1, Core 1 (H designates that this core was taken with the APC system), from Hole 1257A, during Leg 207. Cored intervals are also referred to in “curatorial” mbsf dept. The mbsf depth of a sample is calculated by adding the depth of the sample below the section top and the lengths of all higher sections in the core to the core-top datum measured with the drill string.

In some cases, a sediment core from less than a few hundred mbsf may expand upon recovery (typically 10% in the upper 300 mbsf) and its length may not necessarily match the drilled interval. In addition, a coring gap is typically present between cores, as shown by composite depth construction (see the “Explanatory Notes” chapters in the Leg

138, 177, and 189 *Initial Reports* volumes [Shipboard Scientific Party, 1992, 1999, 2001]). Thus, a discrepancy may exist between the drilling mbsf and the curatorial mbsf depths. For instance, the curatorial mbsf depth of a sample taken from the bottom of a core may be larger than that of a sample from the top of the subsequent core, where the latter corresponds to the drilled core-top datum.

If a core has incomplete recovery, all cored material is assumed to originate from the top of the drilled interval as a continuous section for curation purposes. The true depth interval of the cored interval is not known. This should be considered as a sampling uncertainty in age-depth analysis and correlation of core facies with downhole log signals.

Core Handling and Analysis

General core handling procedures are described in previous *Initial Reports* volumes and the *Shipboard Scientist's Handbook* and are summarized here. Core catcher samples were obtained for biostratigraphic analysis. When the core was cut in sections, whole-round samples were taken for interstitial water analyses, microbiology, gas samples, and physical property measurements. In addition, headspace gas samples were immediately extracted from the ends of cut sections and sealed in glass vials for light hydrocarbon analysis.

Before splitting, whole-round core sections were run through the multisensor track (MST) and thermal conductivity measurements were taken. The cores were then split into working and archive halves (from bottom to top), so investigators should be aware that older material could have been transported upward on the split face of each section. When short pieces of sedimentary rock were recovered, the individual pieces were split with the rock saw and placed in split liner compartments created by sealing spacers into the liners with acetone.

Coherent and reasonably long archive-half sections were measured for color reflectance using the archive multisensor track (AMST). All archive-half sections were run through the cryogenic magnetometer and a digital imaging track system (equipped with a line-scan camera), described visually and by means of smear slides and thin sections, and photographed with both black-and-white and color film. Close-up photographs were taken of particular features for illustrations in site chapters, as requested by individual scientists. The working half was sampled both for shipboard analysis—such as physical properties, carbonate, and bulk X-ray diffraction (XRD) mineralogy—and shore-based studies. Both halves of the core were then put into labeled plastic tubes, sealed, and placed in a cold-storage space on board the ship. At the end of the leg, the cores were transferred from the ship into refrigerated containers and shipped to the ODP Bremen Core Repository in Bremen, Germany.

LITHOSTRATIGRAPHY

Sediment Barrel Sheets

Data obtained during shipboard analysis of each sediment core are summarized on core description forms termed “barrel sheets.” To generate barrel sheets, detailed observations of each core or core section were first recorded on standard ODP visual core description (VCD) forms. Copies of these original, handwritten VCD forms are available from

2. Heavy: >50%–75% of interval is burrowed and/or primary bedding contacts are rare.
3. Moderate: 10%–50% of interval is burrowed and/or primary bedding contacts are common.
4. Slight: <10% of interval is burrowed and/or primary bedding contacts are rarely cut by discrete traces.
5. Absent: no traces observed and/or all primary bedding contacts are preserved.

These levels are illustrated as a grayscale bar in the Bioturbation column (Fig. F3).

Color

During visual core description, sediment color was estimated qualitatively using Munsell Soil Color Charts (Munsell Color Company, 1994). To minimize color changes associated with drying and redox reactions, observations were made soon after each core was split. Munsell color names and a summary of color variation are provided with the lithologic summary and general lithologic description in the Remarks column of each barrel sheet. Quantitative color data were collected using color reflectance spectrophotometry (see “[Color Reflectance Spectrophotometry](#),” p. 7).

Sample Types

The position of samples taken for shipboard sedimentological, paleontological, and chemical analyses are shown in the Sample column. Sample types include interstitial water whole rounds (IW), micropaleontology samples (PAL), smear slides (SS), thin section billets (THS), inorganic carbon (CAR), discrete samples for identification of mineral components using X-ray diffraction (XRD), and whole rounds for either physical properties (WRP) or microbiology (WRB). Depending on lithologic variability, typically one to six smear slides were made per core. In addition, pore water samples were taken at designated intervals and a micropaleontology sample was usually obtained from the core catcher. Inorganic carbon and XRD samples were taken where needed to assess the lithologic composition and components. Additional samples were selected to better characterize lithologic variability in a given interval. Tables summarizing relative abundance of sedimentary components observed in the smear slides and thin sections were generated using a spreadsheet program (Sliders) and are presented with the barrel sheets (see the “[Core Descriptions](#)” contents list).

Remarks

The written description for each core contains a brief overview of both major and minor lithologies present and notable features such as sedimentary structures, fossils, and disturbances resulting from the coring process.

Drilling Disturbance

The extent and style of disturbance introduced during drilling and recovery is shown in the Drilling Disturbance column (Fig. F1), and the symbols used are shown in Figure F3.

fix “-stone” is appended to the dominant size classification (e.g., clay vs. claystone).

4. Sediments composed of sand-sized volcanoclastic grains:
Ash: sediment can be deformed easily with a finger;
Tuff: more consolidated material.

Color Reflectance Spectrophotometry

In addition to visual estimates of color, reflectance of visible light from soft-sediment cores was routinely measured using a Minolta spectrophotometer (model CM-2002) mounted on the AMST. The AMST measures the archive half of each core section and provides a high-resolution stratigraphic record of color variations for visible wavelengths (400–700 nm). Lightness (L^*) values are plotted on the barrel sheets; these values as well as all other color measurements are in the Janus database.

To measure reflectance, freshly split cores were covered with clear plastic wrap and placed on the AMST. Measurements were typically taken at 2.5-cm spacing. The AMST skips empty intervals and intervals where the core surface is well below the level of the core liner but does not recognize relatively small cracks or disturbed areas of core. Thus, AMST data may contain spurious measurements that should be edited out of the data set. Each measurement recorded consists of 31 separate determinations of color reflectance in 10-nm-wide spectral bands from 400 to 700 nm. Additional detailed information about measurement and interpretation of spectral data with the Minolta spectrophotometer can be found in Balsam et al. (1997, 1998) and Balsam and Damuth (2000).

X-Ray Diffraction

Selected samples were taken for qualitative mineral analysis using a Philips PW-1729 X-ray diffractometer with a CuK_α source (40 kV and 35 mA). The goniometer scan was performed from 2° to $70^\circ 2\theta$ for the air-dried samples analyzed during Leg 207. Scan speed was $1.2^\circ/\text{min}$ (step = 0.01° and count time = 0.5 s).

Some samples were decalcified using 10% acetic acid then washed repeatedly with demineralized water, centrifuged, and decanted. The carbonate-free fraction was deflocculated with a 1% Calgon (sodium hexametaphosphate) solution and homogenized in a sonic dismembrator for 1 min. The interactive software package MacDiff (version 4.1.1) (Petschick, 2000) was used to display diffractograms, and identifications are based on multiple peak matches using the mineral database provided with MacDiff. Diffractograms were peak corrected to match the calcite peak at 3.035 Å. In the absence of calcite, no peak correction was applied.

Digital Color Imaging System

Systematic high-resolution line-scan digital core images of the archive half of each core were obtained using the Geotek X-Y digital imaging system (Geoscan II). This system collects digital images with three line-scan charge-coupled device arrays (1024 pixels each) behind an interference filter to create three channels (red, green, and blue). The image resolution is dependent on the height of the camera and width of the core. The standard configuration for the Geoscan II produces 300

dots per inch (dpi) on an 8-cm-wide core, with a zoom capability up to 1200 dpi on a 2-cm-wide core. Synchronization and track control are better than 0.02 mm. The dynamic range is 8 bits for all three channels. The Framestore card has 48 MB of onboard random access memory (RAM) for the acquisition of images with an ISA interface card for personal computers. After cores were visually described, they were placed in the digital imaging system and scanned. A spacer holding a neutral gray color chip and an identifying label was scanned with each section. Output from the digital imaging system includes a Windows bitmap (.BMP) file and a Mr.Sid (.SID) file for each section scanned. The bitmap file contains the original data with no compressional algorithms applied, whereas the Mr.Sid files contain extensive compressional algorithms. The digital imaging system was calibrated for black and white approximately every 12 hr.

Because sediments and sedimentary rocks ranging from black to white were recovered during Leg 207, sometimes it was necessary to adjust the aperture of the imaging system to prevent resolution loss resulting from over- or underexposure. To minimize artifacts in composite images related to changes in the aperture, we changed the f/stop only when light-colored intervals oversaturated the sensors or when there was a change to markedly darker lithologies that extended over several cores. In exceptional cases where very light and very dark lithologies were present in the same core section, the core section was scanned twice—once each with an appropriate f/stop for the light and dark intervals, respectively.

BIOSTRATIGRAPHY

Preliminary age assignments were based on biostratigraphic analyses of calcareous nannofossils, planktonic foraminifers, and radiolarians. At multiply cored sites, efforts were focused on Hole A, thereby allowing greater sampling density and development of a detailed shipboard biostratigraphy. Age constraints of calcareous nannofossil datums were determined by observing from one to six samples per core section (sampling spacing = 0.25–1.5 m) as well as core catcher samples. Planktonic foraminifers were examined in one sample per core section from Hole A (sampling density = ~1.5 m) in addition to core catcher samples from all holes. Radiolarians were studied mainly in core catcher samples. The preservation, abundance, and zonal assignment for each microfossil group as well as for selected samples were recorded in the stratigraphic site summary sheets and entered into the Janus database.

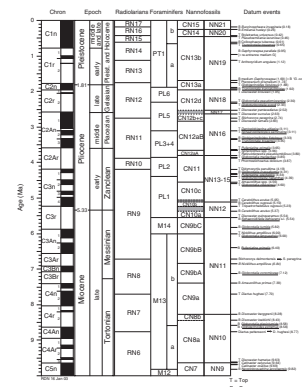
Recognition of Cenozoic Critical Intervals

In the Cenozoic, much emphasis has been placed on two critical intervals: the Eocene/Oligocene (E/O) boundary and the Paleocene/Eocene (P/E) boundary. Biostratigraphic indicators for each of these events are discussed below.

Eocene/Oligocene Boundary

The lower Oligocene is zoned in most detail by calcareous nannofossils (Fig. F5), although the E/O boundary is recognized by the last occurrence (LO) of the planktonic foraminifer genus *Hantkenina*. The E/O boundary is present in uppermost Chron C13r at the planktonic foraminifer

F5. Nannofossil, foraminifer, and radiolarian zonations, p. 59.



minifer Zone P16/P18 boundary and in the middle of calcareous nannofossil Subzone CP16a. We did not recognize planktonic foraminifer Zone P17 of Berggren et al. (1995a) because of taxonomic and preservational problems associated with identification of the LO of *Cribohantkenina inflata*. Calcareous nannofossil datum levels within 2 m.y. of the E/O boundary (33.7 Ma) include the first occurrence (FO) of *Reticulofenestra umbilica* (31.7 Ma), the FO of *Ericsonia formosa* (32.9 Ma), and the start of the *Ericsonia subdisticha* acme (33.3 Ma). The onset of the *Ericsonia obruta* acme (33.7 Ma) coincides with the E/O boundary. The planktonic foraminifer *Pseudohastigerina* (top = 32.0 Ma) is considered a reliable datum for the lowermost Oligocene. The uppermost Eocene is easily determined by the presence of the calcareous nannofossils *Discoaster saipanensis* (top = 34.0 Ma) and *Discoaster barbadiensis* (top = 34.2 Ma) as well as by planktonic foraminifers *Turborotalia cerroazulensis* (top = 33.8 Ma) and *Globigerinatheka* spp. (top = 34.3 Ma). The base of the *Theocyrtis tuberosa* radiolarian zone (RP20) has been approximated to 32.8 Ma (Sanfilippo and Nigrini, 1998).

Paleocene/Eocene Boundary

The P/E boundary has, until recently, been placed at the planktonic foraminifer Biozone P5/P6 boundary, which is found in the middle part of calcareous nannofossil Zone NP10 (Subzone CP9a) (Aubry et al., 1996). In 2000, the International Geological Correlation Programme Project 308 membership (*Paleocene/Eocene Events in Space and Time*) voted to recognize the carbon isotope excursion associated with the Paleocene–Eocene Thermal Maximum (PETM) as the defining criterion for identifying the P/E boundary. For Leg 207, we will adhere to this definition of the P/E boundary.

The P/E boundary, as defined by the carbon isotope excursion, can be approximated by a series of calcareous microfossil datums (Fig. F5). These events include a major extinction event among benthic foraminifers (including *Gavelinella beccariiiformis*, *Aragonia velascoensis*, and *Osangularia velascoensis*) precisely at the boundary. The boundary can also be approximated by the presence of the planktonic foraminifer “excursion fauna,” which includes *Acarinina africana*, *Acarinina sybiaensis*, and *Morozovella allisonensis* (Kelly et al., 1996, 1998). The planktonic foraminifer *Pseudohastigerina wilcoxensis* and large specimens of *Chiloguembelina wilcoxensis* also have FOs close to the boundary (Speijer et al., 1997). The interval ~500–700 k.y. above the P/E boundary is marked by the LOs of *Morozovella velascoensis* (marking the top of planktonic foraminifer Zone P5) and *Morozovella occlusa* as well as the FOs of *Morozovella gracilis* and *Acarinina wilcoxensis*.

The extinction of the calcareous nannofossil genus *Fasciculithus* occurs not far above the boundary, and the lineage *Rhombaster–Tribrachiatatus* evolves somewhat farther above the boundary; the FO of *Campylosphaera eodela* is observed shortly below. Thus, from a biostratigraphic point of view, the P/E boundary falls in planktonic foraminifer Biozone P5 and in calcareous nannofossil Biosubzone CP8b and Biozone NP9.

During drilling, however, it is desirable to know from core catcher samples when the P/E boundary is being approached and to confirm its capture in a core as accurately as possible in order to determine whether to take whole-round interstitial water samples. The planktonic foraminifers *M. velascoensis* and *M. occlusa* suggests proximity to the P/E boundary, whereas members of the excursion fauna indicate the sample comes from the ~200-k.y. interval immediately following the boundary.

The benthic foraminifers *A. velascoensis*, *G. beccariiiformis*, or *O. velascoensis* shows that the boundary has been passed and is either in the recovered core or is unconformable. For calcareous nannofossils we can detect the dominance change or crossover among the nannofossils downhole from *Zygrhablithus bijugatus* and *Neochiastozygus junctus* (whose high abundances extend some distance above the boundary in Zone NP9) to the abundant and varied fasciculiths below (see Bralower, 2002, regarding the evolutionary behavior of the latter two taxa). This technique worked so well that we have further subdivided Martini (1971) Zone NP9 into an upper NP9b and a lower NP9a Subzone based on this crossover in dominance/abundance (see Fig. F5). As further indicated in that figure, we have also made a similar division of the number-coded Okada and Bukry (1980) scheme in Subzone CP8b and divided it into Subsubzones CP8bB and CP8bA.

All of these biostratigraphic events are present in the long interval of Chron 24r. According to our timescale (Cande and Kent, 1995), this interval of uniform reversed polarity has a duration of 2.557 m.y. Recent cyclostratigraphic work (Norris and Röhl, 1999; Röhl et al., 2000) has shown that the carbon isotope excursion, and therefore the P/E boundary, is ~1 m.y. above the top of Chron C25n. Thus, it has an age of 55 Ma according to the Leg 207 timescale.

Hole 1051A (Leg 171B), in the western North Atlantic, is the only recovered P/E boundary section in which radiolarians have been studied (Sanfilippo and Blome, 2001). In this mid-latitude fauna, many tropical zonal markers are missing and others are diachronous with their tropical equivalents. There is no gross change in the composition of the fauna and only a minor increase in the number of FOs and LOs across the PETM and P/E boundary.

Sanfilippo and Nigrini (1998) established the stratigraphic sequence of the 70 lowest and highest radiolarian occurrences in a 10-m.y. interval spanning the P/E boundary from the Paleocene *Bekoma campechensis* Zone (RP6) to the upper part of the lower Eocene *Buryella clinata* Zone (RP8) and related them to the calcareous nannofossil zonation. Although none of their investigated tropical sequences contained the actual P/E boundary, they determined that there are six reliable, easily recognized, and potentially useful radiolarian FOs that approximate the P/E boundary: *Calocyclas castum*, *Theocotylissa auctor*, *Lamtonium fabaeforme*, *Podocyrtilis (Podocyrtilis) papalis*, *Giraffospyris lata*, and *Phormocyrtilis turgida*.

Recognition of Cretaceous Critical Intervals

In the Cretaceous, “critical boundaries” include the following:

1. The Cretaceous/Tertiary (K/T) boundary (65.5 Ma);
2. The mid-Maastrichtian (~69 Ma); and
3. Two oceanic anoxic events (OAEs), OAE 3 (~83.5–89.0 Ma) and OAE 2 (~97.6–93.5 Ma).

Biostratigraphic indicators for each of these events are discussed below.

Cretaceous/Tertiary Boundary

The K/T boundary is marked by one of the largest mass extinctions in the last 200 m.y. of Earth’s history. The extinction level is about half-way through Magnetochron C29r and ~250 k.y. below the base of

Chron C29n. The top of the Maastrichtian is recorded in the extinction of ~95% of the planktonic foraminifers, including the globotruncanids, rugoglobigerinids, and the large serially coiled planktonic foraminifers. The nearly exclusive presence of minute planktonic foraminifers, typically <63 µm in diameter, are characteristic of the first Paleogene sediments above the K/T boundary. These Danian species include *Parvulorugoglobigerina eugubina*, *Guembelina cretacea*, and *Heterohelix globulosa*. Previous zonations have recognized a Zone P0 dominated by *G. cretacea* between the K/T boundary and the first appearance of *P. eugubina* (~64.97 Ma). However, reexamination of the classic K/T boundary section at el Kef, Tunisia, demonstrated that rare specimens of *P. eugubina* are present directly above the extinction level of the Cretaceous foraminifers, suggesting that Zone P0 reflects an increased abundance of *P. eugubina* rather than its evolutionary first appearance (Norris et al., 1999). Calcareous nannofossils also display a significant extinction across the K/T boundary, which is bracketed by the FOs of *Cruciplacolithus tenuis* (64.5 Ma) and *Cruciplacolithus primus* (64.8 Ma) above the boundary and the FO of *Micula prinsii* (65.4 Ma) below the boundary.

Mid-Maastrichtian Interval

Widespread and presumably related isotopic, sedimentological, and paleontological changes are concentrated in the middle of the Maastrichtian (e.g., Barrera and Savin, 1999; Frank and Arthur, 1999; MacLeod and Huber, 2001). However, there are currently no established criteria for defining the interval and erecting a definition poses some challenges. Some associated changes are graded over millions of years (e.g., high-latitude cooling), others are markedly diachronous (e.g., the LO of bathyal inoceramids), others are not expressed in all areas (e.g., carbon isotopic excursions among benthic foraminifers), and still others are poorly dated (e.g., the collapse of rudist reefs). These uncertainties notwithstanding, the decline in abundance among inoceramids can first be resolved in the upper part of Chron 31r in the subtropical North Atlantic and Tethys. Except for *Tenuipteria*, inoceramids disappear in Chron 31n. This interval coincides with diversification among Tethyan planktonic foraminifers, increased isotopic gradients among planktonic foraminifers on Blake Nose, and proposed changes in the North Atlantic carbonate compensation depth. Thus, during Leg 207, mid-Maastrichtian changes are expected to be seen in the upper portion of Chron 31r, in Zone CC25, and near the FO datum of the planktonic foraminifer *Abathomphalus mayaroensis*.

Santonian/Campanian and Turonian/Coniacian Boundaries (Oceanic Anoxic Event 3)

The interval between the base of the Coniacian and the base of the Campanian marks an interval of elevated deposition of organic carbon in the tropical Atlantic and South Atlantic that is sometimes referred to as OAE 3. The lower Campanian is defined by a series of nannofossil events that includes the LO of *Marthasterites furcatus* (~80.6 Ma) and the FOs of *Ceratolithoides verbeekii* (82.0 Ma), *Aspidolithus parvus constrictus* (82.5 Ma), and *Aspidolithus parvus parvus* (83.4 Ma). The top of the Santonian is approximated by the first appearance of the nannofossil *Arkhangelskiella cymbiformis* (~83.5 Ma). The planktonic foraminifer *Dicarinella asymetrica* (83.0 Ma) has its LO just above the base of the Campanian, whereas the FO of *Globotruncana elevata* (84.8 Ma) marks the

middle of the Santonian. We did not find *D. asymetrica* at any Leg 207 site and resorted to using alternative markers to approximate Santonian Zone KS24. In particular, we used the presence of *Rosita fornicata* to mark Santonian-age black shales. However, *R. fornicata* is reported to range into the middle Coniacian by some authors (e.g., Premoli Silva and Sliter, 1999), whereas others extend its range only to the base of the Santonian (e.g., Robaszynski et al., 1984). Hence, it is entirely possible that samples we identify as Santonian may represent the middle or upper Coniacian.

The Turonian/Coniacian boundary (89.0 Ma), which approximates the onset of OAE 3 is slightly predated by the FO datum of *M. furcatus* (89.3 Ma). The FO of *Dicarinella concavata* (89.5 Ma) can also be used to recognize the uppermost Turonian. We also used the FO of *Dicarinella primitiva* to approximate the Turonian/Coniacian boundary. However, there is some disagreement in the lowest stratigraphic range of *D. primitiva* between recently published biostratigraphies, with some authors extending the FO datum into the upper Turonian (Premoli Silva and Sliter, 1999), whereas others infer a range only to the base of the Coniacian (Robaszynski et al., 1984). Hence, it is possible that any disagreements in age between planktonic foraminifers and calcareous nannofossils may be due to uncertainties in the published ages of various datums.

Oceanic Anoxic Event 2

OAE 2 falls in the lower part of calcareous nannofossil Zone CC11 and the upper part of Zone CC10. The boundary itself is marked by the FO of *Quadrum gartneri* (93.2 Ma). The upper Cenomanian range marker *Lithraphidites acutus* was observed only once on board the ship in Leg 207 sediments. Its LO is closely approximated, however, by the LOs of *Corollithon kennedyi* and *Axopodorhabdus albianus*. Although rare themselves in this part of the section, they, particularly the latter, were used in this study. As such, the LO of *A. albianus* provided a useful means to subdivide Zone CC10, which we propose here as a lower Subzone CC10a and an upper Subzone CC10b (see Fig. F5). The lowermost Turonian is marked by the LOs of the planktonic foraminifers *Marginotruncana renzi* (92.5 Ma) and *Helvetoglobotruncana helvetica* (93.0 Ma). Unfortunately, we did not find any specimens of *H. helvetica* at Leg 207 sites and so have approximated the OAE 2 interval based on the following alternate criteria: (1) the absence of rotaliporids; (2) the presence, sometimes exclusively, of *Whiteinella archaeocretacea*; and (3) the disappearance of virtually all planktonic foraminifers in the “dead zone,” which is associated with what we assume are the most extreme anoxic conditions during the OAE. The upper Cenomanian is marked by the LO of *Rotalipora cushmani* (94.0 Ma) and the presence of *Rotalipora greenhornensis* and *Whiteinella* sp. Whiteinellids (mostly four-chambered *Whiteinella baltica*) range as low as the middle *R. cushmani* Zone (Zone KS19). At Leg 207 sites, it also appears that large inflated forms of *H. globulosa* range as low as the Cenomanian/Turonian boundary or perhaps into the lower Turonian part of the *W. archaeocretacea* Zone (KS20).

Zonal Schemes and Taxonomy

Calcareous Nannofossils

The zonal scheme of Martini (1971) was used for Cenozoic calcareous nannofossil biostratigraphy. This zonation represents a general framework for the biostratigraphic classification of mid- to low-latitude nannofossil assemblages and is presented in Figure F5. Ages and sources for Cenozoic calcareous nannofossil datums are presented in Table T1. The age estimates presented are all adjusted to the timescale from Leg 207. The zonation of Bukry (1973, 1975) (zonal code numbers CN and CP added and modified by Okada and Bukry, 1980) is also shown for reference. As explained previously in “Paleocene/Eocene Boundary,” p. 9, in “Recognition of Cenozoic Critical Intervals,” we have further subdivided herein Zone NP9 of the Martini (1971) zonal compilation scheme and Subzone CP8b of the Okada and Bukry zonation.

The zonal schemes of Sissingh (1977) (CC Zones), as modified by Perch-Nielsen (1985) and Burnett (1999) (UC Zones), were used for the Upper Cretaceous (Table T2). Those of Roth (1978, 1983) (NC Zones) with subdivisions by Bralower et al. (1993) were used for the Lower Cretaceous (Table T2). As noted previously in “Oceanic Anoxic Event 2,” p. 12, in “Recognition of Cenozoic Critical Intervals,” we have further subdivided Zone CC10 of the upper Cenomanian into Subzones CC10a and CC10b.

All of these zonation schemes represent a general framework for the biostratigraphic classification of mid- to low-latitude nannofossil assemblages and are shown in Figure F5. Cenozoic nannofossil taxonomy follows that of Perch-Nielsen (1985) and Bown (1999). Cretaceous nannofossil taxonomy follows that used in Bown (1999), where full taxonomic lists can be found.

Planktonic Foraminifers

The tropical planktonic foraminifer zonal scheme (N and P zones) for the Cenozoic follows Berggren et al. (1995b) and is illustrated in Figure F5. Ages and sources for Cenozoic planktonic foraminifer datums are presented in Table T3. Cenozoic taxonomic concepts selectively follow Postuma (1971), Kennett and Srinivasan (1983), Bolli and Saunders (1985), Toumarkine and Luterbacher (1985), Spezzaferri and Premoli Silva (1991), Chaisson and Leckie (1993), Leckie et al. (1993), Spezzaferri (1994), Pearson (1995), Berggren and Norris (1997), Chaisson and Pearson (1997), Pearson and Chaisson (1997), Norris (1998), and Olsson et al. (1999). Genus-species combinations generally follow those rules used by Berggren et al. (1995b), with few modifications. The zonation used for Cretaceous planktonic foraminifers is based on the tropical zonal schemes of Caron (1985) and Sliter (1989) (KS Zones) with modifications by Bralower et al. (1993, 1995, 1997) and Premoli Silva and Sliter (1994, 1999) (Fig. F5). Age estimates for planktonic foraminifer datum markers were obtained from Erba et al. (1995), Bralower et al. (1997), and Premoli Silva and Sliter (1999) (Table T4). Cretaceous taxonomic concepts are based on Longoria (1974), Robaszynski et al. (1979, 1984), Leckie (1984), Caron (1985), Nederbragt (1990, 1991), and Petrizzo (2000).

T1. Cenozoic nannofossil datum events, p. 73.

T2. Cretaceous nannofossil datum events, p. 75.

T3. Cenozoic foraminifer datum events, p. 76.

T4. Cretaceous foraminifer datum events, p. 79.

Radiolarians

Leg 207 Cenozoic radiolarian biostratigraphy is based largely on the radiolarian zonation and code numbers that are tied to the geomagnetic polarity timescale (GPTS) of Cande and Kent (1995) and documented by Sanfilippo and Nigrini (1998) (Fig. F5). Supplemental markers, also derived from Sanfilippo and Nigrini (1998), are used whenever possible and are correlated with the data supplied by calcareous nannofossils. Primary and supplemental datums are listed in Table T5 and illustrated in Figure F5. Upper Cretaceous radiolarian biostratigraphy (Table T6) is based on the zonation of Sanfilippo and Riedel (1985), O'Dogherty (1994), and Erbacher and Thurow (1998).

Methods of Study

Calcareous Nannofossils

Calcareous nannofossils were examined on smear slides using standard light microscope techniques under crossed nicols and transmitted light at 1000× magnification. The following abbreviations are used to describe nannofossil preservation:

- G = good (little or no evidence of dissolution and/or recrystallization; diagnostic characteristics fully preserved).
- M = moderate (dissolution and/or secondary overgrowth; partially altered primary morphological characteristics; most specimens were identifiable to the species level).
- P = poor (severe dissolution, fragmentation, and/or overgrowth; primary morphological characteristics largely destroyed; specimens often cannot be identified at the species and/or generic level).

Abundances of calcareous nannofossil were estimated and their abundance levels recorded as follows:

- A = abundant (the taxonomic category constitutes >10% of the total assemblage).
- C = common (the taxonomic category constitutes from 1% to 10% of the total assemblage).
- F = few (the taxonomic category constitutes from 0.1% to <1% of the total assemblage).
- R = rare (the taxonomic category constitutes <0.1% of the total assemblage).
- B = barren.

Foraminifers

Foraminifers from unlithified ooze were soaked in a 3% solution of hydrogen peroxide (with a small amount of Calgon added), warmed on a hot plate, and washed with tap water over a 45- μ m sieve. Semilithified ooze and chalk were first partially fragmented by hand then soaked in hydrogen peroxide and Calgon before washing. Hard chalk was pounded with a hammer into pea-sized chunks and boiled on a hot plate for 1 or 2 min in a combination of either peroxide and Calgon or peroxide and dishwashing detergent.

T5. Cenozoic Radiolarian datum events, p. 80.

T6. Late Cretaceous radiolarian datums and zones, p. 84.

Repeated boiling and washing over a sieve was necessary to disaggregate many black shale samples. We tried the following methods, all with limited success:

1. We placed samples in a freeze-dryer for ~12–24 hr and then soaked them in peroxide and detergent.
2. We freeze-dried samples as above and soaked them in either methanol, acetone, or Quaternary-O (an industrial detergent).
3. We boiled samples in detergent and peroxide and then scrubbed the rock fragments through a 710- μm screen over a 45- μm screen.

Of these methods, none produced consistently high-quality results. Freeze-drying worked extremely well with clay-rich Albian samples from Site 1258 but did little to improve sample preparation in most organic-rich black shale samples. Acetone proved to be the best solvent but was not effective in separating clay from foraminifers. Boiling in a detergent/peroxide mixture was used the most, but even this method often required five or six washing/soaking/boiling cycles to remove the majority of the clay fraction. The use of 30% peroxide was effective after several washing cycles but contributed to severe dissolution of the foraminifers. We had three major problems:

1. The foraminifers are frequently coated with a tarlike organic fraction that is difficult to remove by standard washing procedures, even with repeated wetting/drying cycles.
2. Many samples contain thin diagenetic calcite or phosphate seams that partly cement the foraminifers.
3. Layers of foraminifer sands interbedded with black shales are strongly cemented with calcite spar.

We do not expect to be able to extract foraminifers in calcite or phosphate cements during postcruise work, but it may be possible to remove the organic fraction using turpentine, bleach, and dry-cleaning solution.

All samples were dried in a low-temperature oven at ~50°C. Species identification for planktonic foraminifers was generally made on the >250- and >150- μm size fractions. Benthic foraminifers were not examined in detail except for the interval around the P/E boundary, where the ranges of species that become extinct near the PETM were noted.

We did not attempt to estimate relative abundances except in a general nonquantitative fashion. Instead, we noted the presence or absence of the major marker species and the distinctive or dominant species in a sample. The pressure of processing samples in a timely fashion prevented detailed and comprehensive study of all samples. Some samples were examined only to identify the biozone marker species, whereas others were described more comprehensively to give the reader a sense for the species diversity and composition present in each zone.

Preservation status of the planktonic and benthic foraminifers was estimated as follows:

- Glassy = very good (no evidence of overgrowth, infilling, dissolution, or abrasion; dry tests translucent. Specimens did not necessarily have to be completely clean in our samples to be described as “glassy”).
- G = good (little evidence of overgrowth, dissolution, or abrasion).

- M = moderate (calcite overgrowth, dissolution, or abrasion were common but minor).
- P = poor (substantial overgrowth, dissolution, or fragmentation).
- B = barren (no planktonic foraminifers present).

We also use the informal designation “rocks” for samples where 80%–90% of the particles in a sample are unidentifiable pieces of rock.

Radiolarians

Core catcher samples were disaggregated by gentle boiling in a solution of 10% H₂O₂ and ~5 g of tetrasodium pyrophosphate. The solution was passed through a 63- μ m sieve. Calcareous components were dissolved by adding a 10% solution of hydrochloric acid and sieving again. A strewn slide was prepared by pipetting the microfossils onto a microscope slide, allowing the water to evaporate, adding a drop or two of xylene and some Norland optical adhesive to the slide, and covering the slide with a 22 mm \times 40 mm glass coverslip.

Overall radiolarian abundances were determined based on strewn-slide evaluation at 100 \times , using the following conventions:

- A = abundant (>100 specimens per slide traverse).
- C = common (51–100 specimens per slide traverse).
- F = few (11–50 specimens per slide traverse).
- R = rare (1–10 specimens per slide traverse).
- T = trace (<1 specimen per slide traverse).
- B = barren (no radiolarians in sample).

Preservation was recorded as follows:

- G = good (majority of specimens complete, with minor dissolution, recrystallization, and/or breakage).
- M = moderate (minor but common dissolution, with a small amount of breakage of specimens).
- P = poor (strong dissolution, recrystallization, or breakage; many specimens unidentifiable).

PALEOMAGNETISM

Magnetostratigraphy, when coupled with biostratigraphic control, provides high-resolution correlation among sites and a precise calibration to the absolute timescale. Paleomagnetic vectors indicate the history of plate rotation and paleolatitude motion of the site, and magnetic characteristics provide insight into the mineralogy, preferential orientation, and grain size of remanence carriers.

Paleomagnetic investigations for Leg 207 had a shipboard and a shore-based phase. The measurements performed aboard the *JOIDES Resolution* concentrated on a high-resolution survey of the natural remanent magnetization (NRM) of archive-half core sections before and after alternating-field (AF) demagnetization and on low-field magnetic susceptibility (*k*) measurement. Approximately 2000 core sections were analyzed.

The shore-based program consisted of progressive thermal demagnetization of ~800 discrete minicores at the paleomagnetism laboratory at the University of Munich, Germany. The discrete samples required

shore-based analysis because sediment sample magnetizations are too weak to be measured reliably with shipboard equipment and the extensive core flow did not allow time for these procedures. In addition to revealing a more reliable magnetostratigraphy at each site, the detailed thermal demagnetization of these discrete samples allowed insight into the magnetic properties and magnetic mineralogy of the sediments and a determination of paleolatitudes for plate motion studies. The combined results for magnetostratigraphy are incorporated in the “Paleomagnetism” sections in each site chapter.

Whenever possible, we offer an interpretation of the magnetic polarity, with the naming convention following that of correlative Late Cretaceous and Cenozoic anomaly numbers prefaced by the letter C (e.g., Tauxe et al., 1984; Cande and Kent, 1995). Normal polarity subchrons are referred to by adding suffixes (e.g., C24n.n1 and C24n.n2) that increase with age. Assignments of polarity chrons are constrained by the associated biostratigraphy and by characteristic patterns of relative thickness in the sedimentary record.

The ages of the polarity intervals used during Leg 207 are modified from the Berggren et al. (1995b) composite of magnetic polarity timescales calibrated to marine microfossil biostratigraphy (Table T7). The Leg 207 magnetic polarity timescale is summarized in Figure F5.

For each hole, tabulated and annotated paleomagnetic measurements for each discrete sample and a summary of the preliminary polarity interpretations with graphical representations are included.

Shipboard Measurements and Equipment

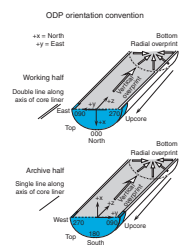
The standard ODP coordinate system was used, where +x is the vertical upward direction to the split surface of archive halves or 0° declination in core coordinates, +y is the direction to the left along the split-core surface when looking upcore or 90° declination in core coordinates, and +z is the downcore direction or 90° inclination in core coordinates (see Fig. F6).

Remanent magnetization was measured using the shipboard long-core cryogenic magnetometer equipped with direct-current superconducting quantum interference devices (DC SQUIDS) (2-G Enterprises model 760R) and an in-line automated AF demagnetizer capable of reaching a peak field of 80 mT. Continuous core measurements were made at 5- to 10-cm intervals. An additional 20-cm header and trailer distance allows future deconvolution of the core data. The pickup coils of the cryogenic magnetometer measure the core over an interval of a little more than 30 cm, although 85% of the remanence is sensed from a 20-cm width. Because of this window size and the 5- to 10-cm sampling intervals, adjacent measurements made on Leg 207 cores are not strictly independent. Measurements within 5 cm of core and section ends, within 5 cm of contacts between rotated blocks, and within intervals of drilling-related core disturbance were removed during data processing. In addition, the upper 20 cm of each core that commonly displayed spurious high-intensity magnetization or downhole contamination and the upper 5 cm of each section that was influenced by magnetization (blue-colored end cap) were excluded. The magnetization of the core liner itself was removed by applying a holder-tray correction to each run.

The background noise of the cryogenic magnetometer seems to be amplified by the ship’s movement compared to shore-based instruments; it was measured by running empty holder trays to be $\sim 3 \times 10^{-5}$

T7. Late Cretaceous–Cenozoic magnetic polarity timescale, p. 85.

F6. Paleomagnetic orientation system, p. 65.



A/m, assuming a measured volume of $\sim 100 \text{ cm}^3$. The relatively large volume of core material in the sensing region normally compensates for the relatively high background noise; however, for the chinks that dominated the stratigraphy at Leg 207 sites, more than one-half of the sediment recovered was measured to be $< 5 \times 10^{-5} \text{ A/m}$ and was therefore considered to be too near the instrument noise level to be useful for polarity determinations. In contrast, the shore-based cryogenic magnetometer enabled an extra order of magnitude sensitivity for the minicores of 12-cm^3 volume.

Measurements of NRM and stepwise AF demagnetization were performed on all archive halves longer than 20 cm. More than 6000 runs were carried out on the shipboard magnetometer. Because AF demagnetization of the archive half was conducted mostly to remove the soft magnetic overprint that was acquired during the drilling process, field strengths were limited to 20 mT to avoid erasing the entire primary NRM component. Sections were measured at NRM, 10- and 15-mT AF demagnetization steps, with an additional 20-mT step applied if core flow permitted it. The 10-mT step appeared to be effective in removing extraneous overprints induced during the drilling process. In general, the additional 20-mT demagnetization step did not significantly alter the magnetic direction obtained at the prior 15-mT step for the majority of the sediment types.

The orientations of APC cores (only used for the uppermost cores in Hole 1257A) were recorded using the Tensor tool (Tensor Inc., Austin, Texas). The instrument has a three-axis fluxgate magnetometer that records the orientation of the double lines scribed on the core liner with respect to magnetic north. The critical parameters for core orientation are the inclination angle (typically $< 2^\circ$) and the angle between magnetic north and the double line on the core liner, known as the magnetic tool face angle. The Tensor tool readings were recorded continuously at 30-s intervals, downloaded to a computer, and analyzed once the tool was back on deck. Orientation of core declinations is of particular importance in magnetostratigraphic interpretation of sediments from equatorial regions, where the paleomagnetic inclination is close to zero. APC coring and associated Tensor tool orientation is limited to relatively soft sediment intervals, whereas every core drilled during Leg 207, except the uppermost ones in Hole 1257A, were from non-oriented XCB and RCB cores in harder sedimentary rocks.

Magnetic susceptibility was measured for each whole-core section as part of the MST analysis (see "**Multisensor Track Measurements**," p. 33, in "Physical Properties"). Susceptibility is measured on the MST using a Bartington Instruments MS2 susceptibility meter coupled to a MS2C sensor coil with a diameter of 8.8 cm operating at 0.565 kHz. The sensor was set on SI units, and the data were stored in the Janus database in raw meter units. The sensor coil is sensitive over an interval of $\sim 4 \text{ cm}$ (half-power width of the response curve), and the width of the sensing region corresponds to a volume of 166 cm^3 of cored material. To convert raw instrument units to true SI volume susceptibilities, these values should be multiplied by 10^{-5} and then multiplied by a correction factor to account for the actual volume of material that passed through the susceptibility coils. Except for measurements near the ends of each section, the correction factor for a standard full ODP core is ~ 0.68 . The end effect of each core section is not adequately corrected using this procedure.

Shipboard Polarity Interpretations: Data Filtering and Inclination Clusters

All recovered sediment pieces from XCB and RCB cores have unknown horizontal rotations. The usage of magnetic declination was limited to the few APC cores in the uppermost portion of Hole 1257A. Therefore, our interpretations of characteristic magnetic polarity rely on measurements obtained from within continuous sediment intervals that exceed 15 cm in length with no suspected interblock rotations. These intact segments yield at least one measurement positioned at least 5 cm from an adjacent block having relative rotation. For this purpose, each intact interval was logged in each analyzed section, and we filtered out all measurements that did not meet these criteria. All measurements from the upper 20 cm of each core were omitted because these were generally contaminated with downhole displaced sediment or anomalous intensity spikes in drill slurry.

All 15- and 20-mT measurements less than the background noise level of the cryogenic magnetometer (3×10^{-5} A/m) were filtered from the block-data file, and all measurements $<5 \times 10^{-5}$ A/m are considered unreliable indicators of polarity. These low-intensity filters imply that the demagnetized data from the majority of light-colored chinks, which constitute more than half of the Campanian–middle Eocene facies, yielded directions that we considered to be unreliable. Indeed, all shipboard measurements from several entire cores failed this threshold. The signal-to-noise ratio of each of the remaining intact blocks was enhanced by employing a three-point moving mean through adjacent data measurements.

In most shipboard magnetostratigraphy interpretations, polarity zones are identified by stratigraphic clusters of positive or negative magnetic inclinations. For sites located north of the paleoequator, these are respectively associated with normal polarity or reversed polarity chrons but have an opposite association for sites south of the paleoequator. The Leg 207 sites are between 9° and 10°N latitude. Global plate reconstructions generally indicate that South America has experienced a small amount of northward drift with negligible plate rotation since the Early Cretaceous (C.R. Scotese, pers. comm., 2002); therefore, pre-Oligocene paleolatitudes of the Leg 207 sites were projected to be closer to the paleoequator.

During Leg 207, the filtered pass-through cryogenic measurements generally consisted of three broad classes of stratigraphic clustering of inclinations: (1) uniformly positive, (2) uniformly negative, or (3) random mixing of positive and negative. Stratigraphic intervals dominated by each class were generally consistent among the different holes at a site after correcting to composite depth (the meters composite depth [mcd] scale). For shipboard estimates of magnetic stratigraphy, we assumed a model in which the original polarity has a variable persistent overprint of present-day north-directed polarity and that clusters of negative inclination correspond to polarity zones of reversed polarity. These shipboard polarity interpretations of these three classes and the associated fitting to polarity chrons were implicitly based on an optimistic assumption that the Leg 207 sites had been north of the paleoequator during the latest Cretaceous and early Cenozoic. Therefore, Class 1 was considered either to be a primary normal polarity or a dominance by present-day overprinting, Class 2 was assigned as reversed polarity, and Class 3 was considered to indicate reversed polarity with variable overprinting by the normal polarity present-day field.

The rate of core flow coupled with the observed ineffectiveness of additional progressive demagnetization by AF methods to significantly change the declination-inclination vectors of most lithologies precluded using sample-by-sample analysis of demagnetization behavior to evaluate removal of overprints and relative rotations of magnetic vectors as clues to the underlying magnetic polarity. In general, for a site located north of the paleoequator, the magnetic vectors of a normal polarity sample would display minimal directional change during AF demagnetization and a normal polarity interval would display a high degree of inclination clustering near 0° to $+20^\circ$. In contrast, a reversed polarity sample might display significant directional change during partial removal of the present-day overprint and a reversed polarity interval might be characterized by a significant scatter in inclinations toward relatively steep downward to low-angle negative (upward) inclinations. This simplified model of ideal magnetic behavior upon AF demagnetization was implicit in our association of inclination classes with polarity zones.

However, the near-equatorial position and the uncertainty in the Cretaceous–Eocene paleolatitudes of the Leg 207 sites and the lack of response of some sediment lithologies to AF demagnetization precluded using magnetic inclination as a reliable indicator of polarity. Therefore, we systematically drill-pressed an extensive suite of minicores to provide stratigraphic coverage of the Campanian–Eocene at each site.

Shore-Based Measurement and Procedures

Discrete samples were collected during the cruise and at the Bremen repository from working halves of core sections by drill-pressing standard (12 cm^3) minicores with the orientation arrow on the cut face of the sample pointing upcore (see Fig. F6). The shipboard sampling frequency was generally one minicore from every second section (3 m spacing) from one hole per site (a total of ~ 400 minicores). Additional postcruise sampling enhanced resolution of the magnetic polarity pattern in selected intervals (a total of ~ 400 minicores), especially in the Maastrichtian–Campanian of all sites and in the Eocene of Site 1258.

The cryogenic magnetometer at the Department of Earth and Environmental Sciences at the University of Munich is housed in a magnetically shielded room with equipment for thermal and AF demagnetization and measurement of susceptibility. The effective background noise of this three-axis 2-G Enterprises cryogenic magnetometer for a paleomagnetic minicore is $\sim 1 \times 10^{-6}\text{ A/m}$ ($1 \times 10^{-3}\text{ emu/cm}^3$), which implies that reliable polarity information can be obtained from samples with remanent magnetizations as low as $4 \times 10^{-6}\text{ A/m}$. This sensitivity level is an order of magnitude greater than the operation of the shipboard pass-through cryogenic magnetometer during Leg 207. To further increase the signal-to-noise ratio, we performed duplicate measurements whenever a sample had a remanent magnetization $< 8 \times 10^{-6}\text{ A/m}$.

A suite of pilot demagnetizations of representative sediment lithologies of different ages recovered during Leg 207 indicated that a combined AF and progressive thermal demagnetization treatment was effective in resolving characteristic polarities. All 800 minicores underwent an initial AF demagnetization of 5 mT, followed by progressive heating steps at 30° – 50°C increments in the 150° – 450°C range. Magnetic susceptibility was measured after each thermal demagnetization step above 300°C to monitor potential formation of new magnetic minerals or other anomalous changes in magnetic characteristics.

Nearly all samples displayed NRM with positive inclinations that are generally significantly steeper than the 20° inclination expected for the present latitude of the Leg 207 sites. These inclinations typically shallowed upon application of the initial 5-mT demagnetization step. Therefore, we interpret the NRM to have a significant component of a downward overprint induced during the coring of the seafloor, as is commonly observed by most ODP paleomagnetic studies (summarized in Acton et al., 2002).

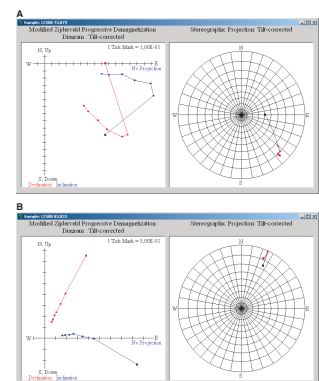
An interesting and temporary magnetodiagenetic artifact was observed after the initial thermal demagnetization step (150° or 200°C) of relatively unoxidized gray-colored minicores that still retained significant moisture. The magnetic vector measured after this first heating step was often offset from the main trend from NRM to the 5-mT AF step and through the higher heating steps. The colors of the minicores after this initial heating were generally less dark or bleached, and there was no detectable change in magnetic susceptibility. Our explanation for this offset magnetic direction that appears to vanish at the next heating step (200° or 250°C) is that the minicore lithologies have undergone creation of goethite-type iron clays as fine particles of iron sulfides or other reactive reduced iron phases undergo heating while surrounded by pore water. The goethite minerals acquired a weak magnetization even from the very low fields in the oven and cooling chamber, and this magnetization was erased upon next stage of heating above the Curie point of goethite (150°–200°C range). The lack of a significant susceptibility response by goethite minerals is consistent with these observations. This hypothesized goethite artifact was not observed in most minicores collected on board ship that had undergone unanticipated storage at room temperature for 2 months during an extended delay in customs release by Brazil, which suggests that these diagenetic alterations had already taken place prior to our measurement of NRM. Such rapid diagenetic alternation of iron minerals upon sample storage and initial heating steps was also observed when the Leg 207 cores were resampled at the ODP repository at Bremen—in just 2 months since the leg ended, many intervals in these refrigerated sediments had already experienced a change in surface coloration from the original greenish gray to a grayish tan.

Shore-Based Interpretations of Magnetostratigraphy

The polarity and characteristic magnetization for each sample were interpreted from a graphical display of the progressive variation in magnetic vectors (declination, inclination, and intensity). We used the PALEOMAG software package (freeware available from Purdue University at www.eas.purdue.edu/paleomag/) that has a combined graphical and analytical package designed for interpreting magnetostratigraphy of large suites of samples.

Two types of magnetic behavior were observed upon progressive thermal demagnetization (Fig. F7). The “N-type” displays a stable declination and consistently decreasing magnetic intensity as the inclination first undergoes a shallowing then stabilization at a low angle during progressive demagnetization steps (Fig. F7B). This magnetic behavior is consistent with a primary normal polarity direction that has been overprinted by a downward drilling-induced remanence and the present-day normal polarity field. South America has not had a significant rotation relative to the pole since the Cretaceous; therefore, as these overprints are progressively removed the declination remains rel-

F7. Thermal demagnetization of chalks, p. 66.



atively stable. In general, the NRM declination was within 20° of the characteristic declination observed at the higher steps of thermal demagnetization.

In contrast, the “Hook-type” is characterized by a significant change in declination during the first demagnetization stages and a temporary increase in magnetic intensity when the new stable declination is attained (Fig. F7A, F7C, F7D). The new magnetic vector then decreases in intensity with higher thermal demagnetization steps. We interpret this magnetic behavior as an initial NRM that contained an underlying reversed polarity vector that was partially opposed and rotated by normal polarity overprints. As these overprints are reduced during early stages of demagnetization, the reversed polarity vector is unblocked and increases in intensity until further demagnetization reduces this primary vector.

Approximately 80% of the minicore demagnetization behavior could be assigned as N-type or Hook-type, and these types were generally in stratigraphic clusters that were interpreted as polarity zones. About 20% of the samples yielded uncertain polarities for a variety of reasons, including magnetizations near the background noise level of the cryogenic magnetometer upon early stages of demagnetization, persistent steep downward overprints, or unstable magnetic directions. However, an ambiguous intermediate behavior could be displayed by a sample in which there is significant normal polarity overprint superimposed on a primary reversed polarity direction. In this case, a misleading N-type response might be displayed. This is one caution to interpreting magnetic polarity of samples solely from either demagnetization curves or inclination data without having orientation with respect to present magnetic north.

Characteristic magnetization directions and associated variances were computed for each sample by applying the least-squares three-dimensional line-fit procedure of Kirschvink (1980), which is also called principal component analysis. The characteristic direction was visually assigned to the set of vectors that during progressive demagnetization appeared to display removal of a single component in equal-area and vector plots. The intensity of characteristic magnetization was computed as the mean of the intensities of those vectors used in the least-squares fit.

Each characteristic direction was assigned a polarity rating based on the individual demagnetization behavior: (1) well-defined N or R directions computed from at least three vectors, (2) less precise NP or RP directions computed from only two vectors or a suite of vectors displaying high dispersion, (3) NPP or RPP samples that did not achieve adequate cleaning during demagnetization but their polarity was obvious—these were omitted from computations of paleolatitudes, and (4) samples with uncertain N?? or R?? or indeterminate (INT) polarity that were not used to define polarity zones. To reduce the bias of a single observer, selection and rating of characteristic magnetization vectors and associated polarity interpretations were generally examined independently by both paleomagnetists.

When both polarity and characteristic inclination is known for a discrete sample, then its magnetic paleolatitude can be computed. In contrast to our expectations prior to Leg 207, the suites of discrete minicores revealed that the sites were at or just south of the paleoequator during most of the Eocene and Paleocene. This southern latitude implies that most of the shipboard interpretations of polarity zones, which were based only on inclination clusters as explained above, were

incorrect. During the Maastrichtian and Campanian, the paleolatitudes of the array of sites were slightly north of the paleoequator; therefore, shipboard interpretations of inclination clusters were partially supported. During the Albian, the paleolatitudes of the sites appear to have been at the present latitude (10°N) or even farther north. The discrepancies of these paleolatitudes obtained from the arrays of hundreds of minicores with prior estimates based on regional plate motion reconstructions has yet to be resolved.

Acknowledgments

It was possible to complete all the shore-based paleomagnetic studies (~800 minicores) for this volume only through the generosity of Professor Valerian Bachtadse, Manuela Weiss, and the Institute of Geophysics at the University of Munich, who allowed us to have 3 weeks of full-time usage of their paleomagnetism laboratory facility and adjacent living quarters. The energetic group at the ODP Repository at Bremen sent us >100 additional minicores at the beginning of our shore-based paleomagnetic analyses and then aided us for 4 days in drill-pressing an additional 300 minicores to improve resolution of magnetic reversal boundaries at the midpoint of our analysis marathon. Joint Oceanographic Institutions/US Science Advisory committee (JOI/USSAC) provided us advance funding and a special travel grant to accomplish the postcruise collection and analysis of the minicores in Germany prior to the revision of this *Initial Reports* volume.

COMPOSITE DEPTHS

To recover the most complete sedimentary record possible, multiple holes were cored during Leg 207 at Sites 1257–1261. Continuity of recovery was assessed by constructing composite depth sections for all sites. Adjustments to the shipboard mbsf depth scale are required for several reasons, listed below, and are discussed in more detail in Ruddiman et al. (1987), Farrell and Janecek (1991), and Hagelberg et al. (1992, 1995). Rebound of the sediment under reduced pressure caused the cored sediment sequence to be expanded relative to the drilled interval. In addition, random variations in ship motion and heave may have affected the true in situ depth of each core. Portions of the sediment sequence are usually missing in section breaks, even between successive cores having 100% recovery. As a result of these factors, the mcd depth scale increases downhole relative to the mbsf scale, typically on the order of 10% (e.g., Alexandrovich and Hays, 1989; Farrell and Janecek, 1991; Hagelberg et al., 1995; Lyle, Koizumi, Richter, et al., 1997; Acton et al., 2001). A composite depth scale places coeval laterally continuous stratigraphic features into a common frame of reference by shifting the mbsf depth scales of individual cores to maximize the correlation between holes. The individual cores are shifted vertically without permitting expansion or contraction of the relative depth scale in any core. After establishing an mcd scale, more complete stratigraphic records are spliced from the data from multiple holes.

The methods we used during Leg 207 were similar to those used to construct composite depth sections during Legs 138 (Hagelberg et al., 1992), 154 (Curry, Shackleton, Richter, et al., 1995), 162 (Jansen, Raymo, Blum, et al., 1996), 167 (Lyle, Koizumi, Richter, et al., 1997), 178 (Acton et al., 2001), 189 (Exon, Kennett, Malone, et al., 2001), and

199 (Lyle, Wilson, Janecek, et al., 2002). At each site, closely spaced (2.5- to 7.5-cm interval) measurements of magnetic susceptibility, gamma ray attenuation (GRA) bulk density, and natural gamma ray (NGR) emissions were made on the MST soon after the core sections had equilibrated to room temperature. For some holes, noncontact resistivity (NCR) data were also collected on the MST. Susceptibility values are presented as raw meter values (instrument units), which can be converted to SI volume susceptibility units by multiplying by $\sim 0.68 \times 10^{-5}$ (Mayer, Pisias, Janecek, et al., 1992; Blum, 1997). Measurements of spectral reflectance were made at 2.5-cm resolution on all split cores (see “**Color Reflectance Spectrophotometry**,” p. 7, in “Lithostratigraphy”). All data were entered into the shipboard Janus database. Data profiles from each hole were compared to determine if coring offsets were maintained between holes. Integration of at least two different physical properties allowed more reliable hole-to-hole correlations than would be possible with a single data set. The physical properties most useful for correlation varied among sites and lithologies.

The mcd scale was constructed using the software program SPLICER (version 2.2), which is available on the World Wide Web from Lamont-Doherty Earth Observatory–Borehole Research Group (LDEO-BRG) at www.ldeo.columbia.edu/BRG/ODP. SPLICER allows data sets from several holes at a given site to be correlated simultaneously. Corresponding features in data sets from adjacent holes were aligned based on graphical and mathematical cross correlations using an iterative process. Correlations were first made visually by selecting a tie point from data in one hole and comparing it directly with data from another hole. Distinctive features and trends were aligned by adjusting the ODP coring depths in mbsf on a core-by-core basis. No depth adjustments can be made in an individual core using SPLICER. Postcruise refinements to the composite depths will be made where it is necessary to stretch, condense, or break individual cores.

Cross-correlation coefficients for all data sets were calculated in SPLICER. Depth adjustments were chosen that provided the best correlation in a preferred data set or the best compromise of correlation coefficients among some or all the data sets. The values of the cross-correlation coefficient vary from +1 to -1, with +1 indicating perfect correlation (such as would be obtained by comparing identical data sets) and -1 indicating anticorrelation (such as would be obtained by comparing a data set to its inverse). Values near zero indicate poor or no correlation. Each time a depth adjustment is made in SPLICER, the coefficient is recalculated, allowing the user to determine the preferred correlation. The window over which the coefficient is calculated is adjustable. The default window length of ± 2.00 m on either side of the selected tie point was used for most correlations. This window was reduced to ± 1.00 m as needed to focus on features of interest or to avoid spurious features such as those biased by coring disturbances.

Correlation began by selecting the core that had the most pristine record in the upper few meters of the sedimentary record, with particular emphasis on the mudline, if recovered. This first core is defined as the top of the composite section and its mcd depth is the same as its mbsf depth. A tie point that gives the preferred correlation was selected between data from this core and a core in a second hole. All of the data from the second hole below the correlation point were shifted vertically to align the tie points between the holes. Once the appropriate tie was determined and the depth adjustment was made, the shifted section became the reference section and a tie was made to a core from the first

hole. The process continued downhole, vertically shifting the data in one hole relative to data from the other hole. By tying points of different mbsf depths, SPLICER vertically adjusted the individual sections of the cores and brought the chosen features into the common mcd depth scale. The tie points were added to the SPLICER “affine” table. This table records the depth adjustments for each core, and these adjustments define the composite depth scale in mcd.

The composite depth section for each site is presented in tabular form in the “Composite Depths” section of each site chapter. A portion of the composite depth table of Site 1258 is given as an example in Table T8. For each core, the cumulative depth adjustment (offset) required to convert from the ODP curatorial subbottom (mbsf) depth scale to the mcd scale is given, along with the resulting composite depth (in mcd) for the top of each core. The depth offset column facilitates conversion of sample depths that are recorded in ODP curatorial subbottom depth (in mbsf) to composite depth (in mcd). The equivalent depth in mcd is obtained by adding the amount of offset listed to the depth in mbsf of a sample taken in a particular core.

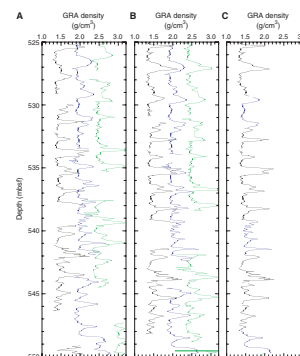
The need for a composite section to verify stratigraphic continuity is illustrated in Figure F8. In the left panel, magnetic susceptibility data from two holes at Site 1258 are shown on the mbsf depth scale. In the middle panel, the same records are shown after depth scale adjustment so that correlative features are aligned. The correlation of lithologic parameters between parallel holes and associated depth adjustments for individual cores were optimized in such a way that a single record could be sampled from the aligned cores without any additional depth scale changes. The right panel shows the resulting spliced record. Where the amount of offset necessary to align features was ambiguous or imprecise for all lithologic parameters or where multiple hole data were unavailable, no additional depth adjustments were made. In these cases, the total amount of offset between mbsf and mcd depths is equal to the cumulative offset from the overlying cores.

Where core recovery in adjacent holes spanned gaps in the sedimentary sequence, it was possible to assemble a continuous representative record (a “splice”) using the composite depths. Splice tie points were made between adjacent holes at identifiable highly correlated features. Each splice was constructed beginning at the mudline at the top of the composite section and working downward. Typically, one hole was chosen as the backbone for the record and cores from other holes were used to patch in the missing intervals in the core gaps. Intervals were chosen for the splice so that section continuity was maintained. Disturbed intervals were avoided where possible. In some cases, gaps were not spanned by recovery in any hole at a site. Here, discrete “hanging” splices were assembled. The composite splices provide a representative continuous record of each lithologic parameter (e.g., magnetic susceptibility, GRA bulk density, NGR, NCR, and spectral reflectance) for a given site. The splice can also serve as a template for sample collection for paleoceanographic studies.

Tables that give the tie points for construction of the spliced records are presented in each site chapter. An example is given in Table T9 (a portion of the splice table for Site 1258). By identifying intervals where features present in the multiply cored holes were most highly correlated, it was possible to construct a spliced record that avoided duplication or omission of individual features or cycles. Splice tie points always connect features with exactly the same composite depths. As a result, the final alignment of the adjacent holes could be slightly different

T8. Composite depth table, p. 87.

F8. GRA density, p. 69.



T9. Splice table, p. 88.

from the best overall visual or quantitative hole-to-hole correlation. Further adjustments to the composite depth section by expanding and compressing the depth scale in individual core intervals are required to align all features exactly. The procedure for the generation of a common depth scale that allows stretching and squeezing on a fine level was pioneered by Hagelberg et al. (1995) and results in a revised mcd (rmcd) scale. Typically, the generation of revised mcd scales is carried out as part of postcruise work.

SEDIMENTATION RATES

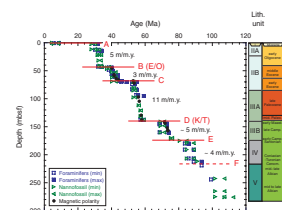
Sedimentation rates are derived from the age-depth relationship of sediments recovered at each site drilled during Leg 207. The ages are based on biostratigraphic and magnetostratigraphic shipboard data.

Where biostratigraphic data are used, the main uncertainty arises from the fact that the samples that constrain the datums may be widely separated in depth because of the limited amount of time for shipboard study. For many ODP legs, it has been necessary to reconstruct sedimentation rates by using datums determined only in core catchers (i.e., within 9.5 m). The uncertainty of sedimentation rate estimates is thus related to the sediment thickness over which they are averaged divided by the combined uncertainty in the top and bottom controls. A second source of uncertainty in the calculation of average sedimentation rates is the age of the datums. Datums used during this leg are presented in “Zonal Schemes and Taxonomy,” p. 13, in “Biostratigraphy.” Biostratigraphic data were augmented by paleomagnetic reversals recognized in shipboard measurements. The paleomagnetic record has been refined using shore-based measurements on minicores (see “Shore-Based Interpretations of Magnetostratigraphy,” p. 21, in “Paleomagnetism”), but these changes have not been integrated into sedimentation rate calculations.

Age-depth plots depict the distribution of age control points as a function of depth. Depending on the data used, uncertainty in age and/or depth may be depicted. Sedimentation rates (meters per million years) may be estimated from age-depth plots (see Fig. F9), either by fitting curves to some or all available biostratigraphic and paleomagnetic data over certain depth intervals or by connecting adjacent datums with straight line segments. Connecting datums is more likely to resolve short-term changes in sedimentation rates but also might exaggerate errors. Best-fit curves, on the other hand, might be more accurate but average out short-term variation. During Leg 207, we used the latter approach.

Age-depth plots indicate that at sites drilled during Leg 207 there are distinct changes in apparent sedimentation rates and sediment age (see Fig. F9) are present. Often, these breaks coincide with lithologic and/or color changes of the sediments recovered. These breaks may reflect nondeposition, condensed intervals, postdepositional erosion, or a combination of these. Therefore, most given sedimentation and accumulation rates are minimum estimates calculated for the lithologic segments in between these breaks. Bulk sediment mass accumulation rates (MARs) (grams per square centimeters per thousand years) are calculated by multiplying linear sedimentation rate (LSR) and dry bulk density data (in grams per cubic centimeters). The MAR of the bulk sediment was calculated for depths where a bulk density value was

F9. Age-depth plot, p. 70.



measured by the onboard physical properties program (see “[Index Properties](#),” p. 36, in “Physical Properties”).

ORGANIC GEOCHEMISTRY

The shipboard organic geochemistry program during Leg 207 included

1. Core-by-core monitoring of volatile hydrocarbons in headspace gases as required by ODP safety regulations;
2. Measurement of inorganic carbon (IC) and carbonate content of the sediments;
3. Elemental analyses of total carbon, nitrogen, and sulfur;
4. Characterization of bulk organic matter by Rock-Eval pyrolysis; and
5. Studies of solvent-extractable organic matter components.

The laboratory procedures and equipment employed during Leg 207 were adapted from those described in the “Explanatory Notes” chapters of recent ODP legs, with supplements from the technical guides for shipboard organic geochemistry (Emeis and Kvenvolden, 1986; Kvenvolden and McDonald, 1986; Pimmel and Claypool, 2001).

Interstitial Gas Analyses

Concentrations of the light hydrocarbon gases methane, ethane, propane, and propene were monitored for safety and pollution prevention. The C_1/C_2 ratio is particularly useful for indicating possibly overpressured conditions; biogenic gases commonly have ratios >1000 , whereas values <200 may indicate potential petroleum generation related to increasing depth and temperature (cf. Stein et al., 1995).

Our scientific objectives during Leg 207 included exploration of possible microbial activity in several sequences. It was predicted that organic-rich black shales in the OAEs would support elevated populations of prokaryotes, as has been demonstrated in Pleistocene sapropels (Coolen et al., 2002). A special analytical scheme was carried out on board the *JOIDES Resolution* to characterize interstitial gases originating from microbial activity.

Routine Headspace Gas Analysis of Volatile Hydrocarbons

Sampling of headspace gases in each core followed the standard procedure described by Kvenvolden and McDonald (1986). Immediately after core retrieval on deck, a $\sim 5\text{-cm}^3$ sediment sample was collected using a borer tool, placed in a 21.5-cm^3 glass serum vial, and sealed on deck or immediately in the laboratory with a septum and metal crimp cap. For consolidated or lithified samples, chips of material were placed in the vial and sealed. Prior to gas analyses, the vial was heated at 70°C for 30 min. A 5-cm^3 subsample of the headspace gas was extracted from each vial using a glass gas syringe and analyzed by gas chromatography.

Volatile hydrocarbons were analyzed using a Hewlett-Packard (HP) 6890 gas chromatograph (GC) equipped with sample loop, $2.4\text{ m} \times 3.2\text{ mm}$ ($8\text{ ft} \times 1/8\text{ in}$) stainless steel column packed with HaySep R porous polymer packing (80/100 mesh), and flame ionization detector (FID). The GC oven was programmed at 100°C for 5 min, then to increase to

140°C at 50°C/min, and finally to remain at 140°C for another 4 min. Helium was used as a carrier gas. For data acquisition and processing, HP Chemstation software was used. Chromatographic responses were calibrated using commercial standards (Scotty II Analyzed Gases, Scott Specialty Gas Co.) and the results reported in parts per million by volume (ppmv [$\mu\text{L/L}$]).

Headspace Gas Analyses of Microbial Volatile Hydrocarbons

Duplicate 4-cm³ samples of sediment were collected using a cutoff 5-cm³ syringe or borer tool and placed in a 21.5-cm³ headspace vial immediately after core retrieval on deck. The samples were taken immediately to the microbiology laboratory where ~5 mL of 1-N NaOH was added. The vials were then sealed with Teflon/silicone septa and metal crimp caps. The two samples were shaken gently for ~1 hr. One sample (A) was reserved for shore-based control studies. Headspace gas from vial B was analyzed ~36 hr after recovery to determine interstitial volatile hydrocarbons (C₁–C₄). A 4-mL aliquot of headspace gas was removed with a glass gas-tight valve syringe, compressed to 2.5 cm³, and the pressure in the syringe barrel was reduced to atmospheric by briefly opening the valve. The chromatographic conditions used were as described in “[Routine Headspace Gas Analysis of Volatile Hydrocarbons](#),” p. 27.

The remaining headspace content of vial B was then transferred to a clean, evacuated headspace gas vial containing ~5 mL of water using a double-ended needle. This sample was reserved for future isotopic analysis. Headspace gas contents of vial B will be measured again after ~2 months to measure any additional desorbed volatile hydrocarbons.

Natural Gas Analyses

Headspace samples of interstitial gases were also analyzed with the natural gas analyzer (NGA) when high concentrations of C₂₊ hydrocarbons or nonhydrocarbon gases such as H₂S or CO₂ were anticipated. The NGA system consists of a HP 6890 GC equipped with multiport valves that access different column and detector combinations. Both FID and thermal conductivity detectors (TCD) are employed; helium was used as a carrier gas. Detectable gases are N₂, O₂, CO₂, H₂S, CS₂, and hydrocarbons in the range of C₁–C₁₀, which are detected by applying a system of four columns for sequential partitioning. First, a 60 m × 0.32 mm capillary column coated with a 1- μm film of DB-1 (J&W, Inc.) and the FID were employed for separation and detection of C₁–C₇ hydrocarbons isothermally at 50°C (15 min). The multicolumn system also contains a 1.8-m (6 ft) stainless steel column packed with HaySep R porous polymer (80/100 mesh) (acid washed). This column was held at 80°C, and used for the separation of air and methane from O₂, N₂, CO₂, C₂, C₃, ethylene, and propylene as well as H₂S, if present in high concentrations. Then, a nonheated combination of a 15.2-cm (6 in) stainless steel column packed with Poropak T (50/80 mesh) in line with a 0.9-m (3 ft) column packed with molecular sieve 13× (60/80 mesh) was used for O₂, N₂, and C₁ analysis. All nonhydrocarbon gases were analyzed isothermally using the sequence of packed columns, as stated above, and the TCD. For data acquisition and evaluation, an HP ChemStation computer system was used. Chromatographic responses are calibrated

against preanalyzed standards; gas contents are reported in parts per million by volume (ppmv).

Carbonate Analysis

The weight percentage of inorganic carbon was determined by titration using a Coulometrics 5011 CO₂ analyzer equipped with a System 140 carbonate analyzer. A 20-mg freeze-dried ground sediment sample was reacted with 2-N HCl to liberate CO₂. The gas is cleaned of SO₂ and transferred into a vial filled with a blue-colored aqueous proprietary solution using CO₂-free air as a carrier gas. An acidic reaction of the CO₂ gas with this solution induces a color change. A base is added stepwise until the now-clear liquid returns to its original tint. The CO₂ titration process is controlled by a photodetection cell, which constantly monitors the change in light transmittance of the solution. The volume of basic titrant is proportional to the inorganic carbon content of the sample. The percentage of carbonate is calculated from the inorganic carbon using the following equation:

$$\text{CaCO}_3 \text{ (wt\%)} = \text{IC (wt\%)} \times 8.33.$$

This method assumes that all of the CO₂ evolved was derived from dissolution of calcium carbonate. No corrections were made for other carbonate minerals.

Elemental Analysis

Total carbon, nitrogen, and sulfur were determined using an autosampler-equipped Carlo Erba NA 1500 CHNS analyzer, which combusts sediment samples in tin cups with an oxidant at 1000°C in a stream of oxygen. The analytical procedure employs a sample of 5- to 15-mg freeze-dried, crushed sediment with ~10 mg V₂O₅ acting as an oxidation catalyst. Helium was used as a carrier gas. Nitrogen oxides were reduced to N₂, and the mixture of N₂, CO₂, H₂O, and SO₂ gases was separated by gas chromatography. Detection of individual components was performed with a TCD. The hydrogen value is not useful because it represents both hydrogen derived from organic matter and that produced from water bound to clay minerals. All measurements were calibrated by comparison to a pure sulfanilamide standard. The amount of total organic carbon (TOC) was calculated as the difference between total carbon (TC) and inorganic carbon (determined from coulometry),

$$\text{TOC (wt\%)} = \text{TC (wt\%)} - \text{IC (wt\%)}.$$

In addition to the TOC concentration, elemental analysis yields the C/N atomic ratio, which can be used to help identify sources of organic matter (fresh marine C/N = 6–8; degraded marine C/N = 8–20; continental C/N = >20).

Organic Matter Characterization and Maturity Determination

The type of organic matter was characterized by programmed pyrolysis using a Delsi Nermag Rock-Eval II system. This method is based on a whole-rock pyrolysis technique designed to identify the type of organic

matter and its maturity and to evaluate the petroleum potential of sediments (Espitalié et al., 1986). Although the Rock-Eval II system can provide an independent measure of TOC, the TOC module did not function during Leg 207 and TOC values determined as described in “[Elemental Analysis](#),” p. 29, were used instead.

The Rock-Eval system includes a temperature program that first releases volatile hydrocarbons from organic matter by heating at 300°C for 3 min (S_1). Hydrocarbons are then released via thermal cracking of kerogen (S_2) as the temperature is increased to 550°C at 25°C/min. The S_1 and S_2 hydrocarbons are measured by FID and reported in milligrams per gram of dry sediment. The temperature at which the kerogen yields the maximum amount of hydrocarbons (top of the S_2 peak) provides the parameter T_{max} , which is used to assess the thermal maturity of the organic matter. Between 300° and 390°C of the programmed pyrolysis, CO_2 released from the thermal degradation of organic matter (S_3) is trapped and subsequently measured by TCD and reported in milligrams per gram dry sediment. Rock-Eval analysis provides the calculated parameters hydrogen index (HI), oxygen index (OI), and the S_2/S_3 ratio:

$$HI = S_2/TOC \times 100 \text{ and}$$

$$OI = S_3/TOC \times 100.$$

In general, high hydrogen index values (>400) indicate large proportions of well-preserved algal and microbial organic matter, whereas high oxygen index values (>100) are an indicator of continental organic matter or of immature organic matter of all sources.

The production index (PI) is defined as

$$PI = S_1/(S_1 + S_2).$$

This value is usually <0.2 in immature rocks; values of 0.3–0.4 are typical for samples in the petroleum window ($T_{max} = 420^\circ\text{--}450^\circ\text{C}$). Values of >0.5 may indicate the proximity of migrated hydrocarbons or trapped petroleum.

Interpretation of Rock-Eval oxygen index data may be compromised for samples containing >10 wt% carbonate, and the values themselves are also unreliable for young and immature organic matter (<1 Ma or $T_{max} = < 400^\circ\text{C}$) (Peters, 1986). Furthermore, samples with <0.5 wt% TOC do not give reliable results because of the small size of the S_1 , S_2 , and S_3 signals.

Solvent Extractable Components: Higher Hydrocarbons and Alkenones

Solvent-extractable organic constituents were examined to assess the biomarker contents of organic matter in Cretaceous black shales. The focus of these analyses was to determine the relative compositions of the hydrocarbons and related components in selected sediment sequences. Measurement of absolute concentrations of individual constituents was not attempted. These data are reported in [Forster et al.](#), this volume.

The extraction procedure consisted of ultrasonic extraction of 1–4 g of sediment for 30 min using 8 mL of CH_2Cl_2 . The extract was trans-

ferred to a vial and reduced to dryness under N₂. It was transferred in hexane to a silica column and successively eluted with 4 mL hexane (aliphatics), 4 mL 1:1 hexane:dichloromethane (aromatics), and 4 mL dichloromethane (polar hydrocarbons). The hexane eluate is predominantly aliphatic hydrocarbons and monoaromatic hydrocarbons. The CH₂Cl₂ eluate contains aromatic hydrocarbons and ketones, including alkenones. Each eluant was taken to near dryness under N₂ and transferred using 50–100 µL of hexane to a vial for analysis by gas chromatography–mass selective detector (GC-MSD). Extraction of 1 g of Colorado oil shale was used to verify the extraction and separation procedures.

The GC-MSD consists of an HP 6890 GC with an HP-5973 MSD and an HP 7683 automatic liquid sampler. The GC is equipped with an electronically program-controlled split-splitless injector and an HP capillary column (5% phenyl methyl siloxane; 30 m × 0.25 µm) programmed from 70° to 130°C at 20°C/min, then at 4°C/min to 320°C, and held at 320°C for 20 min. Helium was used as the carrier gas. The transfer line was set at 280°C and the source of the MSD at 230°C. The MSD scanned from 27 to 800 *m/z*. HP MS Chemstation software was used for data acquisition and processing. The identity of individual hydrocarbons was determined from their mass spectral characteristics and GC retention times by comparison with literature values.

INORGANIC GEOCHEMISTRY

Typically, shipboard interstitial water analyses were performed on 5- or 10-cm-long whole-round sections that were cut immediately after the core arrived on deck. Details of the sampling resolution are described in the individual site chapters of this volume. After extrusion from the core liner, the surface of each whole-round section was scraped with a spatula. In samples recovered by XCB and RCB drilling technology, care was taken to separate the so-called “biscuited” core samples from their associated slurry before squeezing. These steps are required to avoid contamination of the interstitial water signal by seawater.

Interstitial waters were collected using titanium squeezers that were modified after the standard stainless steel squeezer (Manheim and Sayles, 1974). Pressure up to 275 MPa (40,000 psi) was applied using a hydraulic press. Where necessary, the sample was left in the squeezer for an extended period (up to 24 hr) and the applied pressure was increased very slowly. This modified technique helped to maintain interstitial water yields at levels sufficient for the shipboard and shore-based analytical programs.

Interstitial waters were passed through prewashed Whatman number 1 filters fitted above a titanium screen and subsequently extruded into a plastic syringe attached to the bottom of the squeezer assembly. All interstitial water samples were double-filtered through 0.45-µm polycarbonate filters. Samples for shipboard analysis were stored in plastic vials pending analysis. Aliquots for future shore-based analyses were placed in glass ampules or plastic tubes and heat sealed or kept in precleaned polyethylene bottles and stored in a refrigerator. In cases where trace amounts of hydrogen sulfide were present, sulfide was trapped by the addition of 0.2 mL of a 1% zinc acetate solution.

Interstitial water samples were routinely analyzed for salinity as total dissolved solids with a Goldberg optical handheld refractometer. The

pH and alkalinity were determined by Gran titration with a Brinkmann Instruments pH electrode and a Metrohm autotitrator. Dissolved chloride was determined by titration with silver nitrate. Ammonium and a few silica concentrations were determined by spectrophotometric methods (Gieskes et al., 1991) using a Milton Roy Spectronic 301 spectrophotometer equipped with a sample introduction system. Alkali (Li, Na, and K) and alkaline earth (Mg, Ca, Sr, and Ba) elements together with manganese, iron, and boron concentrations were determined by inductively coupled plasma–atomic emission spectroscopy (ICP-AES) following the general procedure outlined by Murray et al. (2000). Sulfate was analyzed as total dissolved sulfur and silica as total dissolved silica by ICP-AES. Details of the procedure are given below. In preparation for analysis by ICP-AES, aliquots of interstitial water were acidified with nitric acid and diluted tenfold with deionized water (0.5 mL of sample + 4.5 mL of deionized water). Analytical blanks were prepared identically by analyzing deionized water, which was acidified to matrix match the samples. At all sites, sodium was determined by charge balance calculation where

$$[\text{Na}^+] = [\text{Alk}] - [\text{K}^+] - 2[\text{Mg}^{2+}] - 2[\text{Ca}^{2+}] + [\text{Cl}^-] + 2[\text{SO}_4^{2-}]$$

(Broecker and Peng, 1982). The chemical data for interstitial waters are reported in molar units. The reproducibility of results, determined via multiple determinations of the International Association for the Physical Sciences of the Ocean (IAPSO) standard seawater (alkalinity, Cl^- , Ca^{2+} , Mg^{2+} , K^+ , and SO_4^{2-}), spiked synthetic seawater (ICP-AES determinations), or through the use of a calibration curve (NH_4^+ , HPO_4^{2-} , and $\text{Si}[\text{OH}]_4$), is available in Table T10.

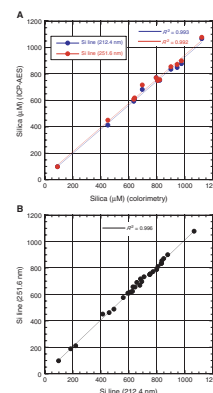
Determination of Total Dissolved Sulfur and Total Dissolved Silica by ICP-AES

Sulfur and silica have strong emission lines that may be used for the determination of both elements in interstitial waters by ICP-AES. The method should allow the determination of trace quantities of sulfate (≤ 0.2 mM) and silica (≤ 100 μM) on relatively small sample volumes. For silica, two emission lines, at 212.4 and 251.6 nm, are recommended for analysis. We included both lines in the routine minor element run, which is performed on 1:10 diluted interstitial water samples. Calibration was performed by adding appropriate amounts of the silica standard to the master solution containing the other minor elements. The calibration curve covered a silica concentration range of 0–3340 μM . Twelve interstitial water samples were analyzed for silica by the routine shipboard colorimetric method. Figure F10A shows a comparison of results obtained by both methods, whereby the two emission lines mentioned for silica were used for analysis. Figure F10B shows that the results obtained for both silica emission lines are essentially identical. For this reason, the more sensitive silica emission line at 251.6 nm was used exclusively for further analysis.

For sulfur, two strong emission lines at 180.676 and 181.978 nm (Jobin Yvon instrument library) were checked. According to other emission line libraries, the sulfur lines are located at 182.036 and 180.734 nm (B. Schnetger, pers. comm., 2003), but the latter line is interfered by calcium and manganese. Calibration curves were made up from IAPSO standard seawater diluted with a 3.5% NaCl solution made from Pura-

T10. Analytical reproducibility, p. 89.

F10. Comparison of Si results, p. 71.



tronic metal-free NaCl. In the high concentration range, both lines are suitable for analysis, but in the low concentration range (<5 mM), significant differences are evident. Results obtained from the sulfur line at 180.676 nm are significantly higher than those from the other line, most likely because of calcium interference. For this reason, only the sulfur line at 181.978 nm was used for subsequent analysis. In the ultraviolet range of the instrument, adequate flushing with nitrogen is required. This should be carried out for at least 12 hr prior to analysis. If this is not done, detection limits and reproducibility may be adversely affected. The ICP-AES method is very rapid (up to 30 samples may be analyzed per hour); therefore, we typically included a calibration point as every third sample.

PHYSICAL PROPERTIES

Shipboard measurements of physical properties provide information useful in the characterization of lithostratigraphic units, correlation of lithology with downhole geophysical logging data, assessment of the nature of consolidation, and interpretation of seismic reflection profiles. The primary objectives of the Leg 207 physical properties program were to collect high-resolution data to

1. Facilitate hole-to-hole correlation and construction of composite stratigraphic sections,
2. Allow correlation between sites,
3. Enable cyclostratigraphic studies to help constrain events across critical intervals,
4. Facilitate construction of synthetic seismograms, and
5. Investigate the characteristics of major seismic reflectors.

Several types of physical property measurements were performed on unsplit sections. Nondestructive measurements of bulk density, magnetic susceptibility, transverse compressional (*P*)-wave velocity, NGR, and resistivity were performed on the MST. The MST incorporates a GRA densitometer, a *P*-wave logger (PWL), a magnetic susceptibility meter, an NGR sensor, and an NCR sensor. Thermal conductivity, using the needle-probe method, was also measured at discrete intervals in whole-round sections from the upper four to five cores from two sites (Sites 1257 and 1260).

Measurements on split-core sections included discrete transverse and axial *P*-wave velocity and moisture and density (index) properties. Measured index properties of discrete samples (namely wet and dry mass and dry volume) were used to determine bulk density, dry bulk density, grain density, water content, porosity, and void ratio. A comprehensive discussion of all methodologies and calculations used in the *JOIDES Resolution* physical properties laboratory can be found in Blum (1997).

Multisensor Track Measurements

The principal aim of MST data acquisition during Leg 207 was to obtain high-resolution data sets to facilitate shipboard core-to-core correlation, to allow the construction of composite stratigraphic sections, and to provide for cyclostratigraphic analyses across critical boundaries and intervals. These objectives had to be completed within a reasonable time frame without compromising the shipboard processing of recov-

ered core. As the IMS software used to control the MST was only capable of handling four instruments at a time, it was necessary to strategically employ certain types of measurements for different sites and holes. The PWL and NCR and NGR sensors were all taken off-line at times. The site, hole, and sections measured with each sensor are listed in Table T11.

The GRA densitometer measures the attenuation of gamma rays that pass through the core material, where the degree of attenuation is proportional to density (Boyce, 1976). Calibration of the GRA system was completed using known seawater/aluminum density standards. GRA bulk density data are of highest quality when determined on APC cores because the liner is generally completely filled with sediment. In XCB and RCB cores where the cores do not completely fill the full inner diameter of the liner, GRA measurements are of lower quality and cannot be used to reliably determine bulk density on their own. The measurement width of the GRA sensor is ~0.5 cm, with sample spacing generally set at 2.5 cm for Leg 207 cores. The minimum integration time for a statistically significant GRA measurement is 1 s, and routine Leg 207 GRA measurements used either a 3- or 4-s integration time. A freshwater control was run with each section to measure instrument drift.

Whole-core magnetic susceptibility was measured with the MST using a Bartington MS2C meter with an 8-cm (internal diameter) loop. The measurement resolution of the susceptibility sensor is 5 cm on either side of the loop, with a minimum statistically significant count time of 1 s. During Leg 207, MST magnetic susceptibility was routinely measured at a spacing of 2.5 cm with a single data acquisition. Magnetic susceptibility data were archived as raw instrument units and not corrected for changes in sediment volume. To obtain SI units, these raw instrument values need to be multiplied by 0.68×10^{-5} (Blum, 1997).

Transverse *P*-wave velocity was measured on the MST with the PWL. All APC cores where coupling of the sediment and liner existed and saturation was high enough to transmit the pulse were measured (Table T11). The PWL was not used on XCB or RCB cores because the weak core liner/sediment interface results in poor acoustic coupling between the sediment and the liner. The PWL transmits a 500-kHz compressional wave pulse through the core at 1 kHz. The transmitting and receiving transducers are aligned perpendicular to the core axis. A pair of displacement transducers monitors the separation between the compressional wave transducers so that variations in the outside diameter of the liner do not degrade the accuracy of the measured velocities. The displacement transducers were calibrated using a series of acrylic blocks of known thickness, while the *P*-wave traveltime and measurement of electronic delay in the PWL circuitry was calibrated using a plastic bag filled with distilled water. The bag was manipulated to sit between the transducers at varying distances. Repeated measurement of *P*-wave velocity through a core liner filled with distilled water was used to check the calibration validity. The measurement width of the PWL sensor is ~0.1 cm, with sample spacing routinely set at 2.5 cm for Leg 207 APC cores.

Electrical resistivity of sediment cores was measured using the NCR sensor on the MST. NCR measurements are made by using a high-frequency magnetic field to induce an electrical current in the core. Magnetic fields, regenerated by the electrical current, are measured on a receiver coil and normalized with a set of coils operating in air. Calibration of the NCR is achieved by measuring a variety of core-sized standards containing seawater of varying but known salinity. The salinity of

T11. MST sampling frequencies,
p. 90.

each standard was measured in the chemistry laboratory using a refractometer. The relationship between NCR millivolt output and true resistance is determined by plotting the sensor output for each standard against the empirically determined resistivities of the solutions. During Leg 207, five standards were constructed during transit using core liner cut into 15-cm pieces and filled with diluted solutions of seawater. One standard remained undiluted. The resistivity of each of these standards was calculated from the salinities using a power-curve relationship derived from the salinities of known NaCl solutions found in the *CRC Handbook of Physical Properties of Rocks* (Carmichael, 1982) and compared to the resistances derived from the calibration curve determined during the NCR sensor installation during Leg 204 (see Tréhu, Bohrmann, Rack, Torres, et al., 2003). Excellent agreement existed between the two methods for determining the resistance of the various standards between 18.5 and 35.5 psu, illustrating that the relationship between the NCR millivolt output and true resistance (derived during Leg 204) remained accurate and applicable (Table T12).

Extensive RCB drilling during Leg 207 introduced a complication into the acquisition and interpretation of the resistivity data from the MST. RCB cores tend to have a substantial and variable gap between the core and the liner. Although resistivity was routinely measured on all cores and was occasionally found to be in good agreement with the GRA density, it was not until the end of drilling operations that an attempt was made to measure the response of the sensor to variable distances from the core. A sequence of measurements was made on a single seawater standard with the sensor placed at variable distances from the outside of the core liner (Table T13). With increasing distance from the water standard, one would expect the resistance to increase; however, it was not possible to define this relationship based upon the results from this test. As illustrated in Table T13, there does not appear to be a readily definable relationship between distance and sensor response. Without better constrained core diameters, normalization of the NCR resistivity data for most of the RCB cores and thus for most of the material recovered during Leg 207 does not appear possible. Resistivity data collected during Leg 207 should be interpreted with utmost caution.

NGR was measured on the MST, and the operating principles of the system used on the *JOIDES Resolution* are discussed by Hoppie et al. (1994). Data from 256 energy channels were collected and archived. For presentation purposes, the counts were summed over the range of 200–3000 keV in order to be comparable with data collected during previous legs. This integration range also allows direct comparison with down-hole logging data, which were collected over a similar integration range (Hoppie et al., 1994). Over the 200- to 3000-keV integration range, background counts, measured using a core liner filled with distilled water, averaged ~30 during a 1-hr measurement period. Before taking measurements, each of the four NGR amplifiers was adjusted so that the main thorium peaks (2615 keV) for each sensor were exactly aligned. The multichannel analyzer was then calibrated by assigning certain channels to the characteristic energies of ^{40}K and the main peak of ^{232}Th (Blum, 1997). The measurement width of the NGR sensor is ~15 cm, with a statistically significant count time of at least 5 s, depending on lithology. Because of the long time required for NGR measurements, sample spacing for NGR measurements varied between 7.5 and 15 cm, depending on the age and lithology of the sediment recovered (Table T11). No cor-

T12. NCR calibration standard salinities, p. 91.

T13. NCR sensor calibration, p. 92.

rections were made to NGR data obtained from XCB or RCB cores to account for sediment incompletely filling the core liner.

Thermal Conductivity

The thermal conductivity of core material was measured in suitable whole-core sections using the needle-probe method in full-space configuration for soft sediments (Von Herzen and Maxwell, 1959). Sediment soft enough to be measured with the insertion probe was restricted to Cores 1–5 in Holes 1257A and 1257B and Cores 1–4 in Hole 1260B.

The full-space needle, containing a heater wire and calibrated thermistor, was inserted into the unconsolidated sediment through a small hole drilled into the core liner. Three measuring cycles were automatically performed at each sampling location. At the beginning of each test, a self-test that included a drift study was conducted. Once the samples were equilibrated, the heater circuit was closed and the temperature rise in the probes was recorded. Thermal conductivities were calculated from the rate of the temperature rise while the heater current was flowing. Temperatures measured during the first 150 s of the heating cycle were fitted to an approximate solution of a constantly heated line source (for details see Kristiansen, 1982; Blum, 1997). Measurement errors were 5%–10%. No correction was attempted for in situ temperature or pressure effects. Thermal conductivity was measured only in soft sediments, into which the TK04 needles could be inserted without risk of damage.

Index Properties

Index (moisture and density; MAD) properties (bulk density, dry bulk density, grain density, water content, porosity, and void ratio) were determined from measurements of wet and dry sediment mass and dry sediment volume. Discrete ~10-cm³ samples were taken from soft sediments and placed in 10-mL beakers. Samples were collected at a frequency of one per section in Hole A at each site and in Holes B and C when these cored intervals were not recovered in Hole A. One sample per core was collected in intervals already recovered from other holes. Sampling was minimal through the Cretaceous black shale sequence and across critical boundaries.

Sample mass was determined with a reproducibility of $\pm 3\%$ standard deviation using an electronic balance (Scientech). The balance is equipped with a computer averaging system that corrects for ship acceleration. The sample mass is counterbalanced by a known mass so that the mass differentials are generally <1 g. Sample volumes were determined using a helium-displacement pycnometer (Quantachrome penta-pycnometer). Volume measurements were repeated at least five times, until the last two measurements exhibited <0.01% standard deviation. A reference volume was included in each sample set and rotated sequentially among the cells to check for instrument drift and systematic error. A purge time of 2 min was used before each run. The sample beakers used for discrete determination of moisture and density were calibrated before the cruise.

Each MAD property was calculated using measurements of wet and dry sediment mass and dry sediment volume; the latter two parameters were measured after samples had been oven dried at $105^\circ \pm 5^\circ\text{C}$ for 24 hr and allowed to cool in a desiccator. This analytical method is pre-

ferred because volume measurements of wet samples are less accurate than dry samples when measuring in the pycnometer. The procedures for the determination of these properties comply with the American Society for Testing and Materials (ASTM) designation (D) 2216 (ASTM, 1990).

Wet mass (M_{wet}), dry mass (M_{dry}), and dry volume (V_{dry}) are measured in the laboratory. Salt precipitated in sediment pores during the drying process is included in the M_{dry} and V_{dry} values. The mass of the evaporated water (M_{water}) and the salt (M_{salt}) in the sample are given by

$$M_{\text{water}} = M_{\text{wet}} - M_{\text{dry}} \text{ and}$$

$$M_{\text{salt}} = M_{\text{water}} [s/(1-s)],$$

where s is the assumed seawater salinity (0.035) corresponding to a pore water density (ρ_{pw}) of 1.024 g/cm³ and a salt density (ρ_{salt}) of 2.257 g/cm³. The corrected mass of pore water (M_{pw}), volume of pore water (V_{pw}), mass of solids excluding salt (M_{solid}), volume of salt (V_{salt}), volume of solids excluding salt (V_{solid}), and the wet volume (V_{wet}) are, respectively,

$$M_{\text{pw}} = M_{\text{water}} + M_{\text{salt}} = M_{\text{water}}/(1-s),$$

$$V_{\text{pw}} = M_{\text{pw}}/\rho_{\text{pw}}$$

$$M_{\text{solid}} = M_{\text{dry}} - M_{\text{salt}}$$

$$V_{\text{salt}} = M_{\text{salt}}/\rho_{\text{salt}}$$

$$V_{\text{solid}} = V_{\text{dry}} - V_{\text{salt}} = V_{\text{dry}} - M_{\text{salt}}/\rho_{\text{salt}} \text{ and}$$

$$V_{\text{wet}} = V_{\text{solid}} + V_{\text{pw}}$$

Calculation of Bulk Properties

For all sediment samples, water content (w) is expressed as the ratio of the mass of pore water to the wet sediment (total) mass,

$$w = M_{\text{pw}}/M_{\text{wet}}$$

Bulk density (ρ_{wet}), dry bulk density (ρ_{dry}), sediment grain density (ρ_{solid}), and porosity (ϕ) are calculated from

$$\rho_{\text{wet}} = M_{\text{wet}}/V_{\text{wet}}$$

$$\rho_{\text{dry}} = M_{\text{solid}}/V_{\text{wet}}$$

$$\rho_{\text{solid}} = M_{\text{solid}}/V_{\text{solid}} \text{ and}$$

$$\phi = V_{\text{pw}}/V_{\text{wet}}$$

Compressional Wave Velocity

Velocity was measured on split-core sections using the PWS1 and PWS2 insertion probe system in soft sediments and the PWS3 contact

probe system in consolidated sediments and rocks. The insertion probe system allows measurement of the longitudinal (perpendicular to bedding) *P*-wave velocity (PWS1) and the transverse *P*-wave velocity (PWS2). The contact probe system (PWS3) measures the transverse velocity across the split-core section and core liner or across samples taken from the cores. In both systems, the *P*-wave velocity calculation is based on the accurate measurement of the delay time of a 500-kHz acoustic square wave signal traveling between a pair of piezoelectric transducers. Transducer separations of PWS1 and PWS2 are fixed at 6.96 and 3.48 cm, respectively. The transducer pair for PWS3 is adjusted to the thickness of the core half or extracted sample. A linear voltage-displacement transducer measures the separation of the fixed lower PWS3 transducer and the movable upper transducer. Prior to measuring velocity on samples from each hole, the PWS1 and PWS2 transducers were calibrated by inserting the probes in a container of distilled water of known temperature and measuring the acoustic traveltime. The PWS3 transducers were calibrated using the linear regression of traveltime vs. distance across a plastic bag filled with water measured at a variety of thickness.

Routine sampling frequency for *P*-wave measurements was one per section while using the PWS1 and PWS2 sensors. When the PWS3 sensor was utilized, the sampling frequency was three measurements per section on split cores in Hole A at each site. Measurements of transverse (*x*- and *y*-direction) and longitudinal (*z*-direction) *P*-wave velocity were conducted on cube samples in Hole B at each site, allowing the calculation of velocity anisotropy using the following equation:

$$200(V_{pt} - V_{pl})/(V_{pt} + V_{pl}),$$

where,

V_{pt} = average transverse *P*-wave velocity and
 V_{pl} = average longitudinal *P*-wave velocity.

The positions of the *P*-wave measurements are next to those for MAD analyses. Deionized water was added to the contact between the transducers and sample to improve acoustic coupling when needed. Data reported herein and those stored in the Janus database are uncorrected for in situ temperature and pressure. These corrections can be made using the relationships outlined in Wyllie et al. (1956), Wilson (1960), and Mackenzie (1981) and as applied in Boyce (1976).

In Situ Temperature Measurements and Heat Flow Calculations

A single in situ temperature measurement was made in Hole 1257A in the upper 40 m, which is the only Leg 207 APC-cored interval. The components of the Adara temperature tool are contained in an annulus in the coring shoe of the APC string and include a platinum temperature sensor and a data logger. The platinum resistance-temperature device is calibrated over a range of 0°–100°C, with a resolution of 0.01°C. During operation, the coring shoe is attached to a core barrel and lowered down the pipe by wireline. The tool is typically held for 5–10 min at the mudline to equilibrate with bottom water temperatures then lowered to the end of the drill string. The standard APC coring technique is subsequently used, with the core barrel fired through the drill bit using

hydraulic pressure. The Adara tool is left in the sediment for 10–15 min to obtain a temperature record. Data from the tool provide a sufficiently long transient record for reliable extrapolation of the steady-state temperature. The nominal accuracy of the Adara temperature measurement is $\pm 0.1^\circ\text{C}$.

DOWNHOLE LOGGING

Downhole logging tools are used to determine physical, chemical, and structural properties of the formation penetrated by a borehole. Data are rapidly collected, continuous with depth, and, most importantly, are measured in situ. Logs may be interpreted in terms of the stratigraphy, lithology, mineralogy, and geochemical composition of the formation. Where core recovery is good, logging and core data are complementary and should be integrated and interpreted jointly, with logging data providing in situ ground truth for core data. Where core recovery is incomplete or disturbed, logging data may provide the only means to characterize the borehole section.

Downhole logs record formation properties on a scale that is intermediate between those obtained from laboratory measurements on core samples and geophysical surveys. They are critical for calibrating geophysical survey data (e.g., through synthetic seismograms), providing the necessary link for the integration of core depth-domain to seismic time-domain data. Wireline logging was scheduled for four of the five sites cored during Leg 207.

Wireline Logging

Data are obtained by a variety of Schlumberger and Lamont-Doherty Earth Observatory (LDEO) logging tools combined into several tool strings and deployed in a hole after coring operations are completed. The tool strings are deployed by lowering them to the bottom of the hole and recording data as they are pulled (at constant rate) up the hole. Heave compensation is applied to eliminate or minimize ship motion while logging to ensure a constant rate of ascent of the tool string. Repeat runs or partial runs are undertaken for all tools for data quality control. Three tool strings were run during Leg 207, although not all were run at every site. Details are given in individual site chapters. The three tool strings that were run are the following:

1. The triple combination (triple combo) tool string consists of resistivity (phasor Dual Induction Tool [DIT]), bulk density (Hostile Environment Litho-Density Tool [HLDT]), gamma ray (Hostile Environment Natural Gamma Ray Sonde [HNGS]), and porosity (Accelerator Porosity Sonde [APS]) components, with two additional LDEO tools that measured high-resolution gamma ray (Multi-Sensor Spectral Gamma Ray Tool [MGT]), and temperature, acceleration, and pressure (Temperature/Acceleration/Pressure [TAP] tool).
2. The Formation MicroScanner (FMS)-sonic tool string consists of microresistivity (FMS), sonic velocity (Long Spacing Sonic [LSS]), gamma ray (Scintillation Gamma Ray Tool [SGT]), and orientation/acceleration (General Purpose Inclinator Tool [GPIT]) components.

- The Well Seismic Tool (WST) consists of a single geophone pressed against the borehole wall that is used to record the acoustic waves generated by an air gun located near the sea surface, offset from the ship.

Natural gamma radiation tools are included on both the triple combo and FMS-sonic tool strings to provide a common reference for correlation and depth shifting between multiple logging runs. WST depths are taken from the wireline cable depths. Further tool details are given in Figure F11 and Tables T14 and T15.

Each tool string contains a telemetry cartridge facilitating communication between the tools along the wireline (seven-conductor cable) and the Schlumberger minimum configuration multitasking acquisition and imaging system (MAXIS) (MCM) unit located on the ship. Ship heave motion is a further complication in the acquisition of quality wireline logging data. To overcome this problem, the wireline is fed over the wireline heave compensator (WHC). As the ship heaves in the swell, an accelerometer located near the ship's center of gravity measures the movement and feeds the data, in real time, to the WHC. The WHC responds to the ship's heave by adding or removing cable slack to decouple the movement of the ship from the tool string (Goldberg, 1990). During each logging run, incoming data are recorded and monitored in real time on the MCM logging computer. Tool strings are pulled up at constant speed to provide continuous measurements as a function of depth.

The MGT is not a Schlumberger tool and cannot record data while the Schlumberger tools are active. Thus, the MGT requires separate passes for data acquisition, during which time control of the wireline transfers to the LDEO logger and data are recorded, in real time, on the specialized acquisition system in the downhole measurements laboratory (DHML).

Logged Sediment Properties and Tool Measurement Principles

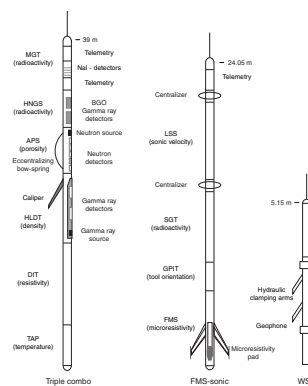
The logs acquired by the wireline tools are listed in Table T15. A brief description of the measurement methods and the logged properties is given below. More detailed information on individual tools and their geological applications may be found in Ellis (1987), Goldberg (1997), Lovell et al. (1998), Rider (1996), Schlumberger (1989, 1994), and Serra (1984, 1986, 1989).

Natural Radioactivity

Three wireline spectral gamma ray tools were used to measure and classify natural radioactivity in the formation: the SGT, HNGS, and MGT. The SGT uses a scintillation detector to measure the total gamma ray radiation originating in the formation and provides data for depth matching to other tool string passes. The HNGS uses two bismuth germanate scintillation detectors for high tool precision. It also filters out gamma ray energies <500 keV, eliminating sensitivity to bentonite or KCl in the drilling mud and improving measurement accuracy.

The MGT was developed by LDEO-Borehole Research Group (BRG) to improve the vertical resolution of NGR logs by using an array of four short detector modules with ~2-ft spacing. Each module comprises a small 2 in × 4 in NaI detector, a programmable 256-channel amplitude

F11. Tool strings, p. 72.



T14. Wireline tool string measurements, p. 93.

T15. Wireline tool acronyms and units, p. 94.

analyzer, and an ^{241}Am calibration source. The spectral data are subsequently recalculated to determine the concentration of potassium, thorium, and uranium radioisotopes or their equivalents. The spectral data from individual modules are sampled 4 times/s and stacked in real time based on the logging speed. This approach increases vertical resolution by a factor of 2–3 over conventional tools while preserving comparable counting efficiency and spectral resolution. The radius of investigation depends on several factors: hole size, mud density, formation bulk density, and the energy of the gamma rays (a higher-energy gamma ray can reach the detector from deeper in the formation). The MGT also includes an accelerometer channel to improve data stacking by the precise measurement of logging speed. Postcruise processing may correct for borehole size and tool sticking using the acceleration data.

Density

Formation density was determined with the HLDT. This tool contains a radioactive cesium (^{137}Cs) gamma ray source (622 keV) and far- and near-field gamma ray detectors mounted on a shielded skid, which is pressed against the borehole wall. Gamma rays emitted by the source undergo Compton scattering, which involves the transfer of energy from gamma rays to the electrons in the formation via elastic collisions. The number of scattered gamma rays that reach the detectors is directly related to the density of electrons in the formation that is in turn related to bulk density. Porosity may also be derived from this bulk density if the matrix (grain) density is known. The HLDT also measures photoelectric absorption as the photoelectric effect (PEF). Photoelectric absorption of the gamma rays occurs when they reach <150 keV, after being repeatedly scattered by electrons in the formation. Because the PEF depends on the atomic number of the elements in the formation, it also varies according to the chemical composition of the minerals present. For example, the photoelectric absorption cross-section index (Pe) of calcite = 5.08 b/e⁻; illite = 3.03 b/e⁻; quartz = 1.81 b/e⁻; and kaolinite = 1.49 b/e⁻. Good contact between the tool and borehole wall is essential for acquisition of quality HLDT logs; poor contact results in an underestimation of density values.

Porosity

Formation porosity was measured with the APS. This sonde incorporates a minitron neutron generator, which produces fast neutrons (14.4 MeV), and five neutron detectors (four epithermal and one thermal) positioned at differing intervals from the minitron. The measurement principle involves counting neutrons that arrive at the detectors after being slowed by neutron absorbers surrounding the tool. The highest energy loss occurs when neutrons collide with hydrogen nuclei that have practically the same mass as the neutron (the neutrons simply bounce off heavier elements without losing much energy). If the hydrogen (i.e., water) concentration is small, as in low-porosity formations, neutrons can travel farther before being captured and the count rates increase at the detector. The opposite effect occurs when the water content is high. However, because hydrogen bound in minerals such as clays or in hydrocarbons also contributes to the measurement, the raw porosity value is often an overestimate. Upon reaching thermal energies (0.025 keV), the neutrons are captured by the nuclei of chlorine, sili-

con, boron, and other elements, resulting in a gamma ray emission. This neutron capture cross section (Σf) is also measured by the tool.

Electrical Resistivity

The DIT provides three measures of electrical resistivity, each with a different depth of investigation into the formation. Two induction devices (deep and medium depths of penetration) transmit high-frequency alternating currents through transmitter coils, creating magnetic fields that induce secondary currents in the formation. These currents produce a new inductive signal proportional to the conductivity of the formation that is measured by the receiving coils. The measured conductivities are then inverted to resistivity. For the shallow penetration resistivity, the current necessary to maintain a constant voltage drop across a fixed interval is measured; it is a direct measurement of resistivity. Sand grains and hydrocarbons are electrical insulators, whereas ionic solutions and clays are conductors. Electrical resistivity can therefore be used to evaluate porosity, via Archie's Law, and fluid salinity.

Temperature, Acceleration, and Pressure

Downhole temperature, acceleration, and pressure were measured with the TAP tool. It was attached to the bottom of the triple combo tool string, with the recorded data stored in built-in memory. After the logging run was complete, the TAP tool was removed from the Schlumberger tools and returned to the DHML, where the data were downloaded.

The tool has a dual-temperature measurement system for identification of both rapid temperature fluctuations and temperature gradients. A thin fast-response thermistor detects small abrupt changes in temperature, and the thicker slow-response thermistor more accurately estimates temperature gradients and thermal regimes. A pressure transducer is used to activate the tool at a specified depth, typically 200 m above seafloor. A three-axis accelerometer measures tool movement downhole, which provides data for analyzing the effects of heave on the tool string. The long-term accumulation and analysis of these data, under varying cable lengths and heave conditions, will lead to enhanced performance of the WHC. Also, the acceleration log can aid in deconvolving heave effects postcruise, and it has proven at times to provide critical data. The temperature record must be interpreted with caution because the elapsed time between the end of drilling and the logging operation is generally not sufficient to allow the borehole to reach thermal equilibrium following circulation of the drilling fluid. The data recorded under such circumstances may differ significantly from the thermal equilibrium of that environment. Nevertheless, it is possible to identify abrupt temperature changes that may represent localized fluid flow into the borehole indicative of fluid pathways and fracturing and/or breaks in the temperature gradient that may correspond to contrasts in permeability at lithologic boundaries.

Acoustic Velocity

The LSS utilizes the "depth-derived" borehole compensation principle. Two transmitters spaced 2 ft (0.61 m) apart are located 8 ft (2.44 m) below two receivers that are also 2 ft (0.61 m) apart. Hole size compen-

sation is obtained by memorizing the first delay time reading and averaging it with a second reading measured after the tool has been pulled up to a fixed distance along the borehole. Because of the long spacing (10–12 ft; 3.04–3.66 m) between the transmitters and receivers, the tool has a wide investigation depth. The depth of the investigation is important, as drilling operations may damage the formation along the borehole wall, which will alter the acoustic velocity. Full waveforms are always recorded for each receiver. The LSS has been found to provide a reliable measurement of sonic traveltimes and has proved especially useful in the slower formations often encountered during paleoceanographic legs.

Formation MicroScanner

The FMS provides images of the borehole wall derived from high-resolution electrical resistivity. The tool has four orthogonal arms with pads, each containing 16 button electrodes, that are pressed against the borehole wall during the recording (Fig. F11). The electrodes are arranged in two diagonally offset rows of eight electrodes. A focused current is emitted from the button electrodes into the formation, with a return electrode located near the top of the tool. The intensity of current passing through the button electrodes is measured. Processing transforms these measurements, which reflect the microresistivity variations of the formation, into continuous spatially oriented high-resolution images that map geologic structures and lithologies along the borehole wall. Analysis of the processed FMS images can provide measurements of dip and direction (azimuth) of structural features in the formation.

The development of the FMS tool has added a new dimension to wireline logging (Luthi, 1990; Salimullah and Stow, 1992; Lovell et al., 1998). Features such as bedding, fracturing, slump folding, and bioturbation can be resolved, and spatially oriented images allow fabric analysis and bed orientation to be measured. The maximum extension of the caliper arms is 15 in, so in holes or parts of holes with larger diameter, the pad contact will be inconsistent and the FMS images may appear out of focus and too conductive. Irregular borehole walls will also adversely affect the image quality if they lead to poor pad/wall contact.

Acceleration and magnetic field measurements were made with the GPIT. The primary purpose of this tool, which incorporates a three-component accelerometer and a three-component magnetometer, is to determine the acceleration and orientation of the FMS-sonic tool string during logging. Acceleration and orientation data provide a means of correcting FMS images for irregular tool motion and allow the true dip and direction (azimuth) of structures to be determined.

Logging Data Quality

The principal influence on logging data quality is the condition of the borehole wall. If the borehole diameter is variable over short intervals, due to washouts during drilling, clay swelling, or ledges caused by layers of harder material, the logs from those tools that require good contact with the borehole wall (i.e., FMS, density, and porosity tools) may be degraded. Investigation measurements with greater formation penetration such as resistivity and sonic velocity, which do not require contact with the borehole wall, are generally less sensitive to borehole conditions. Very narrow (“bridged”) sections will also cause irregular logging results. The quality of the borehole is improved by minimizing

the circulation of drilling fluid while drilling, flushing the borehole to remove debris, and logging as soon as possible after drilling and hole conditioning. These procedures were followed in all logging operations during Leg 207.

Logging Depth Scales

The depth of the wireline-logged measurement is determined from the length of the logging cable payed out at the winch on the ship. The seafloor is identified on the natural gamma log by the abrupt reduction in gamma ray count at the water/sediment boundary (mudline). The coring depth (drillers depth) is determined from the known length of the bottom-hole assembly and pipe stands. The mudline is usually recovered in the first core from the hole.

Discrepancies between the drillers depth of recovered core and the wireline logging depth occur because of core expansion, incomplete core recovery, tidal changes, drill pipe stretch in the case of drill pipe depth, cable stretch (~1 m/km), cable slip in the case of logging depth, and incomplete heave compensation. To minimize the wireline tool motion caused by ship heave, the WHC adjusts for rig motion during wireline logging operations. Differences between drill pipe depth and logging depth should be taken into account when using the logs for correlation between core and logging data. The depths of core data sets, such as density and natural gamma ray, can be correlated with the equivalent downhole logs using the software program SAGAN, which allows shifting of the core depths onto the logging depth scale. Precise core-log depth matching is difficult in zones where core recovery is low because of the inherent ambiguity of placing the recovered section in the cored interval. Where complete core recovery (via a composite depth splice) is achieved, core depths and densities can be corrected by correlation with the logging data (e.g., Hagelberg et al., 1992).

Logs from different wireline tool strings will have slight depth mismatches. Distinctive features recorded by the natural gamma tools run on every tool string (except the WST) provide relative depth offsets and a means of depth shifting for correlation between logging runs.

Data Recording and Processing

Data for each logging run are recorded, stored digitally, and monitored in real time using the MCM software. On completion of logging in each hole, data processing by the shipboard Schlumberger engineer is carried out and data are transferred to the DHML and transmitted via satellite to LDEO-BRG for onshore processing. Data processing at LDEO-BRG consists of (1) depth shifting all logs relative to a common datum (i.e., mbsf), (2) making corrections specific to individual tools, and (3) quality control and rejection of unrealistic or spurious values. Once processed at LDEO-BRG, logging data are transmitted back to the ship, providing near-real time data processing. Further postcruise processing of the logging data from the FMS is performed at LDEO-BRG. Postcruise-processed logging data in ASCII are available directly from the LDEO-BRG Web site at www.ldeo.columbia.edu/BRG/ODP/DATABASE/. A summary of "logging highlights" is posted on the LDEO-BRG Web site at the end of each leg. Basic processing was conducted postcruise to provide scientists with a comprehensive quality controlled downhole logging data set that can be used for comparison, integration, and correlation with other data collected during Leg 207 and other ODP legs.

The processing includes additional depth adjustments as necessary to remove depth offsets between data from different logging runs and corrections specific to certain tools and logs. Documentation for the logs (with an assessment of logging quality), and conversion of the data to a widely accessible format are then performed. Schlumberger GeoQuest's GeoFrame software package is used for most of the processing. Processed acoustic, caliper, density, gamma ray, magnetic, neutron porosity, resistivity, and temperature data are available in ASCII, and FMS images are available as GIF files.

Core-Logging-Seismic Integration

The aim of creating a synthetic seismogram is to provide a means of matching the reflections expected from the formation (measured physical properties from logging and core sources) with those in the seismic data. This allows the seismic data to be interpreted in terms of measured formation properties; for example, lithologic or chronologic boundaries can be picked out as specific reflectors. If a synthetic seismogram can be generated for a number of sites, these data provide the basis for producing a regional seismic stratigraphy.

Velocity and density data are required to produce synthetic seismograms. These data are provided by and valid in downhole logging below the drill pipe, typically at ~60–70 mbsf. Core data were corrected for rebound (increased length with reduced density [e.g., Hamilton, 1976]) and temperature (increased temperature) changes and spliced onto the top of the logging data in order to provide full-depth velocity and density data sets. These full-depth data sets were then imported into the IESX module of the Schlumberger GeoQuest program GeoFrame to integrate with the seismic reflection data. Synthetic seismograms were generated with in-house software that convolves the velocity and density data with an Ormsby wavelet. This wavelet was designed to match the frequency content of the seismic data.

REFERENCES

- Acton, G.D., Borton, C.J., and the Leg 178 Shipboard Scientific Party, 2001. Palmer Deep composite depth scales for Leg 178 Sites 1098 and 1099. In Barker, P.F., Camerlenghi, A., Acton, G.D., and Ramsay, A.T.S. (Eds.), *Proc. ODP, Sci. Results*, 178 [Online]. Available from World Wide Web: <http://www-odptamu.edu/publications/178_SR/chap_05/chap_05.htm>. [Cited 2001-08-27]
- Acton, G.D., Okada, M., Clement, B.M., Lund, S.P., and Williams, T., 2002. Paleomagnetic overprints in ocean sediment cores and their relationship to shear deformation caused by piston cores. *J. Geophys. Res.*, 107:10.1029/2001JB000518.
- Alexandrovich, J.M., and Hays, J.D., 1989. High-resolution stratigraphic correlation of ODP Leg 111 Holes 677A and 677B and DSDP Leg 69 Hole 504. In Becker, K., Sakai, H., et al., *Proc. ODP, Sci. Results*, 111: College Station, TX (Ocean Drilling Program), 263–276.
- ASTM, 1990. Standard method for laboratory determination of water (moisture) content of soil and rock. *Annual Book of ASTM Standards* (Vol. 04.08): Philadelphia (Am. Soc. Testing and Mater.), D 2216–90 (revision of 2216–63, 2216–80).
- Aubry, M.-P., Berggren, W.A., Stott, L., and Sinha, A., 1996. The upper Paleocene–lower Eocene stratigraphic record and the Paleocene/Eocene boundary carbon isotope excursion: implications for geochronology. In Knox, R.W.O'B., Corfield, R.M., and Dunay, R.E. (Eds.), *Correlation of the Early Paleogene in Northwestern Europe*. Geol. Soc. Spec. Publ., 101:353–380.
- Backman, J., 1986. Late Paleocene to middle Eocene calcareous nannofossil biochronology from the Shatsky Rise, Walvis Ridge and Italy. *Palaeogeogr., Palaeoclimatol., Palaeoecol.*, 57:43–59.
- , 1987. Quantitative calcareous nannofossil biochronology of middle Eocene through early Oligocene sediment from DSDP Sites 522 and 523. *Abh. Geol. Bundesanst. (Austria)*, 39:21–31.
- Backman, J., and Raffi, I., 1997. Calibration of Miocene nannofossil events to orbitally tuned cyclostratigraphies from Ceara Rise. In Shackleton, N.J., Curry, W.B., Richter, C., and Bralower, T.J. (Eds.), *Proc. ODP, Sci. Results*, 154: College Station, TX (Ocean Drilling Program), 83–99.
- Backman, J., Schneider, D.A., Rio, D., and Okada, H., 1990. Neogene low-latitude magnetostratigraphy from Site 710 and revised age estimates of Miocene nannofossil datum events. In Duncan, R.A., Backman, J., Peterson, L.C., et al., *Proc. ODP, Sci. Results*, 115: College Station, TX (Ocean Drilling Program), 271–276.
- Balsam, W.L., and Damuth, J.E., 2000. Further investigations of shipboard vs. shore-based spectral data: implications for interpreting Leg 164 sediment composition. In Paull, C.K., Matsumoto, R., Wallace, P., and Dillon, W.P. (Eds.), *Proc. ODP, Sci. Results*, 164: College Station, TX (Ocean Drilling Program), 313–324.
- Balsam, W.L., Damuth, J.E., and Schneider, R.R., 1997. Comparison of shipboard vs. shore-based spectral data from Amazon-Fan cores: implications for interpreting sediment composition. In Flood, R.D., Piper, D.J.W., Klaus, A., and Peterson, L.C. (Eds.), *Proc. ODP, Sci. Results*, 155: College Station, TX (Ocean Drilling Program), 193–215.
- Balsam, W.L., Deaton, B.C., and Damuth, J.E., 1998. The effects of water content on diffuse reflectance measurements of deep-sea core samples: an example from ODP Leg 164 sediments. *Mar. Geol.*, 149:177–189.
- Barrera, E., and Savin, S.M., 1999. Evolution of Campanian–Maastrichtian marine climates and oceans. In Barrera, E., and Johnson, C.C. (Eds.), *Evolution of the Cretaceous Ocean–Climate System*. Spec. Pap.—Geol. Soc. Am., 332:245–282.
- Berggren, W.A., Hilgen, F.J., Langereis, C.G., Kent, D.V., Obradovich, J.D., Raffi, I., Raymo, M.E., and Shackleton, N.J., 1995a. Late Neogene chronology: new perspectives in high-resolution stratigraphy. *Geol. Soc. Am. Bull.*, 107:1272–1287.

- Berggren, W.A., Kent, D.V., Swisher, C.C., III, and Aubry, M.-P., 1995b. A revised Cenozoic geochronology and chronostratigraphy. *In* Berggren, W.A., Kent, D.V., Aubry, M.-P., and Hardenbol, J. (Eds.), *Geochronology, Time Scales and Global Stratigraphic Correlation*. Spec. Publ.—SEPM (Soc. Sediment. Geol.), 54:129–212.
- Berggren, W.A., and Norris, R.D., 1997. Biostratigraphy, phylogeny and systematics of Paleocene trochospiral planktic foraminifera. *Micropaleontology*, Suppl. 1, 43:1–116.
- Blum, P., 1997. Physical properties handbook: a guide to the shipboard measurement of physical properties of deep-sea cores. *ODP Tech. Note*, 26 [Online]. Available from World Wide Web: <<http://www-odp.tamu.edu/publications/tnotes/tn26/INDEX.HTM>>. [Cited 2001-09-02]
- Bolli, H.M., and Saunders, J.B., 1985. Oligocene to Holocene low latitude planktic foraminifera. *In* Bolli, H.M., Saunders, J.B., and Perch-Nielsen, K. (Eds.), *Plankton Stratigraphy*: Cambridge (Cambridge Univ. Press), 155–262.
- Bown, P.R. (Ed.), 1999. *Calcareous Nannofossil Biostratigraphy*: London (Chapman and Hall).
- Boyce, R.E., 1976. Definitions and laboratory techniques of compressional sound velocity parameters and wet-water content, wet-bulk density, and porosity parameters by gravimetric and gamma-ray attenuation techniques. *In* Schlanger, S.O., Jackson, E.D., et al., *Init. Repts. DSDP*, 33: Washington (U.S. Govt. Printing Office), 931–958.
- Bralower, T.J. 2002. Evidence for surface water oligotrophy during the Late Paleocene-Eocene Thermal Maximum: nannofossil assemblages data from Ocean Drilling Program Site 690, Maud Rise, Weddell Sea. *Paleoceanography*, 17:13-1–13-12.
- Bralower, T.J., Fullagar, P.D., Paull, C.K., Dwyer, G.S., and Leckie, R.M., 1997. Mid-Cretaceous strontium-isotope stratigraphy of deep-sea sections. *Geol. Soc. Am. Bull.*, 109:1421–1442.
- Bralower, T.J., Leckie, R.M., Sliter, W.V., and Thierstein, H.R., 1995. An integrated Cretaceous microfossil biostratigraphy. *In* Berggren, W.A., Kent, D.V., Aubry, M.-P., and Hardenbol, J. (Eds.), *Geochronology, Time Scales, and Global Stratigraphic Correlation*. Spec. Publ.—SEPM (Soc. Sediment. Geol.), 54:65–79.
- Bralower, T.J., Sliter, W.V., Arthur, M.A., Leckie, R.M., Allard, D.J., and Schlanger, S.O., 1993. Dysoxic/anoxic episodes in the Aptian–Albian (Early Cretaceous). *In* Pringle, M.S., Sager, W.W., Sliter, W.V., and Stein, S. (Eds.), *The Mesozoic Pacific: Geology, Tectonics, and Volcanism*. Geophys. Monogr., 77:5–37.
- Broecker, W.S., and Peng, T.-H., 1982. *Tracers in the Sea*: Palisades, NY (Eldigio Press).
- Bukry, D., 1973. Low-latitude coccolith biostratigraphic zonation. *In* Edgar, N.T., Saunders, J.B., et al., *Init. Repts. DSDP*, 15: Washington (U.S. Govt. Printing Office), 685–703.
- , 1975. Coccolith and silicoflagellate stratigraphy, northwestern Pacific Ocean, Deep Sea Drilling Project Leg 32. *In* Larson, R.L., Moberly, R., et al., *Init. Repts. DSDP*, 32: Washington (U.S. Govt. Printing Office), 677–701.
- , 1991. Paleoecological transect of western Pacific Ocean late Pliocene coccolith flora, Part I. Tropical Ontong-Java Plateau at ODP 806B. *Open-File Rep.—U.S. Geol. Surv.*, 91-552:1–35.
- Burnett, J.A., 1999. Upper Cretaceous. *In* Bown, P.R. (Ed.), *Calcareous Nannofossil Biostratigraphy*: London (Chapman and Hall), 132–199.
- Cande, S.C., and Kent, D.V., 1995. Revised calibration of the geomagnetic polarity timescale for the Late Cretaceous and Cenozoic. *J. Geophys. Res.*, 100:6093–6095.
- Carmichael, R.S., 1982. *Handbook of Physical Properties of Rocks* (Vol. 2): Boca Raton, FL (CRC Press).
- Caron, M., 1985. Cretaceous planktic foraminifera. *In* Bolli, H.M., Saunders, J.B., and Perch-Nielsen, K. (Eds.), *Plankton Stratigraphy*: Cambridge (Cambridge Univ. Press), 17–86.
- Chaisson, W.P., and Leckie, R.M., 1993. High-resolution Neogene planktonic foraminifer biostratigraphy of Site 806, Ontong Java Plateau (western equatorial

- Pacific). In Berger, W.H., Kroenke, L.W., Mayer, L.A., et al., *Proc. ODP, Sci. Results*, 130: College Station, TX (Ocean Drilling Program), 137–178.
- Chaisson, W.P., and Pearson, P.N., 1997. Planktonic foraminifer biostratigraphy at Site 925: middle Miocene–Pleistocene. In Shackleton, N.J., Curry, W.B., Richter, C., and Bralower, T.J. (Eds.), *Proc. ODP, Sci. Results*, 154: College Station, TX (Ocean Drilling Program), 3–31.
- Coolen, M.J.L., Cypionka, H., Sass, A.M., Sass, H., and Overmann, J., 2002. Ongoing modification of Mediterranean Pleistocene sapropels mediated by prokaryotes. *Science*, 296:2407–2410.
- Curry, W.B., Shackleton, N.J., Richter, C., et al., 1995. *Proc. ODP, Init. Repts.*, 154: College Station, TX (Ocean Drilling Program).
- Davis, E.E., Mottl, M.J., Fisher, A.T., et al., 1992. *Proc. ODP, Init. Repts.*, 139: College Station, TX (Ocean Drilling Program).
- Droser, M.L., and Bottjer, D.J., 1986. A semiquantitative field classification of ichnofabric. *J. Sediment. Petrol.*, 56:558–559.
- Ellis, D.V., 1987. *Well Logging for Earth Scientists*: New York (Elsevier).
- Emeis, K.-C., and Kvenvolden, K.A., 1986. Shipboard organic geochemistry on *JOIDES Resolution*. *ODP Tech. Note*, 7.
- Erba, E., Premoli Silva, I., and Watkins, D.K., 1995. Cretaceous calcareous plankton biostratigraphy of Sites 872 through 879. In Haggerty, J.A., Premoli Silva, I., Rack, F., and McNutt, M.K. (Eds.), *Proc. ODP, Sci. Results*, 144: College Station, TX (Ocean Drilling Program), 157–169.
- Erbacher, J., and Thurow, J., 1998. Mid-Cretaceous radiolarian zonation for the North Atlantic: an example of oceanographically controlled evolutionary processes in the marine biosphere? In Cramp, A., MacLeod, C.J., Lee, S.V., and Jones, E.J.W. (Eds.), *Geological Evolution of Ocean Basins: Results from the Ocean Drilling Program*. *Geol. Soc. Spec. Publ.*, 131:71–82.
- Espitalié, J., Deroo, G., and Marquis, F., 1986. La pyrolyse Rock-Eval et ses applications, Partie III. *Rev. Inst. Fr. Pet.*, 41:73–89.
- Exon, N.F., Kennett, J.P., Malone, M.J., et al., 2001. *Proc. ODP, Init. Repts.*, 189 [Online]. Available from World Wide Web: <http://www-odp.tamu.edu/publications/189_IR/189ir.htm>. [Cited 2003-01-02]
- Farrell, J.W., and Janecek, T.R., 1991. Late Neogene paleoceanography and paleoclimatology of the northeast Indian Ocean (Site 758). In Weissel, J., Peirce, J., Taylor, E., Alt, J., et al., *Proc. ODP, Sci. Results*, 121: College Station, TX (Ocean Drilling Program), 297–355.
- Frank, T.D., and Arthur, M.A., 1999. Tectonic forcings of Maastrichtian ocean-climate evolution. *Paleoceanography*, 14:103–117.
- Gieskes, J.M., Gamo, T., and Brumsack, H., 1991. Chemical methods for interstitial water analysis aboard *JOIDES Resolution*. *ODP Tech. Note*, 15 [Online]. Available from World Wide Web: <http://www-odp.tamu.edu/publications/tnotes/tn15/f_chem1.htm>. Cited [2003-01-02]
- Goldberg, D., 1990. Test performance of the Ocean Drilling Program wireline heave motion compensator. *Sci. Drill.*, 1:206–209.
- , 1997. The role of downhole measurements in marine geology and geophysics. *Rev. Geophys.*, 35:315–342.
- Hagelberg, T.K., Pisias, N.G., Shackleton, N.J., Mix, A.C., and Harris, S., 1995. Refinement of a high-resolution, continuous sedimentary section for studying equatorial Pacific Ocean paleoceanography, Leg 138. In Pisias, N.G., Mayer, L.A., Janecek, T.R., Palmer-Julson, A., and van Andel, T.H. (Eds.), *Proc. ODP, Sci Results*, 138: College Station, TX (Ocean Drilling Program), 31–46.
- Hagelberg, T., Shackleton, N., Pisias, N., and Shipboard Scientific Party, 1992. Development of composite depth sections for Sites 844 through 854. In Mayer, L., Pisias, N., Janecek, T., et al., *Proc. ODP, Init. Repts.*, 138 (Pt. 1): College Station, TX (Ocean Drilling Program), 79–85.

- Hamilton, E.L., 1976. Variations of density and porosity with depth in deep-sea sediments. *J. Sediment. Petrol.*, 46:280–300.
- Hilgen, F.J., 1991a. Astronomical calibration of Gauss to Matuyama sapropels in the Mediterranean and implication for the geomagnetic polarity time scale. *Earth Planet. Sci. Lett.*, 104:226–244.
- , 1991b. Extension of the astronomically calibrated (polarity) time scale to the Miocene/Pliocene boundary. *Earth Planet. Sci. Lett.*, 107:349–368.
- Hollis, C.J., 1993. Latest Cretaceous to late Paleocene radiolarian biostratigraphy: a new zonation from the New Zealand region. *Mar. Micropaleontol.*, 21:295–327.
- Hoppe, B.W., Blum, P., and the Shipboard Scientific Party, 1994. Natural gamma-ray measurements on ODP cores: introduction to procedures with examples from Leg 150. In Mountain, G.S., Miller, K.G., Blum, P., et al., *Proc. ODP, Init. Repts.*, 150: College Station, TX (Ocean Drilling Program), 51–59.
- Jansen, E., Raymo, M.E., Blum, P., et al., 1996. *Proc. ODP, Init. Repts.*, 162: College Station, TX (Ocean Drilling Program).
- Johnson, D.A., and Nigrini, C.A., 1985. Synchronous and time-transgressive Neogene radiolarian datum levels in the equatorial Indian and Pacific Oceans. *Mar. Micropaleontol.*, 9:489–523.
- Johnson, D.A., Schneider, D.A., Nigrini, C.A., Caulet, J.-P., and Kent, D.V., 1989. Pliocene–Pleistocene radiolarian events and magnetostratigraphic calibrations for the tropical Indian Ocean. *Mar. Micropaleontol.*, 14:33–66.
- Keene, J.B., 1975. Cherts and porcellanites from the North Pacific DSDP, Leg 32. In Larson, R.L., Moberly, R., et al., *Init. Repts. DSDP*, 32: Washington (U.S. Govt. Printing Office), 429–507.
- Kelly, D.C., Bralower, T.J., and Zachos, J.C., 1998. Evolutionary consequences of the Latest Paleocene Thermal Maximum for tropical planktonic foraminifera. *Palaeogeogr., Palaeoclimatol., Palaeoecol.*, 141:139–161.
- Kelly, D.C., Bralower, T.J., Zachos, J.C., Premoli Silva, I., and Thomas, E., 1996. Rapid diversification of planktonic foraminifera in the tropical Pacific (ODP Site 865) during the Late Paleocene Thermal Maximum. *Geology*, 24:423–426.
- Kennett, J.P., and Srinivasan, M.S., 1983. *Neogene Planktonic Foraminifera: A Phylogenetic Atlas*: Stroudsburg, PA (Hutchinson Ross).
- Kirschvink, J.L., 1980. The least-squares line and plane and the analysis of palaeomagnetic data. *Geophys. J. R. Astron. Soc.*, 62:699–718.
- Kristiansen, J.I., 1982. The transient cylindrical probe method for determination of thermal parameters of earth materials [Ph.D. dissert.]. Aarhus Univ.
- Kvenvolden, K.A., and McDonald, T.J., 1986. Organic geochemistry on the *JOIDES Resolution*—an assay. *ODP Tech. Note*, 6.
- Lazarus, D., Spencer-Cervato, C., Pianka-Biolzi, M., Beckmann, J.P., von Salis, K., Hilbrecht, H., and Thierstein, H., 1995. Revised chronology of Neogene DSDP holes from the world. *ODP Tech. Note*, 24 [Online]. Available from World Wide Web: <<http://www.ngdc.noaa.gov/mgg/geology/lazarus.html>>. Cited [2003-01-02]
- Leckie, R.M., 1984. Mid-Cretaceous planktonic foraminiferal biostratigraphy off central Morocco, DSDP Leg 79, Sites 545 and 547. In Winterer, E.L., Hinz, K., et al., *Init. Repts. DSDP*, 79: Washington (U.S. Govt. Printing Office), 579–620.
- Leckie, R.M., Farnham, C., and Schmidt, M.G., 1993. Oligocene planktonic foraminifer biostratigraphy of Hole 803D (Ontong Java Plateau) and Hole 628A (Little Bahama Bank), and comparison with the southern high latitudes. In Berger, W.H., Kroenke, L.V., and Mayer, L.A., *Proc. ODP, Sci. Results*, 130: College Station, TX (Ocean Drilling Program), 113–136.
- Longoria, J.F., 1974. Stratigraphic, morphologic and taxonomic studies of Aptian planktonic foraminifera. *Rev. Esp. Micropaleontol.*, Num. Extraordinario.
- Lourens, L.J., Antonarakou, A., Hilgen, F.J., Van Hoof, A.A.M., Vergnaud-Grazzini, C., and Zachariasse, W.J., 1996. Evaluation of the Plio-Pleistocene astronomical time-scale. *Paleoceanography*, 11:391–413.

- Lovell, M.A., Harvey, P.K., Brewer, T.S., Williams, C., Jackson, P.D., and Williamson, G., 1998. Application of FMS images in the Ocean Drilling Program: an overview. *In* Cramp, A., MacLeod, C.J., Lee, S.V., and Jones, E.J.W. (Eds.), *Geological Evolution of Ocean Basins: Results from the Ocean Drilling Program*. Geol. Soc. Spec. Publ., 131:287–303.
- Luthi, S.M., 1990. Sedimentary structures of clastic rocks identified from electrical borehole images. *In* Hurst, A., Lovell, M.A., and Morton, A.C. (Eds.), *Geological Applications of Wireline Logs*. Geol. Soc. Spec. Publ., 48:3–10.
- Lyle, M., Koizumi, I., Richter, C., et al., 1997. *Proc. ODP, Init. Repts.*, 167 [Online]. Available from World Wide Web: <http://www-odp.tamu.edu/publications/167_IR/167TOC.HTM>. [Cited 2003-01-02]
- Lyle, M., Wilson, P.A., Janecek, T.R., et al., 2002. *Proc. ODP, Init. Repts.*, 199 [Online]. Available from World Wide Web: <http://www-odp.tamu.edu/publications/199_IR/199ir.htm>. [Cited 2003-01-02]
- Mackenzie, K.V., 1981. Nine-term equation for sound speed in the oceans. *J. Acoust. Soc. Am.*, 70:807–812.
- MacLeod, K.G., and Huber, B.T., 2001. The Maastrichtian record at Blake Nose (western North Atlantic) and implications for global palaeoceanographic and biotic changes. *In* Kroon, D., Norris, R.D., and Klaus, A. (Eds.), *Western North Atlantic Paleogene and Cretaceous Paleooceanography*. Geol. Soc. Spec. Publ., 183:111–130.
- Manheim, F.T., and Sayles, F.L., 1974. Composition and origin of interstitial waters of marine sediments, based on deep sea drill cores. *In* Goldberg, E.D. (Ed.), *The Sea* (Vol. 5): *Marine Chemistry: The Sedimentary Cycle*. New York (Wiley), 527–568.
- Martini, E., 1971. Standard Tertiary and Quaternary calcareous nannoplankton zonation. *In* Farinacci, A. (Ed.), *Proc. 2nd Int. Conf. Planktonic Microfossils Roma*: Rome (Ed. Tecnosci.), 2:739–785.
- Mayer, L., Pisias, N., Janecek, T., et al., 1992. *Proc. ODP, Init. Repts.*, 138 (Pts. 1 and 2): College Station, TX (Ocean Drilling Program).
- Mazzullo, J.M., Meyer, A., and Kidd, R.B., 1988. New sediment classification scheme for the Ocean Drilling Program. *In* Mazzullo, J.M., and Graham, A.G. (Eds.), *Handbook for shipboard sedimentologists*. *ODP Tech. Note*, 8:45–67.
- Monechi, S., and Thierstein, H.R., 1985. Late Cretaceous–Eocene nannofossil and magnetostratigraphic correlations near Gubbio, Italy. *Mar. Micropaleontol.*, 9:419–440.
- Munsell Color Company, Inc., 1994. *Munsell Soil Color Chart* (Revised ed.): Newburgh, MD (Munsell Color).
- Murray, R.W., Miller, D.J., and Kryc, K.A., 2000. Analysis of major and trace elements in rocks, sediments, and interstitial waters by inductively coupled plasma–atomic emission spectrometry (ICP–AES). *ODP Tech. Note*, 29 [Online]. Available from World Wide Web: <<http://www-odp.tamu.edu/publications/tnotes/tn29/INDEX.HTM>>. [Cited 2001-10-15]
- Nederbragt, A.J., 1990. Biostratigraphy and paleoceanographic potential of the Cretaceous planktic foraminifera Heterohelicidae [Ph.D. thesis]. Centrale Huisdrukkerij Vrije Univ., Amsterdam.
- , 1991. Late Cretaceous biostratigraphy and development of Heterohelicidae planktic foraminifera. *Micropaleontology*, 37:329–372.
- Nigrini, C., and Sanfilippo, A., 2001. Cenozoic radiolarian stratigraphy for low and middle latitudes with descriptions of biomarkers and stratigraphically useful species. *ODP Tech. Note*, 27 [Online]. Available from World Wide Web: <<http://www-odp.tamu.edu/publications/tnotes/tn27/index.html>>. [Cited 2003-01-02]
- Nishimura, A., 1992. Paleocene radiolarian biostratigraphy in the northwest Atlantic at Site 384, Leg 43, of the Deep Sea Drilling Project. *Micropaleontology*, 38:317–362.
- Norris, R.D., 1998. Planktonic foraminifer biostratigraphy: eastern equatorial Atlantic. *In* Mascle, J., Lohmann, G.P., and Moullade, M. (Eds.), *Proc. ODP, Sci. Results*, 159, 445–479 [Online]. Available from World Wide Web: <http://www-odp.tamu.edu/publications/159_SR/CHAPTERS/CHAP_34.PDF>. [Cited 2003-01-02]

- Norris, R.D., Huber, B.T., and Self-Trail, J., 1999. Synchronicity of the K-T oceanic mass extinction and meteorite impact: Blake Nose, western North Atlantic. *Geology*, 27:419–422.
- Norris, R.D., and Röhl, U., 1999. Carbon cycling and chronology of climate warming during the Palaeocene/Eocene transition. *Nature*, 401:775–778.
- O'Dogherty, L., 1994. Biochronology and paleontology of middle Cretaceous radiolarians from Umbria-Marche Appennines (Italy) and Betic Cordillera (Spain). *Mem. Geol. Lausanne*, 21:1–351.
- Okada, H., and Bukry, D., 1980. Supplementary modification and introduction of code numbers to the low-latitude coccolith biostratigraphic zonation (Bukry, 1973; 1975). *Mar. Micropaleontol.*, 5:321–325.
- Olafsson, G., and Villa, G., 1992. Reliability of sphenoliths as zonal markers in Oligocene sediments from the Atlantic and Indian Oceans. In Proto Decima, F., Monechi, S., and Rio, D. (Eds.), *Proc. Int. Nannoplankton Assoc. Conf., Firenze 1989*. *Mem. Sci. Geol.*, 43:261–275.
- Olsson, R.K., Hemleben, C., Berggren, W.A., and Huber, B.T. (Eds.), 1999. *Atlas of Paleocene Planktonic Foraminifera*. Smithsonian. *Contrib. Paleobiol.*, Vol. 85.
- Pearson, P.N., 1995. Planktonic foraminifer biostratigraphy and the development of pelagic caps on guyots in the Marshall Islands group. In Haggerty, J., Premoli Silva, I., Rack, F., and McNutt, M.K. (Eds.), *Proc. ODP, Sci. Results*, 144: College Station, TX (Ocean Drilling Program), 21–59.
- Pearson, P.N., and Chaisson, W.P., 1997. Late Paleocene to middle Miocene planktonic foraminifer biostratigraphy of the Ceara Rise. In Shackleton, N.J., Curry, W.B., Richter, C., and Bralower, T.J. (Eds.), *Proc. ODP, Sci. Results*, 154: College Station, TX (Ocean Drilling Program), 33–68.
- Perch-Nielsen, K., 1985. Cenozoic calcareous nannofossils. In Bolli, H.M., Saunders, J.B., and Perch-Nielsen, K. (Eds.), *Plankton Stratigraphy*: Cambridge (Cambridge Univ. Press), 427–554.
- Peters, K.E., 1986. Guidelines for evaluating petroleum source rock using programmed pyrolysis. *AAPG Bull.*, 70:318–329.
- Petrizzo, M.R., 2000. Upper Turonian–lower Campanian planktonic foraminifera from southern mid-high latitudes (Exmouth Plateau, NW Australia): biostratigraphy and taxonomic notes. *Cretaceous Res.*, 21:479–505.
- Petschik, R., 2000. MacDiff 4.1.1 Manual. *MacDiff* [Online]. Available from World Wide Web: <<http://www.geologie.uni-frankfurt.de/Staff/Homepages/Petschick/RainerE.html>>. [Revised 2001-05-17]
- Pimmel, A., and Claypool, G., 2001. Introduction to shipboard organic geochemistry on the *JOIDES Resolution*. *ODP Tech. Note*, 30 [Online]. Available from World Wide Web: <<http://www-odp.tamu.edu/publications/tnotes/tn30/INDEX.HTM>>. [Cited 2001-08-27]
- Postuma, J.A., 1971. *Manual of Planktonic Foraminifera*: Amsterdam (Elsevier).
- Premoli Silva, I., and Sliter, W.V., 1994. Cretaceous planktonic foraminiferal biostratigraphy and evolutionary trends from the Bottaccione Section, Gubbio, Italy. *Palaeontogr. Ital.*, 82:2–90.
- Premoli Silva, I., and Sliter, W.V., 1999. Cretaceous paleoceanography: evidence from planktonic foraminiferal evolution. In Barrera, E., and Johnson, C.C. (Eds.), *The Evolution of Cretaceous Ocean-Climatic System*. *Spec. Pap.—Geol. Soc. Am.*, 332:301–328.
- Raffi, I., Backman, J., Rio, D., and Shackleton, N.J., 1993. Plio-Pleistocene nannofossil biostratigraphy and calibration to oxygen isotopes stratigraphies from Deep Sea Drilling Project Site 607 and Ocean Drilling Program Site 677. *Paleoceanography*, 8:387–408.
- Raffi, I., and Flores, J.-A., 1995. Pleistocene through Miocene calcareous nannofossils from eastern equatorial Pacific Ocean. In Pisias, N.G., Mayer, L.A., Janecek, T.R., Palmer-Julson, A., and van Andel, T.H. (Eds.), *Proc. ODP, Sci. Results*, 138: College Station, TX (Ocean Drilling Program), 233–286.

- Rider, M.H., 1996. *The Geological Interpretation of Well Logs* (2nd ed.): Caithness (Whittles Publishing).
- Robaszynski, F., Caron, M. (Coord.), and the European Working Group on Planktonic Foraminifera, 1979. *Atlas de Foraminifères Planctoniques du Crétacé Moyen* (Vols. 1 and 2). Cah. Micropaleontol.
- Robaszynski, F., Caron, M., Gonzales-Donoso, J.-M., Wonders, A.A.H., and the European Working Group on Planktonic Foraminifera, 1984. *Atlas of Late Cretaceous Globotruncanids*. Rev. Micropaleontol., 26:145–305.
- Röhl, U., Bralower, T.J., Norris, R.D., and Wefer, G., 2000. New chronology for the Late Paleocene Thermal Maximum and its environmental implications. *Geology*, 28:927–930.
- Roth, P.H., 1978. Cretaceous nannoplankton biostratigraphy and oceanography of the northwestern Atlantic Ocean. In Benson, W.E., Sheridan, R.E., et al., *Init. Repts. DSDP*, 44: Washington (U.S. Govt. Printing Office), 731–759.
- , 1983. Jurassic and Lower Cretaceous calcareous nannofossils in the western North Atlantic (Site 534): biostratigraphy, preservation, and some observations on biogeography and paleoceanography. In Sheridan, R.E., Gradstein, F.M., et al., *Init. Repts. DSDP*, 76: Washington (U.S. Govt. Printing Office), 587–621.
- Ruddiman, W.F., Cameron, D., and Clement, B.M., 1987. Sediment disturbance and correlation of offset holes drilled with the hydraulic piston corer: Leg 94. In Ruddiman, W.F., Kidd, R.B., Thomas, E., et al., *Init. Repts. DSDP*, 94 (Pt. 2): Washington (U.S. Govt. Printing Office), 615–634.
- Salimullah, A.R.M., and Stow, D.A.V., 1992. Application of FMS images in poorly recovered coring intervals: examples from ODP Leg 129. In Hurst, A., Griffiths, C.M., and Worthington, P.F. (Eds.), *Geological Application of Wireline Logs II*. Geol. Soc. Spec. Publ., 65:71–86.
- Sanfilippo, A., and Blome, C.D., 2001. Biostratigraphic implications of mid-latitude Palaeocene–Eocene radiolarian faunas from Hole 1051A, ODP Leg 171B, Blake Nose, western North Atlantic. In Kroon, D., Norris, R.D., and Klaus, A. (Eds.), *Western North Atlantic Paleogene and Cretaceous Paleooceanography*. Geol. Soc. Spec. Publ., 183:185–224.
- Sanfilippo, A., and Nigrini, C., 1995. Radiolarian stratigraphy across the Oligocene/Miocene transition. *Mar. Micropaleontol.*, 24:239–285.
- , 1996. Radiolarian biomarkers at the Oligocene/Miocene boundary. In Moguilevsky, A., Watley, R. (Eds.), *Microfossils and Oceanic Environments: Proc. ODP and the Mar. Biosphere Int. Conf.*: Aberystwyth, Wales (Univ. Wales, Aberystwyth Press), 317–326.
- , 1998. Code numbers for Cenozoic low latitude radiolarian biostratigraphic zones and GPTS conversion tables. *Mar. Micropaleontol.*, 33:109–156.
- Sanfilippo, A., and Riedel, W.R., 1985. Cretaceous radiolaria. In Bolli, H.M., Saunders, J.B., and Perch-Nielsen, K. (Eds.), *Plankton Stratigraphy*: Cambridge (Cambridge Univ. Press), 573–630.
- Schlumberger, 1989. *Log Interpretation Principles/Applications*: Houston (Schlumberger Educ. Services), SMP-7017.
- , 1994. *IPL Integrated Porosity Lithology*: Houston (Schlumberger Wireline and Testing), SMP-9270.
- Serra, O., 1984. *Fundamentals of Well-Log Interpretation* (Vol. 1): *The Acquisition of Logging Data*. Dev. Pet. Sci., 15A.
- , 1986. *Fundamentals of Well-Log Interpretation* (Vol. 2): *The Interpretation of Logging Data*. Dev. Pet. Sci., 15B.
- , 1989. *Formation MicroScanner Image Interpretation*: Houston (Schlumberger Educ. Services), SMP-7028.
- Shackleton, N.J., Berger, A., and Peltier, W.A., 1990. An alternative astronomical calibration of the lower Pleistocene timescale based on ODP Site 677. *Trans. R. Soc. Edinburgh: Earth Sci.*, 81:251–261.

- Shackleton, N.J., Crowhurst, S., Hagelberg, T., Pias, N.G., and Schneider, D.A., 1995. A new late Neogene time scale: application to Leg 138 sites. *In* Pias, N.G., Mayer, L.A., Janecek, T.R., Palmer-Julson, A., and van Andel, T.H. (Eds.), *Proc. ODP, Sci. Results*, 138: College Station, TX (Ocean Drilling Program), 73–101.
- Shackleton, N.J., Crowhurst, S.J., Weedon, G.P., and Laskar, J., 1999. Astronomical calibration of Oligocene–Miocene time. *Philos. Trans. R. Soc. London, Ser. A*, 357:1907–1929.
- Shipboard Scientific Party, 1992. Explanatory notes. *In* Mayer, L., Pias, N., Janecek, T., et al., *Proc. ODP, Init. Repts.*, 138 (Pt. 1): College Station, TX (Ocean Drilling Program), 13–42.
- , 1999. Explanatory notes. *In* Hodell, D., Gersonde, R., Blum, P., et al., *ODP Proc. Init. Repts.*, 177: College Station, TX (Ocean Drilling Program).
- , 2001. Explanatory notes. *In* Exxon, N.F., Kennett, J.P., Malone, M.J., et al., *Proc. ODP, Init. Repts.*, 189, 1–59 [Online]. Available from World Wide Web: <http://www-odp.tamu.edu/publications/189_IR/VOLUME/CHAPTERS/IR189_02.PDF>. [Cited 2003-01-02]
- Sissingh, W., 1977. Biostratigraphy of Cretaceous calcareous nannoplankton. *Geol. Mijnbouw*, 56:37–65.
- Sliter, W.V., 1989. Biostratigraphic zonation for Cretaceous planktonic foraminifers examined in thin section. *J. Foraminiferal Res.*, 19:1–19.
- Speijer, R.P., Schmitz, B., and van der Zwaan, G.J., 1997. Benthic foraminiferal extinction and repopulation in response to latest Paleocene Tethyan anoxia. *Geology*, 25:683–686.
- Spezzaferri, S., 1994. Planktonic foraminiferal biostratigraphy and taxonomy of the Oligocene and lower Miocene in the oceanic record: an overview. *Palaeontographica Ital.*, 81:1–187.
- Spezzaferri, S., and Premoli Silva, I., 1991. Oligocene planktonic foraminiferal biostratigraphy and paleoclimatic interpretation from Hole 538A, DSDP Leg 77, Gulf of Mexico. *Palaeogeogr., Palaeoclimatol., Palaeoecol.*, 83:217–263.
- Stein, R., Brass, G., Graham, D., Pimmel, A., and the Shipboard Scientific Party, 1995. Hydrocarbon measurements at Arctic Gateways sites (ODP Leg 151). *In* Myhre, A.M., Thiede, J., Firth, J.V., et al., *Proc. ODP, Init. Repts.*, 151: College Station, TX (Ocean Drilling Program), 385–395.
- Tauxe, L., Tucker, P., Petersen, N.P., and LaBrecque, J.L., 1984. Magnetostratigraphy of Leg 73 sediments. *In* Hsü, K.J., LaBrecque, J.L., et al., *Init. Repts. DSDP*, 73: Washington (U.S. Govt. Printing Office), 609–621.
- Thierstein, H.R., Geitzenauer, K., Molfino, B., and Shackleton, N.J., 1977. Global synchronicity of late Quaternary coccolith datum levels: validation by oxygen isotopes. *Geology*, 5:400–404.
- Tiedemann, R., Sarnthein, M., and Shackleton, N.J., 1994. Astronomic timescale for the Pliocene Atlantic $\delta^{18}\text{O}$ and dust flux records of Ocean Drilling Program Site 659. *Paleoceanography*, 9:619–638.
- Toumarkine, M., and Luterbacher, H., 1985. Paleocene and Eocene planktic foraminifera. *In* Bolli, H.M., Saunders, J.B., and Perch-Nielsen, K. (Eds.), *Plankton Stratigraphy*: Cambridge (Cambridge Univ. Press), 87–154.
- Tréhu, A.M., Bohrmann, G., Rack, F.R., Torres, M.E., et al., 2003. *Proc. ODP, Init. Repts.*, 204 [CD-ROM]. Available from: Ocean Drilling Program, Texas A&M University, College Station TX 77845-9547, USA.
- Van Couvering, J.A., Castradori, D., Cita, M.B., Hilgen, F.J., and Rio, D., 2000. The base of the Zanclean stage and the Pliocene series. *Episodes*, 23:179–187.
- Von Herzen, R.P., and Maxwell, A.E., 1959. The measurement of thermal conductivity of deep-sea sediments by a needle-probe method. *J. Geophys. Res.*, 64:1557–1563.
- Wentworth, C.K., 1922. A scale of grade and class terms of clastic sediments. *J. Geol.*, 30:377–392.
- Wilson, W.D., 1960. Speed of sound in seawater as a function of temperature, pressure and salinity. *J. Acoust. Soc. Am.*, 32:641–644.

Wyllie, M.R.J., Gregory, A.R., and Gardner, L.W., 1956. Elastic wave velocities in heterogeneous and porous media. *Geophysics*, 21:41–70.

Figure F2. Key to symbols used for graphic lithologies on the computer-generated core description forms.

Lithology

	Nannofossil ooze		Limestone		Siltstone		Siliceous ooze
	Nannofoam ooze		Clay or claystone		Sandstone		Radiolarite
	Calcareous ooze		Silty claystone		Conglomerate		Chert
	Nannofossil chalk		Interval taken as a whole-round sample		Radiolarian ooze		Porcellanite
	Nannofoam chalk		Void				
	Calcareous chalk		Shale				

Figure F3. Key to symbols used for contacts, physical structures, lithologic accessories, ichnofossils, fossils, core disturbance, and bioturbation on the computer-generated core description forms.

Contacts

 Sharp  Gradational

Physical structures

 Slump	 Fault (w/ displacement if observed)	
 Cross lamination	 Mineral-filled vein	 Chaotic bedding
 Coarsening-upward sequence	 Planar lamination	 Graded bedding
 Scour	 Organic-rich lamination	 Flaser bedding

Ichnofossils

 <i>Planolites</i>	 <i>Chondrites</i>	 <i>Zoophycos</i>
 <i>Thalassinoides</i>	 Mottled	 Undefined burrow

Lithologic accessories

 Shell fragments	 Cherty	 Py Pyrite
 Coprolitic material	 Chalcedony/chert concretion	 Gl Glauconite
 Horizontal dark band	 Nodule/concretion, general	 Fe Ferruginous
 Calciite cement	 Pyrite concretion	

Core disturbance

 Disturbed	 Fractured	 Deformed
 Soupy	 Biscuit	 Slurry

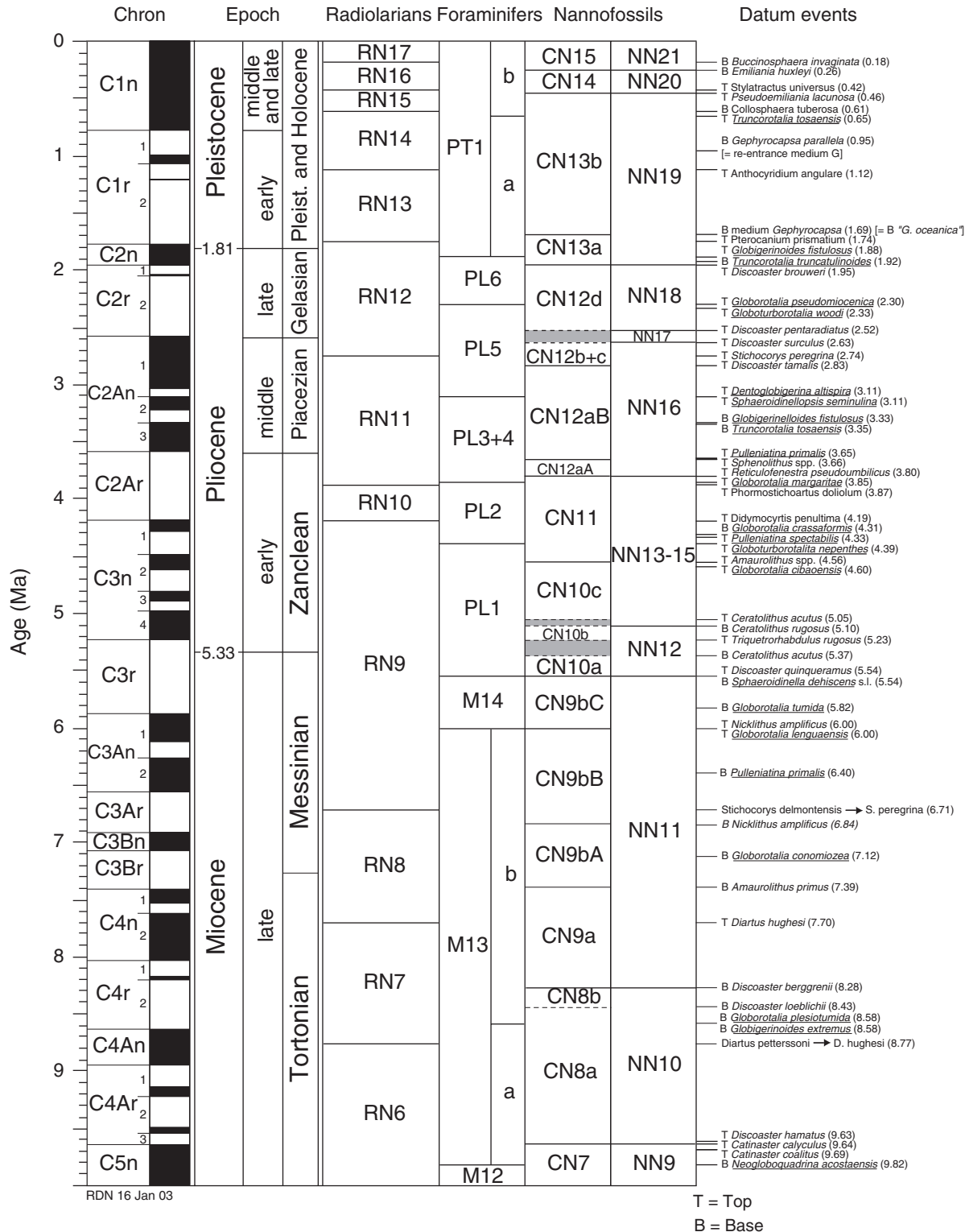
Bioturbation

 Pervasive  Heavy  Moderate  Slight   Absent

Figure F4. Grain-size divisions for sedimentary rocks (adapted from Wentworth, 1922).

Millimeters (mm)	Micrometers (μm)	Phi (ϕ)	Wentworth size class	Rock type
4096		-12.0	Boulder	Conglomerate/ Breccia
256		-8.0	Cobble	
64		-6.0	Pebble	
4		-2.0	Granule	
2.00		-1.0		
1.00		0.0	Very coarse sand	Sandstone
1/2	0.50	1.0	Coarse sand	
1/4	0.25	2.0	Medium sand	
1/8	0.125	3.0	Fine sand	
1/16	0.0625	4.0	Very fine sand	
1/32	0.031	5.0	Coarse silt	Siltstone
1/64	0.0156	6.0	Medium silt	
1/128	0.0078	7.0	Fine silt	
1/256	0.0039	8.0	Very fine silt	
0.00006	0.06	14.0	Clay	Claystone

Figure F5. Calcareous nannofossil, planktonic foraminifer, and radiolarian zonations used during Leg 207. References are cited in the text for each microfossil group. T = LO datum or "Top," B = FO datum or "Base," TA = Top acme, X = crossover in relative abundance of two species. An arrow between radiolarian species names indicates an evolutionary transition from the species on the left to the species on the right. Gray bands and dashed lines = zonal boundaries are not clearly delimited in a given zonation. SCWL = Shackleton et al. (1999) alternative dating of events surrounding the Miocene/Oligocene boundary. (Continued on next five pages.)



RDN 16 Jan 03

T = Top
B = Base

Figure F5 (continued).

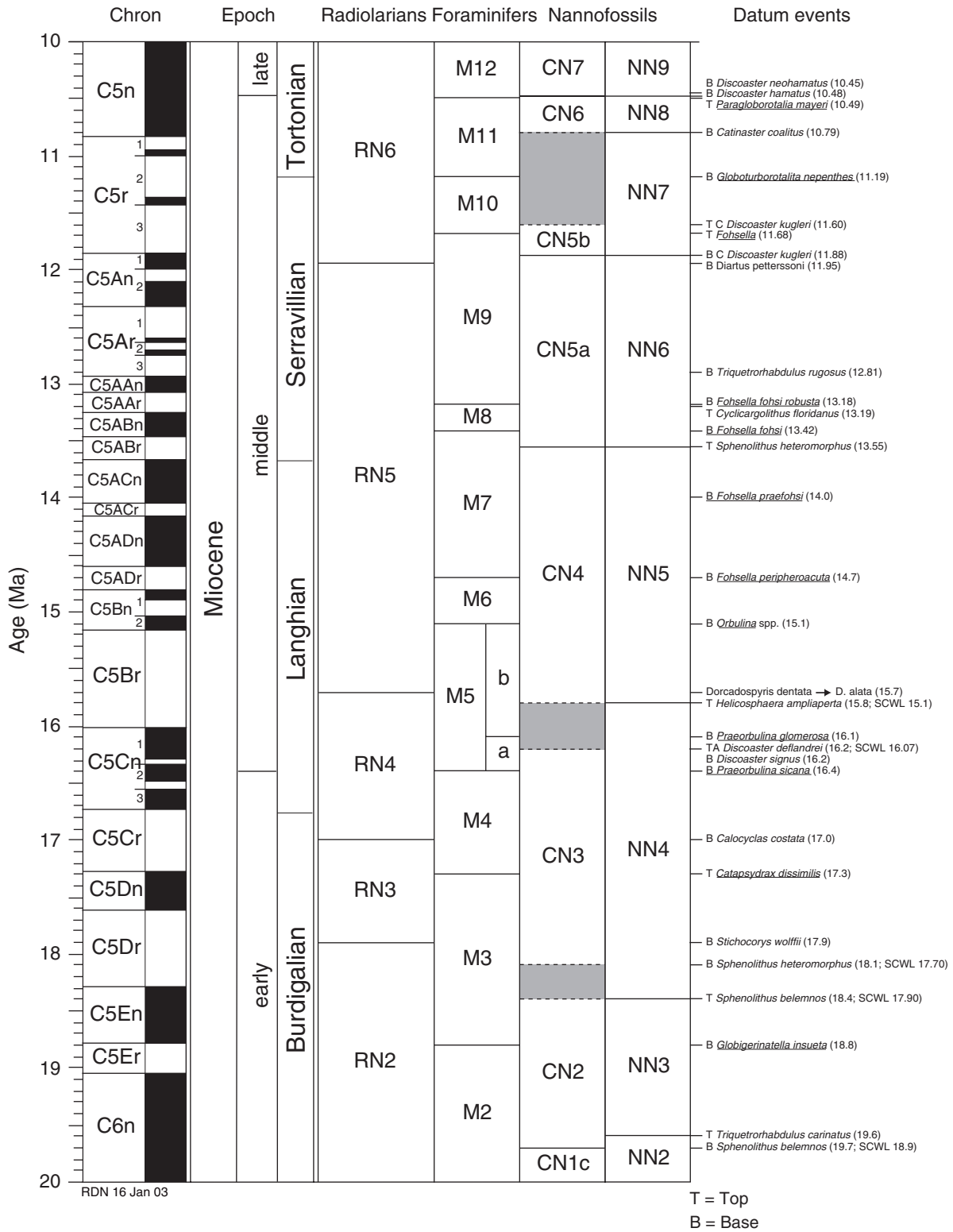


Figure F5 (continued).

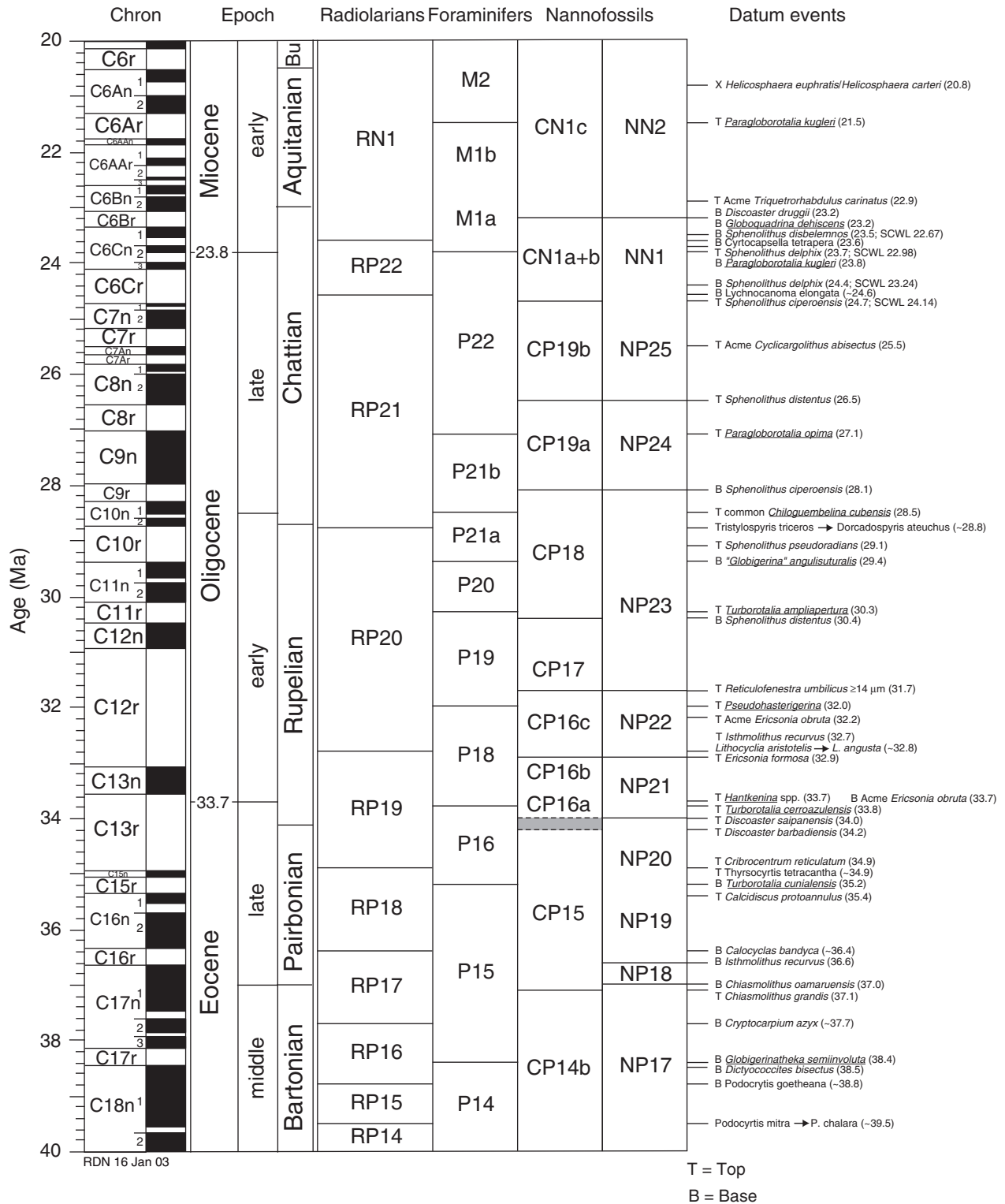


Figure F5 (continued).

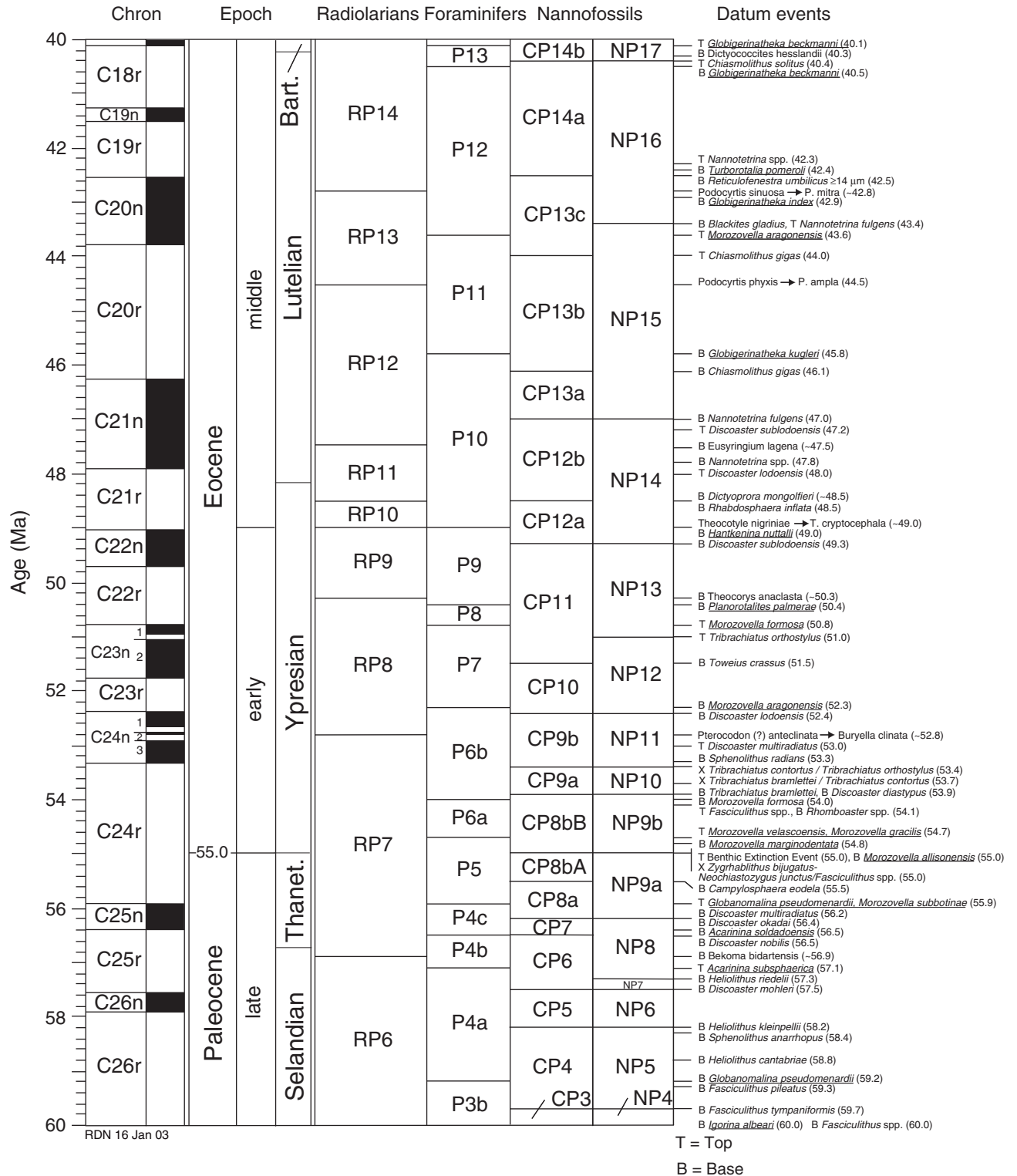


Figure F5 (continued).

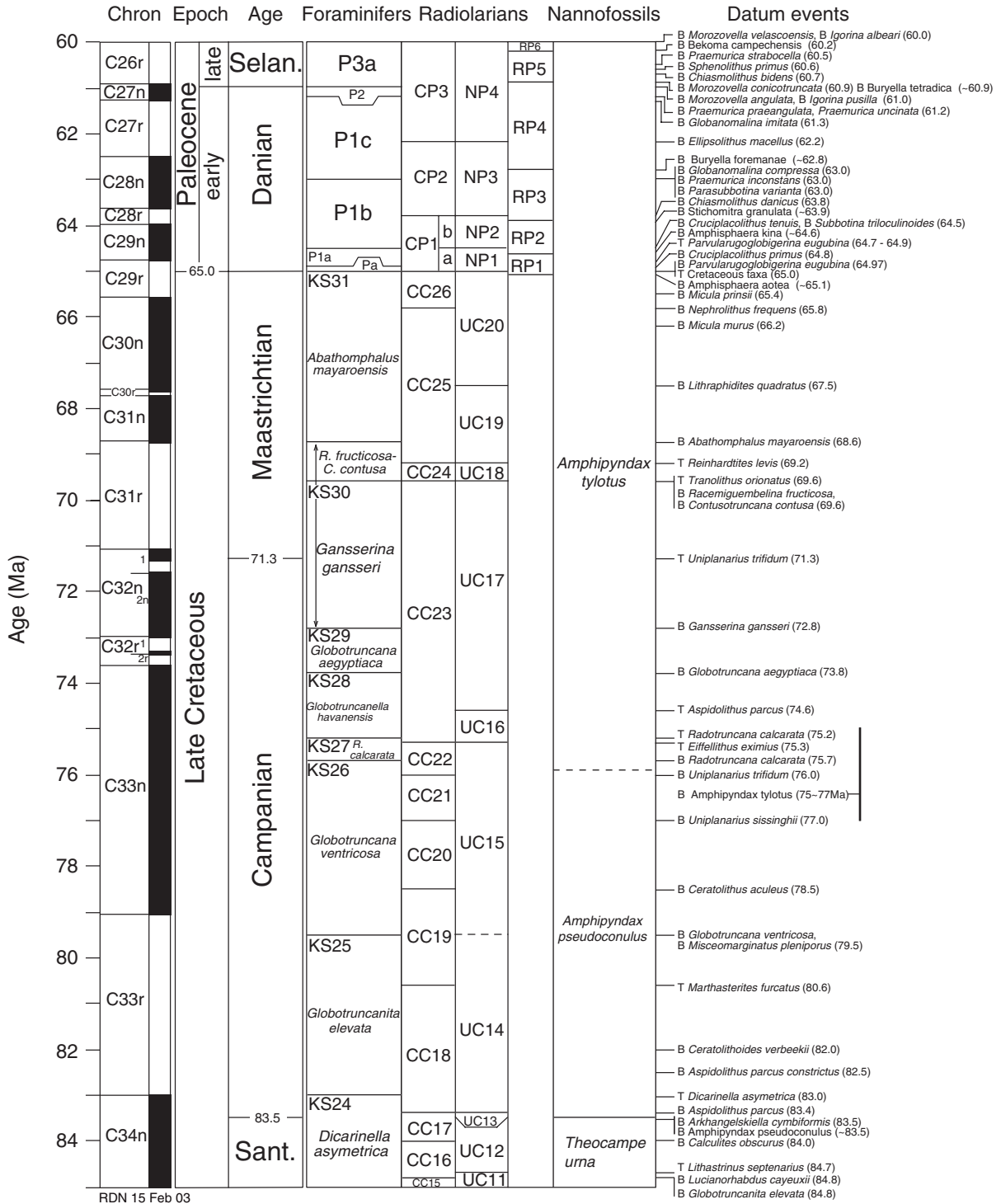


Figure F5 (continued).

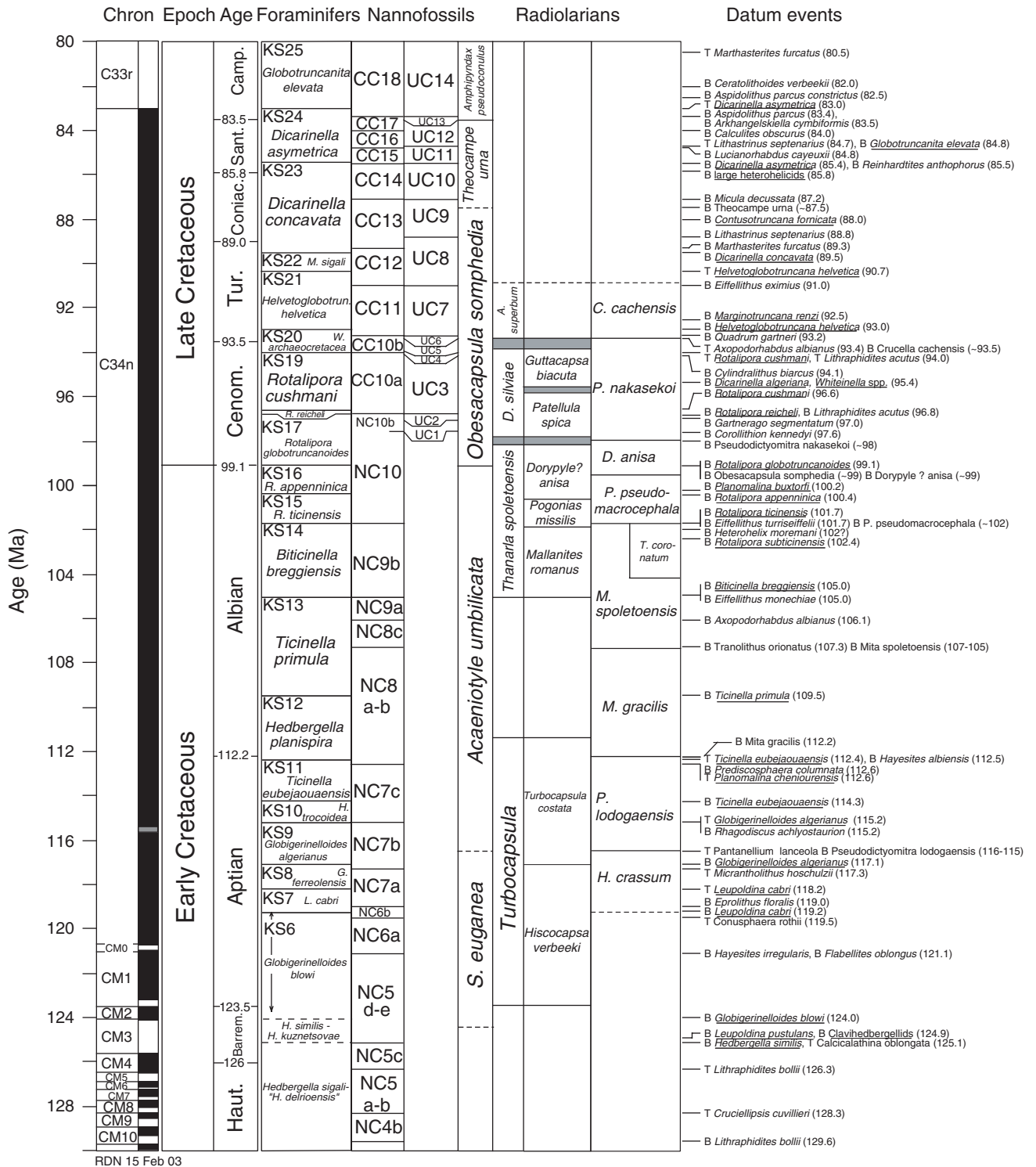


Figure F6. Orientation systems for paleomagnetic analyses. Archive halves are measured with the shipboard pass-through magnetometer, and working halves are sampled for minicores and cubes for shore-based analyses.

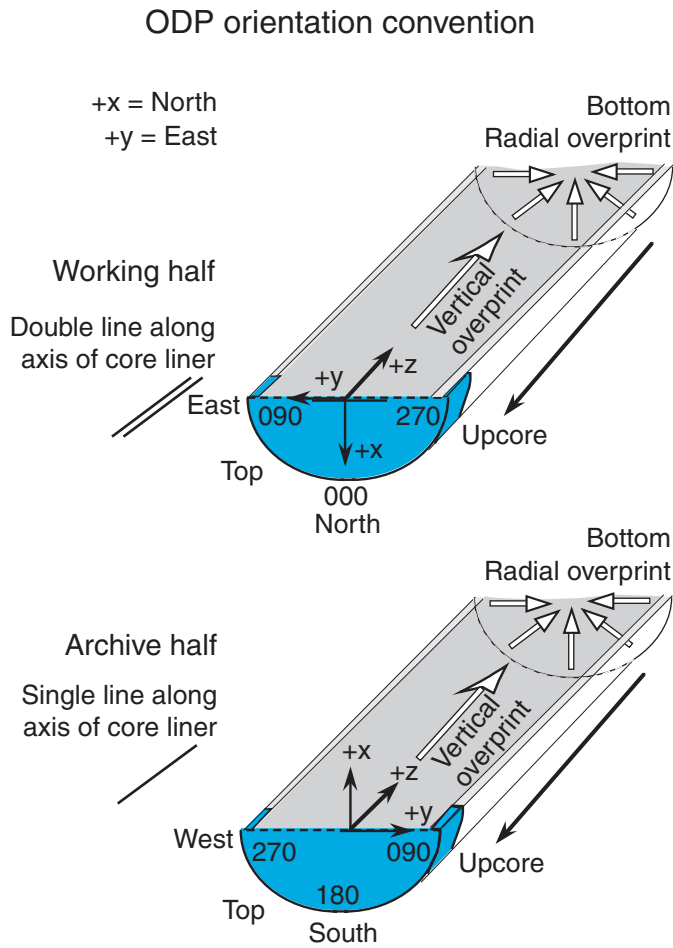
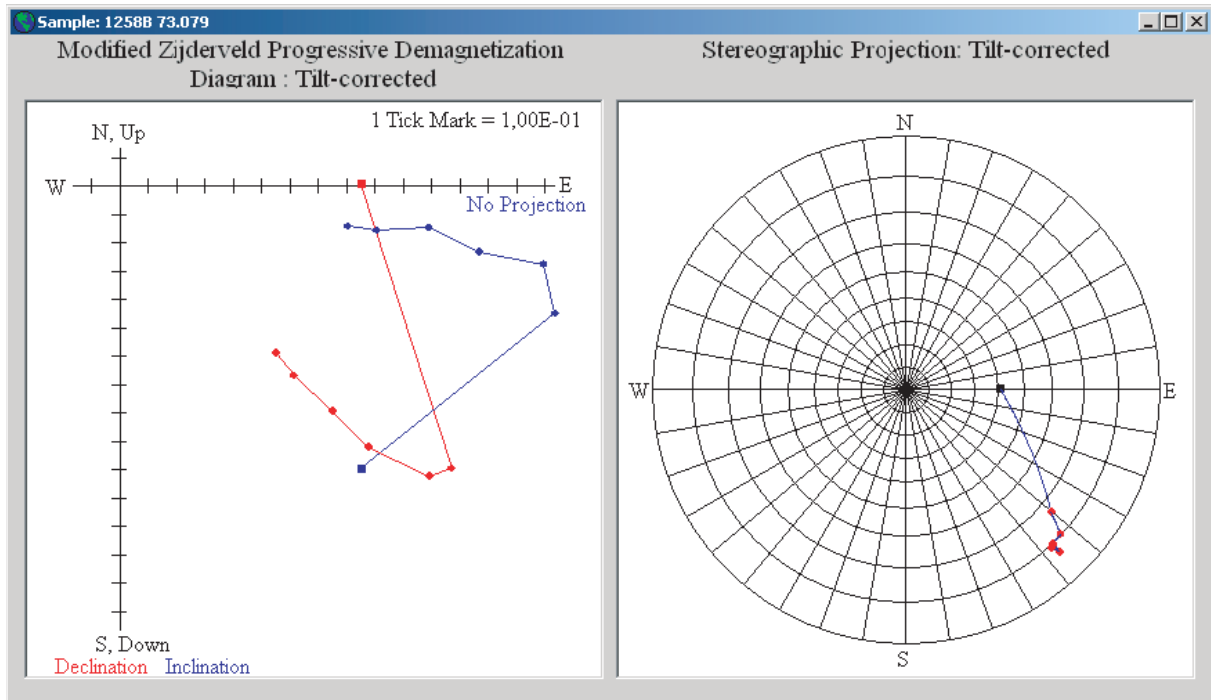


Figure F7. Selected vector plots and stereo diagrams of thermal demagnetization behavior of Eocene chalk samples. Plots are screen images from PALEOMAG software (www.eas.purdue.edu/paleomag/). In the vector plots, the declination and inclination components (red and blue curves, respectively) of the magnetization vector correspond to the horizontal component and to the actual dip of the magnetization vector; scale divisions are in mA/m, unless otherwise noted. Demagnetization procedures are NRM (square point at end), 5 mT AF, 150°C, then progressive 50° steps to 400°C or 450°C. The characteristic directions from Eocene sediments recovered during Leg 207 generally have negative inclinations associated with normal polarity behaviors and positive inclinations with reversed polarity. **A.** Example of a typical “hook-type” curve that is interpreted as unblocking of a downward normal polarity overprint from a positive inclination reversed polarity characteristic direction. Magnetic intensity increases immediately after an initial shift in declination accompanying an inclination shallowing. Sample 209-1258B-7R-3, 79 cm (early Eocene nannofossil chalk) has a characteristic magnetization (136.6° declination, 9.3° inclination, mean intensity = 1.0E+0 mA/m) derived from the last four steps (250°–400°C and tied to origin) and assigned an “R” polarity rating based on the univectorial decay. **B.** Example of a typical “N-type” curve that is interpreted as unblocking of a positive inclination normal polarity overprint from a negative inclination normal polarity characteristic direction. Sample 209-1258B-8R-3, 33 cm (early Eocene nannofossil chalk), has a characteristic magnetization (23.6° declination, –8.3° inclination, mean intensity = 1.0E+0 mA/m) derived from the last four steps (250°–400°C, tied to origin) and assigned an “N” polarity rating based on the univectorial decay. **C.** Example of an “R-type” curve. Declination progressively rotates as the vector initially decreases in intensity, then increases in intensity with a declination nearly opposite to the initial NRM. Further thermal demagnetization is univectorial decay. In contrast to the other plots, the inclination components have been projected onto a constant north–south plane to clearly illustrate the rotational behavior. Sample 209-1259A-26R-1, 13 cm (middle Eocene nannofossil chalk) has a characteristic magnetization (138.8° declination, 15.1° inclination, mean intensity = 1.4E–2 mA/m) derived from the last five steps (200°–400°C, tied to origin) and assigned an “R” polarity rating based on the univectorial decay. **D.** Example of a subtle “hook-type” curve. Stable declination would appear to suggest a normal polarity sample, but the early demagnetization steps caused an increase in magnetic intensity during shallowing of the inclination. This initial increase in intensity implies that a vector of opposite declination is being removed, which is interpreted as the normal polarity overprint on a reversed polarity characteristic direction. Sample 209-1258B-10R-4, 98 cm (early Eocene nannofossil chalk), has a characteristic magnetization (243.0° declination, 15.5° inclination, mean intensity = 1.1E+0 mA/m) derived from the last five steps (250°–450°C, tied to origin) and assigned an “R” polarity rating based on the univectorial decay. (Figure shown on next two pages.)

Figure F7 (continued). (Caption shown on previous page.)

A



B

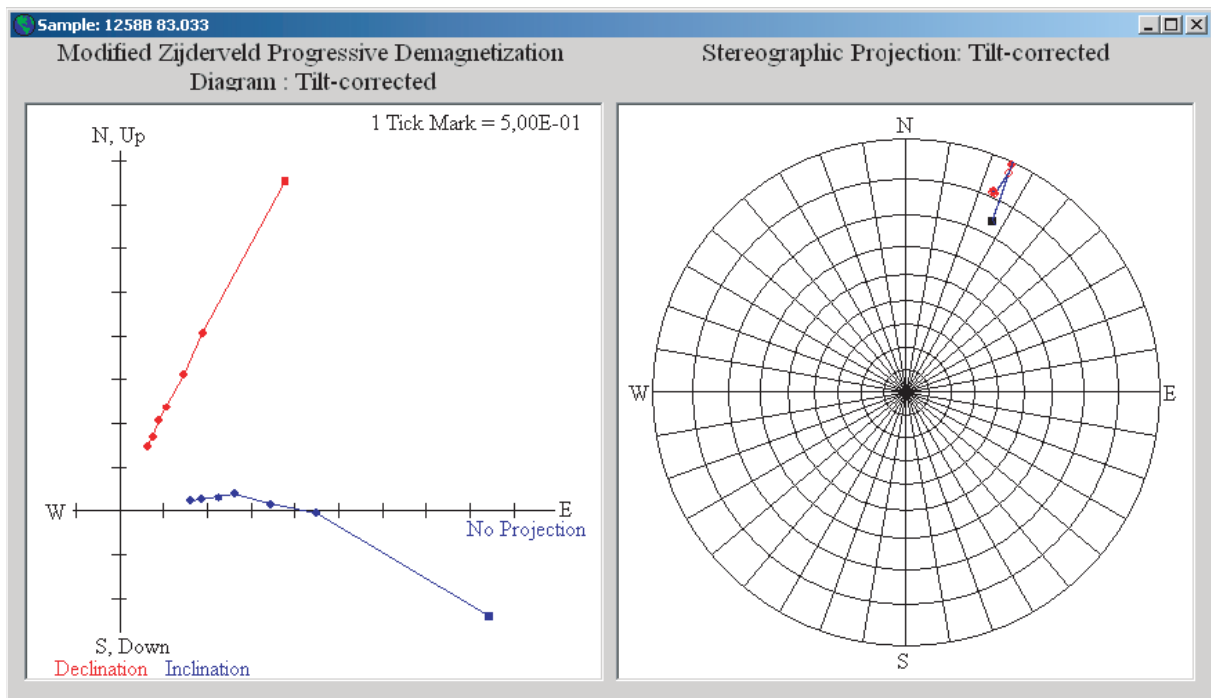
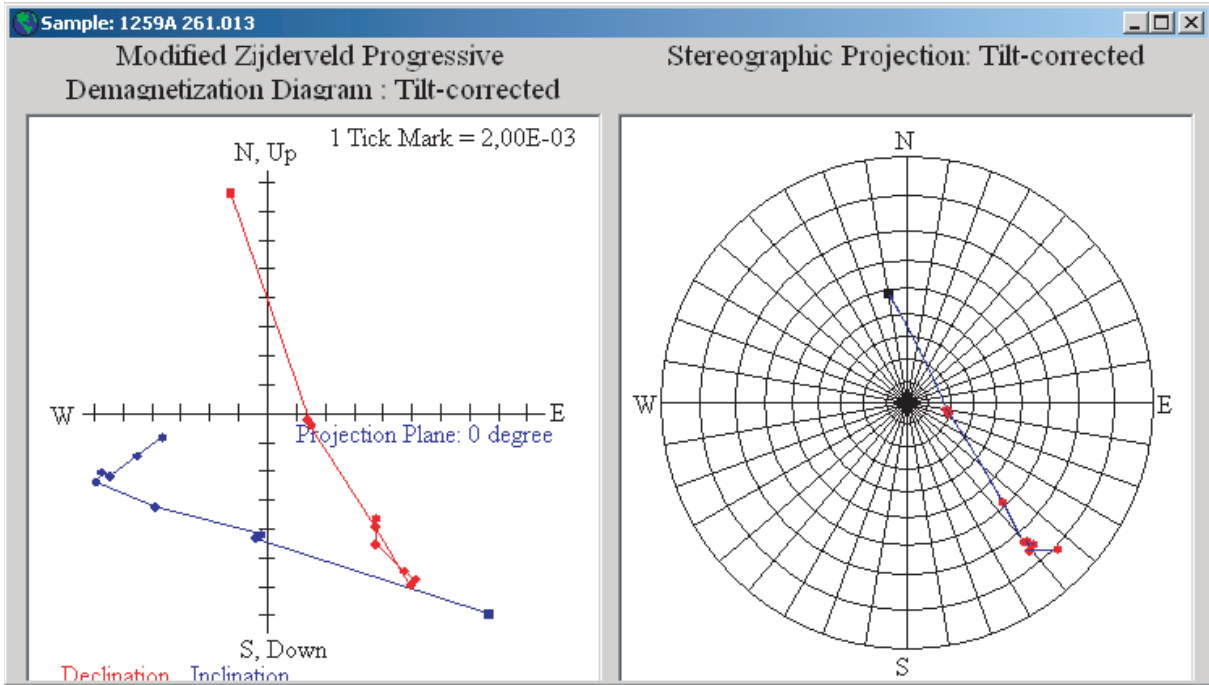


Figure F7 (continued).

C



D

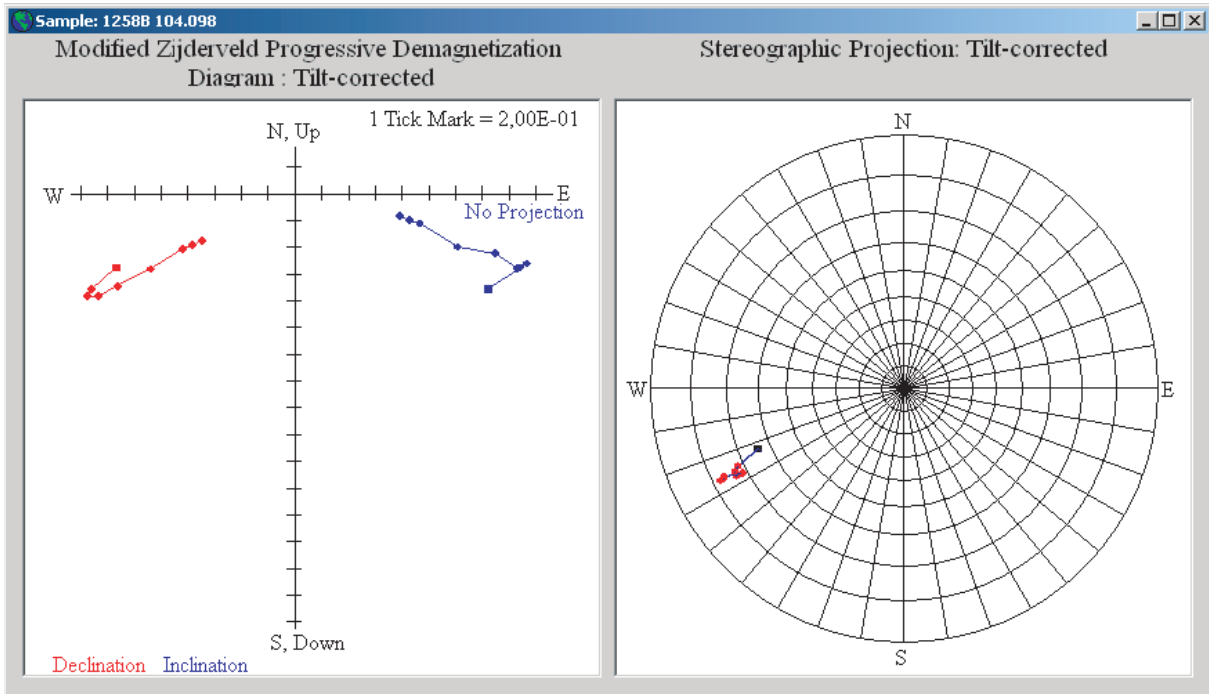


Figure F8. A. Gamma ray attenuation (GRA) density data for a portion of Holes 1259A (black), 1259B (blue), and 1259C (green) plotted vs. mbsf depth. B. GRA density data for a portion of Holes 1259A (black), 1259B (blue), and 1259C (green) plotted vs. mcd depth. C. Splice record of GRA density from 525 to 550 mcd at Site 1259, showing cores from Holes 1259A (black) and 1259B (blue) that were patched together.

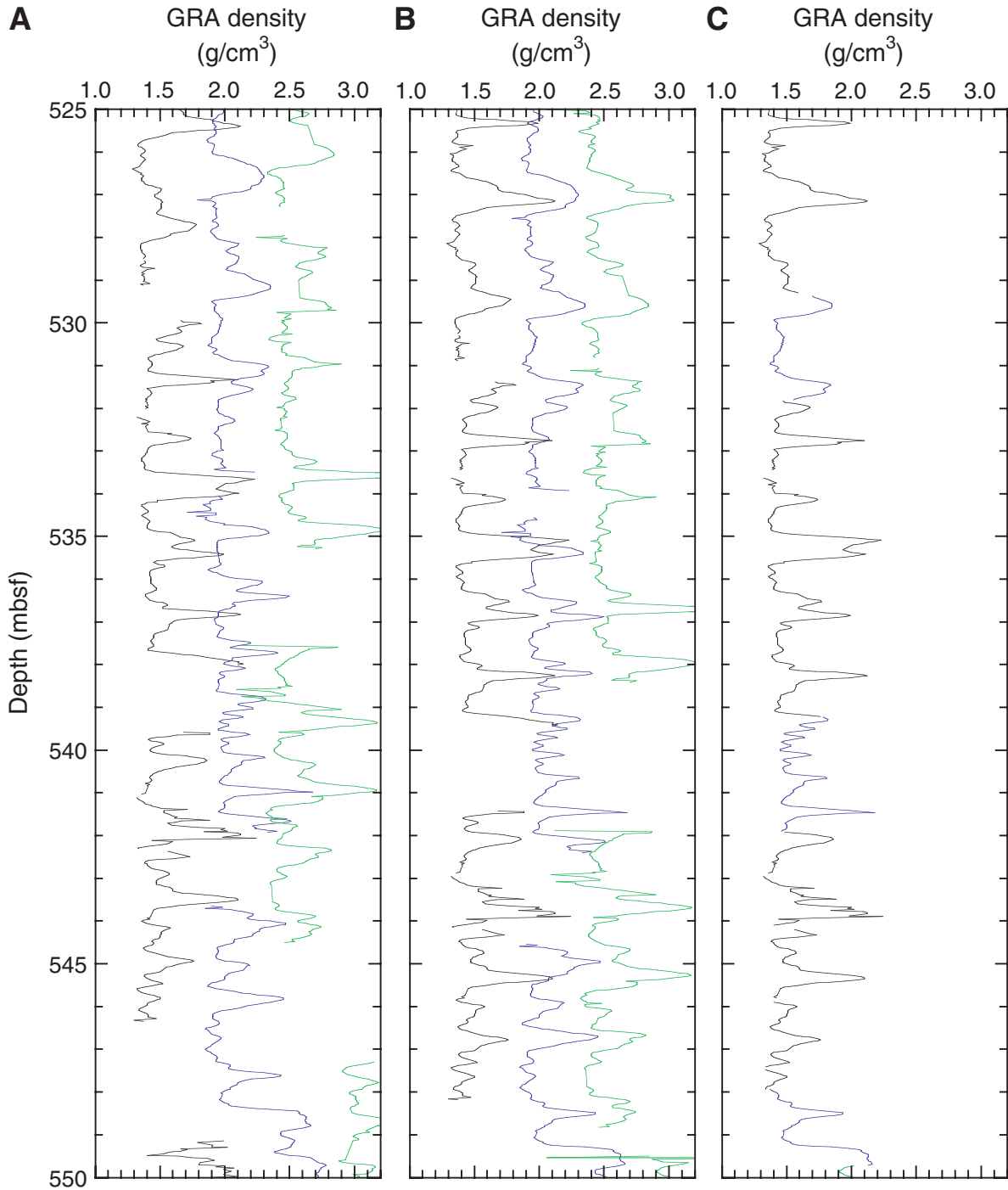


Figure F9. Example of Leg 207 age-depth plot. E/O = Eocene/Oligocene boundary, K/T = Cretaceous/Tertiary boundary.

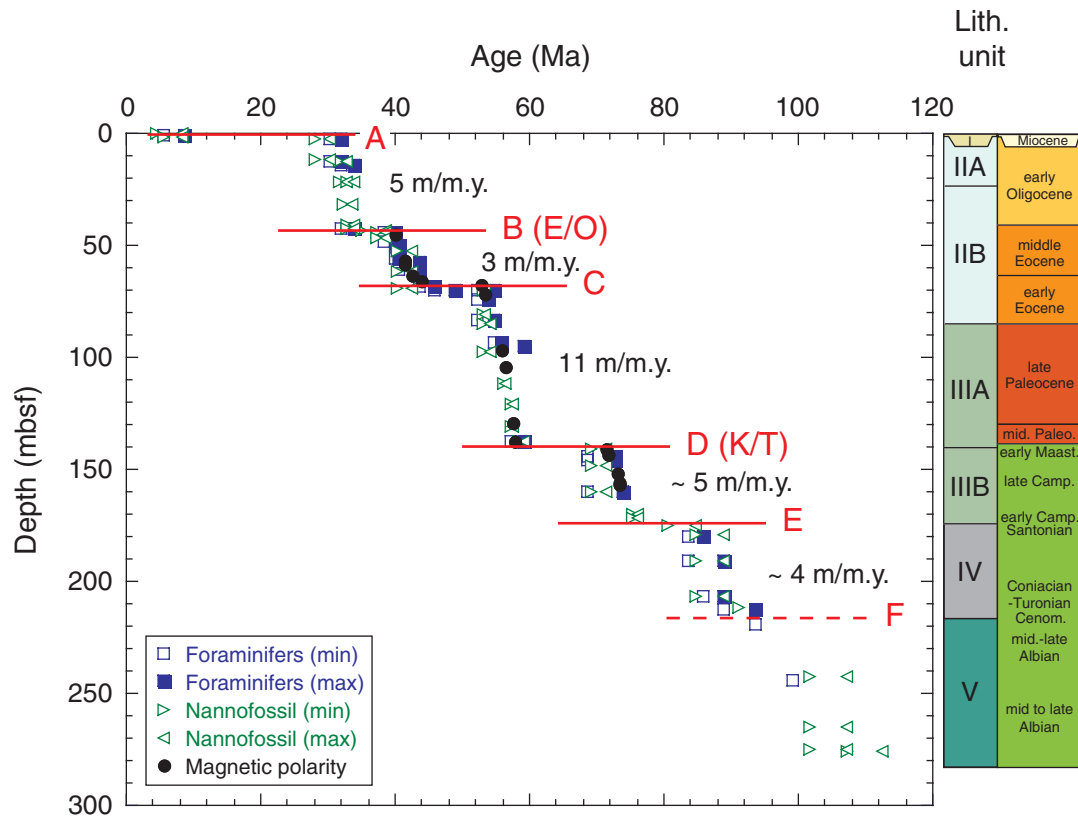


Figure F10. Comparison of Si results obtained by (A) inductively coupled plasma–atomic emission spectroscopy (ICP-AES) vs. colorimetry and (B) two different emission lines by ICP-AES (see “[Determination of Total Dissolved Sulfur and Total Dissolved Silica by ICP-AES](#),” p. 32, in “[Inorganic Geochemistry](#)”).

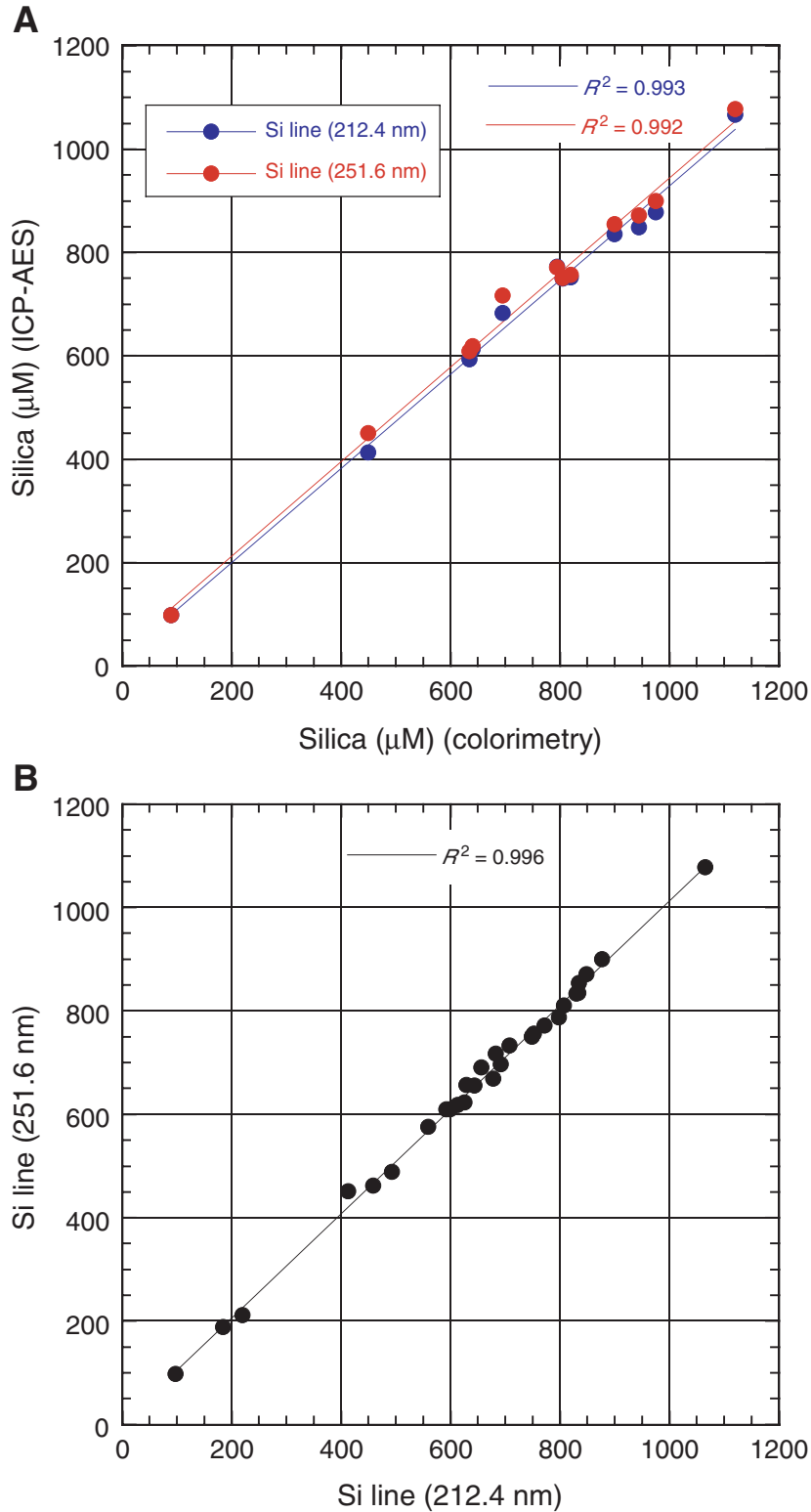


Figure F11. Schematic illustration of the configurations of tool strings used during Leg 207 (see Table T14, p. 93, for explanations of the acronyms).

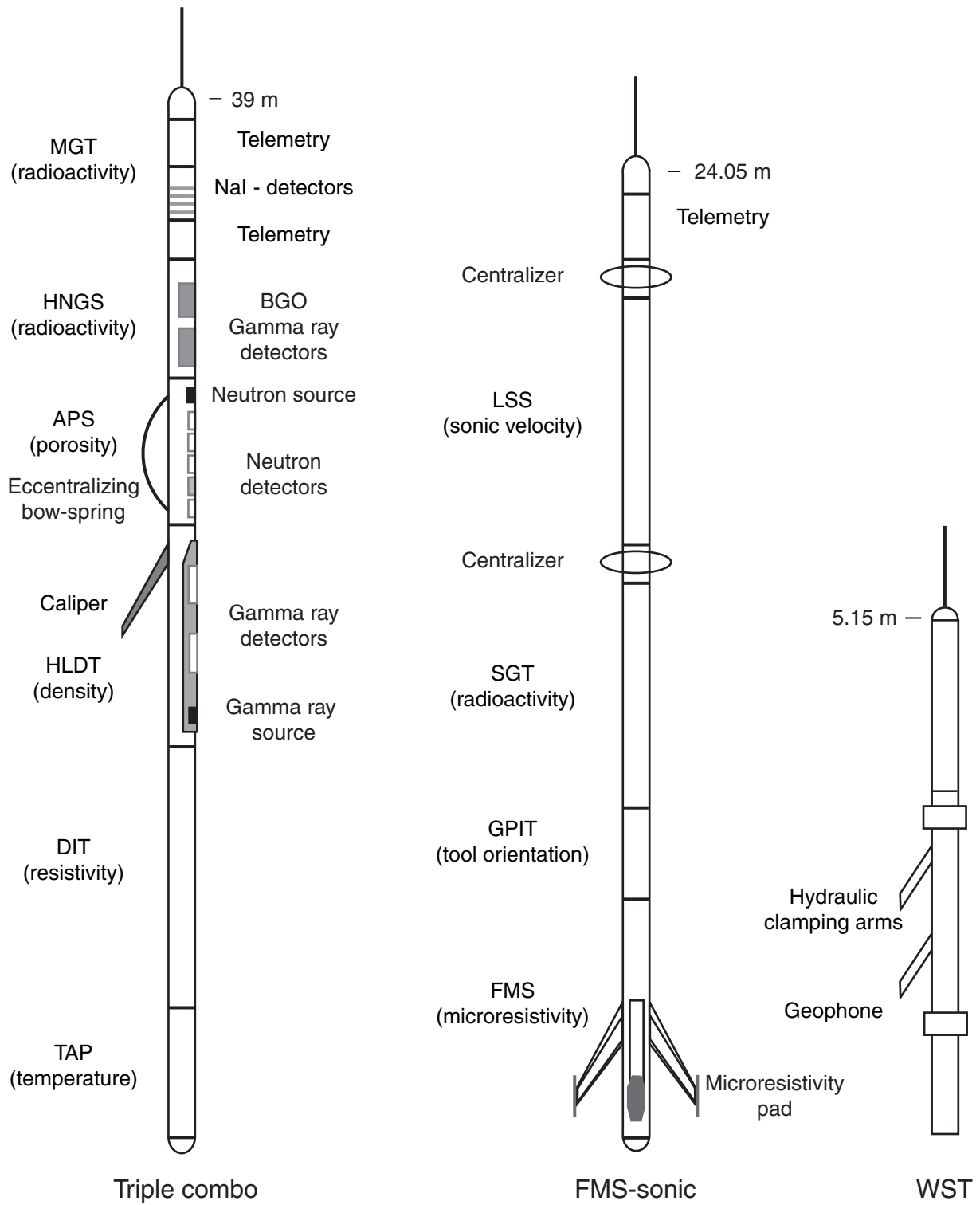


Table T1. Calcareous nannofossil datum events for the Cenozoic. (See table notes. Continued on next page.)

Species event	Zone/subzone (base)	Age (Ma)	Reference	Age (Ma)	Reference
B <i>Emiliania huxleyi</i>	CN15/NN21	0.26	1		
T <i>Pseudoemiliania lacunosa</i>	CN14b/NN20	0.46	1		
B <i>Gephyrocapsa parallela</i> (reentrance medium G)		0.95	2		
B medium <i>Gephyrocapsa</i>	CN13b	1.69	2		
Pliocene/Pleistocene boundary		1.81	3		
T <i>Discoaster brouweri</i>	CN13a/NN19	1.95	2		
T <i>Discoaster pentaradiatus</i>	CN12d/NN18	2.52	4		
T <i>Discoaster surculus</i>	CN12c/NN17	2.63	4		
T <i>Discoaster tamalis</i>	CN12b+c	2.83	4		
T <i>Sphenolithus</i> spp.	CN12aB*	3.66	5		
T <i>Reticulofenestra pseudumbilica</i>	CN12aA*/NN16	3.80	5		
T <i>Amaurolithus</i> spp.	CN11	4.56	5		
T <i>Ceratolithus acutus</i>	CN10c/NN13	5.05	6		
B <i>Ceratolithus rugosus</i>	CN10c/NN13	5.10	6		
T <i>Triquetrorhabdulus rugosus</i>		5.23	6		
Miocene/Pliocene boundary		5.32	7		
B <i>Ceratolithus acutus</i>	CN10b	5.37	6		
T <i>Discoaster quinqueramus</i>	CN10a/NN12	5.54	6		
T <i>Nicklithus amplificus</i>	CN9bC*	6.00	6		
B <i>Nicklithus amplificus</i>	CN9bB*	6.84	6		
B <i>Amaurolithus primus</i>	CN9bA*	7.39	6		
B <i>Discoaster berggrenii</i>	CN9a/NN11	8.28	6		
B <i>Discoaster loeblichii</i>	CN8b	8.43	5		
T <i>Discoaster hamatus</i>	CN8a/NN10	9.63	6		
T <i>Catinaster calyculus</i>		9.64	6		
T <i>Catinaster coalitus</i>		9.69	6		
B <i>Discoaster neohamatus</i>		10.45	6		
B <i>Discoaster hamatus</i>	CN7a/NN9	10.48	6		
B <i>Catinaster coalitus</i>	CN6/NN8	10.79	6		
TC <i>Discoaster kugleri</i>		11.60	6		
BC <i>Discoaster kugleri</i>	CN5b/NN7	11.88	6		
B <i>Triquetrorhabdulus rugosus</i>		12.81	5		
T <i>Cyclicargolithus floridanus</i>		13.19	5		
T <i>Sphenolithus heteromorphus</i>	CN5a/NN6	13.55	8		
T <i>Helicosphaera ampliaptera</i>	CN4/NN5	15.8	9	15.10	8
T Acme <i>Discoaster deflandrei</i>		16.2	5	16.07	8
B <i>Discoaster signus</i>		16.2	5		
B <i>Sphenolithus heteromorphus</i>	CN3	18.1	9	17.70	8
T <i>Sphenolithus belemnus</i>	CN3/NN4	18.4	9	17.94	8
T <i>Triquetrorhabdulus carinatus</i>	NN3	19.6	†		
B <i>Sphenolithus belemnus</i>	CN2	19.7	9	18.90	8
X <i>Helicosphaera euphratis</i> / <i>Helicosphaera carteri</i>				20.80	8
T Acme <i>Triquetrorhabdulus carinatus</i>		22.9	†		
B <i>Discoaster druggii</i>	CN1c/NN2	23.2	11		
B <i>Sphenolithus disbelemnus</i>		23.5	8	22.67	8
Oligocene/Miocene boundary		23.8	11	22.90	8
T <i>Sphenolithus delphix</i>		23.7	8	22.98	8
B <i>Sphenolithus delphix</i>		24.4	8	23.24	8
T <i>Sphenolithus ciperoensis</i>	CN1a	24.7	8	24.14	8
T Acme <i>Cyclicargolithus abisectus</i>	CN1b	25.5	†		
T <i>Sphenolithus distentus</i>	CP19b/NP25	26.5	10		
B <i>Sphenolithus ciperoensis</i>	CP19a/NP24	28.1	10		
T <i>Discoaster pseudoradians</i>		29.1	11		
B <i>Sphenolithus distentus</i>	CP18	30.4	10		
T <i>Reticulofenestra umbilica</i> ($\geq 14 \mu\text{m}$)	CP17/NP23	31.7	12		
T Acme <i>Ericsonia obruta</i>	CP16b	32.2	12		
T <i>Isthmolithus recurvus</i>		32.7	12		
T <i>Ericsonia formosa</i>	CP16c/NP22	32.9	12		
B Acme <i>Ericsonia obruta</i>		33.7	12		
Eocene/Oligocene boundary		33.7	11		
T <i>Discoaster saipanensis</i>	CP16a/NP21	34.0	12		
T <i>Discoaster barbadiensis</i>	CP16a	34.2	12		
T <i>Criboecium reticulatum</i>		34.9	12		
T <i>Calcidiscus protoannulus</i>		35.4	12		
B <i>Isthmolithus recurvus</i>	NP19	36.6	12		
B <i>Chiasmolithus oamaruensis</i>	NP18	37.0	11		

Table T1 (continued).

Species event	Zone/subzone (base)	Age (Ma)	Reference	Age (Ma)	Reference
T <i>Chiasmolithus grandis</i>	CP15	37.1	12		
B <i>Dictyococcites bisectus</i>		38.5	13		
B <i>Dictyococcites hesslandii</i>		40.3	12		
T <i>Chiasmolithus solitus</i>	CP14b/NP17	40.4	11		
T <i>Nannotetrina</i> spp.		42.3	12		
B <i>Reticulofenestra umbilica</i> ($\geq 14 \mu\text{m}$)	CP14a	42.5	12		
T <i>Blackites gladius</i>	NP16	43.4	11		
T <i>Nannotetrina fulgens</i>		43.4	14		
T <i>Chiasmolithus gigas</i>	CP13c	44.0	14		
B <i>Chiasmolithus gigas</i>	CP13b	46.1	11		
B <i>Nannotetrina fulgens</i>	CP13a/NP15	47.0	14		
T <i>Discoaster sublodoensis</i>		47.2	14		
B <i>Nannotetrina</i> spp.		47.8	14		
T <i>Discoaster lodoensis</i>		48.0	14		
B <i>Rhabdosphaera inflata</i>	CP12b	48.5	11		
B <i>Discoaster sublodoensis</i>	CP12a/NP14	49.3	14		
T <i>Tribrachiatus orthostylus</i>	NP13	51.0	14		
B <i>Toweius crassus</i>	CP11	51.5	11		
B <i>Discoaster lodoensis</i>	CP10/NP12	52.4	14		
T <i>Discoaster multiradiatus</i>		53.0	14		
B <i>Sphenolithus radians</i>		53.3	14		
X <i>Tibrachiatus contortus/Tibrachiatus orthostylus</i>	CP9b/NP11	53.4	14	53.40	‡
X <i>Tibrachiatus bramlettei/Tibrachiatus contortus</i>		53.7	14	53.88	‡
B <i>Discoaster diastypus</i>	CP9a	53.9	14		
B <i>Tibrachiatus bramlettei</i>	CP9a/NP10	53.9	14	54.36	‡
B <i>Rhombaster cuspis</i>		54.1	14		
T <i>Fasciculithus</i> spp.		54.1	14		
Paleocene/Eocene boundary		55.0	**		
B <i>Campylosphaera eodela</i>	CP8b	55.5	11		
B <i>Discoaster multiradiatus</i>	CP8a/NP9	56.2	14		
B <i>Discoaster okadae</i>		56.4	14		
B <i>Discoaster nobilis</i>	CP7	56.5	14		
B <i>Heliolithus riedelii</i>	NP8	57.3	11		
B <i>Discoaster mohleri</i>	CP6/NP7	57.5	14		
B <i>Heliolithus kleinpellii</i>	CP5/NP6	58.2	14		
B <i>Sphenolithus anarrhopus</i>		58.4	11		
B <i>Heliolithus cantabriae</i>		58.8	14		
B <i>Fasciculithus pileatus</i>		59.3	14		
B <i>Fasciculithus tympaniformis</i>	CP4/NP5	59.7	11		
B <i>Fasciculithus</i> spp.		60.0	14		
B <i>Sphenolithus</i> spp.		60.7	14		

Notes: B = base, T = top, TC = top common, BC = base common, X = abundance crossover. * = further subdivision of Subzones (CN12aB, etc.) according to Bukry (1991) and Raffi and Flores (1995). † = age estimate derived through calibration to magnetostratigraphy at Site 1218. ‡ = age estimate derived through counting of precessional cycles at Site 1215. ** = carbon isotope excursion calibrated by astronomical tuning at Site 1051 (Norris and Röhl, 1999). Bold = astrochronologically tuned datums. References: 1 = Thierstein et al. (1977), 2 = Raffi et al. (1993), 3 = Lourens et al. (1996), 4 = Tiedemann et al. (1994), 5 = Raffi and Flores (1995), 6 = Backman and Raffi (1997), 7 = Van Couvering et al. (2000), 8 = Shackleton et al. (1999), 9 = Backman et al. (1990), 10 = Olafsson and Villa (1992), 11 = Berggren et al. (1995b), 12 = Backman (1987), 13 = Monechi and Thierstein (1985), 14 = Backman (1986).

Table T2. Calcareous nannofossil datum events for the Cretaceous.

Species event	Zone/subzone (base)	Age (Ma)	Reference
Maastrichtian			
LO Cretaceous taxa (<i>Micula prinsii</i>)		65.0	1
FO <i>Micula prinsii</i>		65.4	2
FO <i>Nephrolithus frequens</i>	CC26	65.8	2, 3
FO <i>Micula murus</i>		66.2	2
FO <i>Lithraphidites quadratus</i>	UC20	67.5	2, 4
LO <i>Reinhardtites levis</i>	CC25/UC19	69.2	2, 3, 4
LO <i>Tranolithus orionatus</i>	CC24/UC18	69.6	2, 3, 4
Campanian			
LO <i>Uniplanarius trifidum</i>		71.3	2
LO <i>Aspidolithus parvus</i>	UC17	74.6	2, 4
LO <i>Eiffellithus eximius</i>	CC23/UC16	75.3	2, 3, 4
FO <i>Uniplanarius trifidum</i>	CC22	76.0	2, 3
FO <i>Uniplanarius sissinghii</i>	CC21	77.0	2, 3
FO <i>Ceratolithoides aculeus</i>	CC20	78.5	2, 3
FO <i>Misceomarginatus pleniporus</i>	UC15	79.5	2, 4
LO <i>Marthasterites furcatus</i>	CC19	80.6	2, 3
FO <i>Ceratolithoides verbeekii</i>		82.0	2
FO <i>Aspidolithus parvus constrictus</i>		82.5	2
FO <i>Aspidolithus parvus</i>	CC18/UC14	83.4	2, 3, 4
FO <i>Arkhangelskiella cymbiformis</i>	UC13	83.5	2, 4
Santonian			
FO <i>Calculites obscurus</i>	CC17	84.0	2, 3
LO <i>Lithastrinus septenarius</i>	UC12	84.7	2, 4
FO <i>Lucianorhabdus cayeuxii</i>	CC16	84.8	2, 3
FO <i>Reinhardtites anthophorus</i>	CC15/UC11	85.5	2, 3, 4
Coniacian			
FO <i>Micula decussata</i>	CC14/UC10	87.2	2, 3, 4
FO <i>Lithastrinus septenarius</i>	UC9	88.8	2, 4
Turonian			
FO <i>Marthasterites furcatus</i>	CC13	89.3	2, 3
FO <i>Eiffellithus eximius</i>	CC12/UC8	91.0	2, 3, 4
FO <i>Quadrum gartneri</i>	CC11/UC7	93.2	2, 3, 4
LO <i>Helenea chiastia</i>	UC6	93.4	2, 4
Cenomanian			
LO <i>Lithraphidites acutus</i>	UC5	94.0	2, 4
FO <i>Cylindralithus biarcus</i>	UC4	94.1	2, 4
FO <i>Lithraphidites acutus</i>	CC10/UC3	96.8	2, 3, 4
FO <i>Gartnerago segmentatum</i>	UC2	97.0	2, 3, 4
FO <i>Corollithion kennedyi</i>	NC10b/UC1	97.6	4, 5, 6
Albian			
FO <i>Eiffellithus turriseiffelii</i>	NC10a	101.7	5, 6
FO <i>Eiffellithus monechiae</i>	NC9b	105.0	5, 6
FO <i>Axopodorhabus albianus</i>	NC9a	106.1	5, 6
FO <i>Tranolithus orionatus</i>	NC8c	107.3	5, 6
FO <i>Hayesites albiensis</i>	NC8b	110.9	5, 6
Aptian			
FO <i>Prediscosphaera columnata</i>	NC8a	112.6	5, 6
FO <i>Rhagodiscus achylostaurion</i>	NC7c	115.2	5, 6
LO <i>Micrantholithus hoschulzii</i>	NC7b	117.3	5, 6
FO <i>Eprolithus floralis</i>	NC7a	119.0	5, 6
LO <i>Conusphaera rothii</i>	NC6b	119.5	5, 6
FO <i>Hayesites irregularis</i>	NC6a	121.1	5, 6
LO <i>Flabellites oblongus</i>		121.1	2, 5

Notes: LO = last occurrence, FO = first occurrence. References: 1 = Berggren et al. (1995b), 2 = Erba et al. (1995), 3 = Sissingh (1977), 4 = Burnett (1999), 5 = Roth (1978), 6 = Bralower et al. (1997).

Table T3. Planktonic foraminifer datum events for the Cenozoic.
(See table notes. Continued on next two pages.)

Species event	Zone/subzone (base)	Age (Ma)	Reference
LO <i>Truncorotalia tosaensis</i>	PT1b	0.7	1
Pliocene/Pleistocene boundary		1.8	8
LO <i>Globigerinoides fistulosus</i>	PT1a	1.9	3
FO <i>Truncorotalia truncatulinoides</i>	N22	1.9	3
LO <i>Globorotalia pseudomiocenica</i> (Indo-Pacific only)	PL6	2.3	2
LO <i>Globoturborotalia woodi</i>		2.3	3
LO <i>Dentoglobigerina altispira</i>	PL5	3.1	3
LO <i>Sphaeroidinellopsis seminulina</i>	PL4	3.1	3
FO <i>Globigerinelloides fistulosus</i>		3.3	1
FO <i>Truncorotalia tosaensis</i>	N21	3.4	1
LO <i>Pulleniatina primalis</i>		3.7	1
LO <i>Globorotalia margaritae</i>	PL3	3.9	3
FO <i>Globorotalia crassaformis</i>		4.3	3
LO <i>Pulleniatina spectabilis</i>		4.3	4
LO <i>Globoturborotalita nepenthes</i>	PL2	4.4	3
LO <i>Globorotalia cibaoensis</i>	PL1b	4.6	2
Miocene/Pliocene boundary		5.3	9
FO <i>Sphaeroidinella dehiscens</i> s.l.	N19	5.5	3
FO <i>Globorotalia tumida</i>	N18/PL1a	5.8	3
LO <i>Globorotalia linguaensis</i>	M14	6.0	2
FO <i>Pulleniatina primalis</i>		6.4	2
FO <i>Globorotalia conomiozea</i>		7.1 (6.9)	2
FO <i>Globigerinoides extremus</i>		8.6	3
FO <i>Globorotalia plesiotumida</i>	N17/M13b	8.6	3
FO <i>Neogloboquadrina acostaensis</i>	N16/M13a	9.8	3
LO <i>Paragloborotalia mayeri</i>	N15/M12	10.5	3
FO <i>Globoturborotalita nepenthes</i>	N14/M11	11.2	3
LO <i>Fohsella fohsi</i> s.l. (including <i>fohsi lobata</i> and <i>fohsi robusta</i>)	N13/M10	11.7	3
FO <i>Globorotalia linguaensis</i>		12.9	3
FO <i>Fohsella fohsi robusta</i>		13.2	3
FO <i>Fohsella fohsi</i> s.l.	N12/M8	13.4	3
FO <i>Fohsella praefohsi</i>	N11	14.0	5
FO <i>Fohsella peripheroacuta</i>	N10/M7	14.7	5
FO <i>Orbulina</i> spp.	N9/M6	15.1	5
FO <i>Praeorbulina glomerosa</i>	M5b	16.1	5
FO <i>Praeorbulina sicana</i>	N8/M5a	16.4	5
FO <i>Globorotalia miozea</i>		16.7	2
LO <i>Catapsydrax dissimilis</i>	N7/M4a	17.3	5
FO <i>Globorotalia praescitula</i>		18.5	2
FO <i>Globigerinatella insueta</i>	N6/M3	18.8	2
LO <i>Globoquadrina binaiensis</i>		19.1	5
FO <i>Globigerinoides altiapertura</i>		20.5	2
LO <i>Tenuitella munda</i>		21.5	2
LO <i>Paragloborotalia kugleri</i>	N5/M2	21.5	2
FO <i>Globorotalia incognita</i>		21.6	2
LO <i>Paragloborotalia pseudokugleri</i>		21.6	2
LO " <i>Globigerina</i> " <i>angulisuturalis</i>		21.6	2
LO <i>Globoquadrina globularis</i>		22.8	2
FO <i>Globoquadrina dehiscens</i>	M1b	23.2	2
FO <i>Globigerinoides trilobus</i> s.l.		23.4	5
Oligocene/Miocene boundary		23.8	2
FO <i>Paragloborotalia kugleri</i>	N4/M1a	23.8	2
LO <i>Globigerina euapertura</i>		23.8	2
LO <i>Tenuitella gemma</i>		24.3	2
FO <i>Globigerinoides primordius</i> (common)		24.3	2
FO <i>Paragloborotalia pseudokugleri</i>		25.9	2
FO <i>Globigerinoides primordius</i>		26.7	2
LO <i>Globigerina labiacrassata</i>		27.1	2
LO <i>Paragloborotalia opima</i>	P22	27.1	2
LO <i>Ch. cubensis</i> (common)	P21b	28.5	2
FO " <i>Globigerina</i> " <i>angulisuturalis</i>	P21a	29.4	2
LO <i>Subbotina angiporoides</i>		30.0	2
LO " <i>Globigerina</i> " <i>ampliapertura</i>	P20	30.3	2
FO <i>Paragloborotalia opima</i>		30.6	2
LO <i>Pseudohastigerina</i> spp.	P19	32.0	2
FO <i>Cassigerinella chipolensis</i>		33.7	2

Table T3 (continued).

Species event	Zone/subzone (base)	Age (Ma)	Reference
Eocene/Oligocene boundary		33.7	2
LO <i>Hantkenina</i> spp.		33.7	2
LO <i>Turborotalia cerroazulensis</i>	P18	33.8	2
LO <i>Cribohantkenina inflata</i>	P17	34.0	2
LO <i>Globigerinatheka index</i>		34.3	2
FO <i>Turborotalia cunialensis</i>	P16	35.2	2
LO <i>Turborotalia pomeroli</i>		35.3	2
LO <i>Globigerinatheka semiinvoluta</i>		35.3	2
FO <i>Cribohantkenina inflata</i>		35.5	2
LO <i>Acarinina collactea</i>		37.7	2
LO <i>Subbotina linaperta</i>		37.7	2
LO <i>Morozovella spinulosa</i>		38.1	2
FO <i>Globigerinatheka semiinvoluta</i>	P15	38.4	2
LO <i>Planorotalites</i>		38.5	2
LO <i>Acarinina primitiva</i>		39.0	2
LO <i>Subbotina frontosa</i>		39.3	2
LO <i>Globigerinatheka beckmanni</i>	P14	40.1	2
FO <i>Globigerinatheka beckmanni</i>	P13	40.5	2
LO <i>Acarinina bullbrooki</i>		40.5	2
FO <i>Turborotalia pomeroli</i>		42.4	2
FO <i>Globigerinatheka index</i>		42.9	2
FO <i>Morozovella lehneri</i>		43.5	2
LO <i>Morozovella aragonensis</i>	P12	43.6	2
FO <i>Globigerinatheka kugleri</i>	P11	45.8	2
FO <i>Turborotalia possagnoensis</i>		46.0	2
FO <i>Hantkenina nuttalli</i>	P10	49.0	2
FO <i>Planorotalites palmerae</i>	P9	50.4	2
LO <i>Morozovella formosa</i>	P8	50.8	2
FO <i>Acarinina pentacamerata</i>		50.8	2
FO <i>Morozovella aragonensis</i>	P7	52.3	2
LO <i>Morozovella marginodentata</i>		52.5	2
LO <i>Morozovella lensiformis</i>		52.7	2
LO <i>Subbotina velascoensis</i>		53.5	2
LO <i>Morozovella aequa</i>		53.6	2
FO <i>Morozovella formosa</i>	P6b	54.0	2
FO <i>Morozovella lensiformis</i>		54.0	2
LO <i>Morozovella velascoensis</i>	P6a	54.7	2
LO <i>Morozovella acuta</i>		54.7	2
FO <i>Morozovella gracilis</i>		54.7	2
FO <i>Igorina broedermanni</i>		54.7	2
FO <i>Morozovella marginodentata</i>		54.8	2
Paleocene/Eocene boundary		55.0	7
FO <i>Globanomalina australiformis</i>		55.5	2
FO <i>Morozovella subbotinae</i>		55.9	2
LO <i>Globanomalina pseudomenardii</i>	P5	55.9	2
LO <i>Acarinina nitida</i> (<i>Acarinina acarinata</i>)		56.3	2
LO <i>Acarinina mckannai</i>		56.3	2
FO <i>Acarinina soldadoensis</i>	P4c	56.5	2
FO <i>Acarinina coalingensis</i> (<i>triplex</i>)		56.5	2
FO <i>Morozovella aequa</i>		56.5	2
LO <i>Acarinina subsphaerica</i>	P4b	57.1	2
FO <i>Acarinina mckannai</i>		59.1	2
FO <i>Acarinina subsphaerica</i>		59.2	2
FO <i>Acarinina nitida</i>		59.2	2
FO <i>Globanomalina pseudomenardii</i>	P4a	59.2	2
LO <i>Parasubbotina variospira</i> (<i>variata</i> ?)		59.2	2
LO <i>Parasubbotina variata</i>		59.2	2, 6
FO <i>Morozovella velascoensis</i>		60.0	2
FO <i>Igorina albeari</i>	P3b	60.0	2
FO <i>Acarinina strabocella</i>		60.5	6
FO <i>Morozovella conicotruncata</i>		60.9	2
FO <i>Morozovella angulata</i>	P3a	61.0	2
FO <i>Igorina pusilla</i>		61.0	2
FO <i>Praemurica praeangulata</i>		61.2	2
FO <i>Praemurica uncinata</i>	P2	61.2	2
FO <i>Globanomalina imitata</i>		61.3	2
FO <i>Globanomalina compressa</i>	P1c	63.0	2
FO <i>Praemurica inconstans</i>		63.0	2
FO <i>Parasubbotina variata</i>		63.0	2

Table T3 (continued).

Species event	Zone/subzone (base)	Age (Ma)	Reference
FO <i>Subbotina triloculinoides</i>	P1b	64.5	2
LO <i>Parvularugoglobigerina extensa</i>		64.9	6
LO <i>Parvularugoglobigerina eugubina</i>	P1a	64.9	2
FO <i>Parvularugoglobigerina eugubina</i>	Pa	65.0	2

Notes: LO = last occurrence, FO = first occurrence. References: 1 = Berggren et al. (1995b), 2 = Berggren et al. (1995a), 3 = Chaisson and Pearson (1997), 4 = Shackleton et al. (1995), 5 = Pearson and Chaisson (1997), 6 = Olsson et al. (1999), 7 = Norris and Röhl (1999), 8 = Lourens et al. (1996), 9 = Hilgen (1991b).

Table T4. Planktonic foraminifer datum events for the Cretaceous.

Species event	Zone/subzone (base)	Age (Ma)	Reference
Maastrichtian			
LO <i>Abathomphalus mayaroensis</i>		65.0	1
FO <i>Abathomphalus mayaroensis</i>	<i>Abathomphalus mayaroensis</i> (KS31)	68.6	2, 3
FO <i>Racemiguembelina fructicosa</i>	<i>Racemiguembelina fructicosa</i> – <i>Contusotruncana contusa</i>	69.6	3
FO <i>Contusotruncana contusa</i>	<i>Racemiguembelina fructicosa</i> – <i>Contusotruncana contusa</i>	69.6	3
Campanian			
FO <i>Gansserina gansseri</i>	<i>Gansserina gansseri</i> (KS30)	72.8	2, 4, 5
FO <i>Globotruncana aegyptiaca</i>	<i>Globotruncana aegyptiaca</i> (KS29)	73.8	2, 4, 5
LO <i>Radotruncana calcarata</i>	<i>Globotruncana havanensis</i> (KS28)	75.2	2, 4, 5
FO <i>Radotruncana calcarata</i>	<i>Radotruncana calcarata</i> (KS27)	75.7	2, 4, 5
FO <i>Globotruncana ventricosa</i>	<i>Globotruncana ventricosa</i> (KS26)	79.5	2, 4, 5
LO <i>Dicarinella asymetrica</i>	<i>Globotruncana elevata</i> (KS25)	83.0	2, 4, 5
Santonian			
FO <i>Globotruncana elevata</i>		84.8	5
FO <i>Dicarinella asymetrica</i>	<i>Dicarinella asymetrica</i> (KS24)	85.4	2, 4, 5
FO large heterohelicids		85.8	3
Coniacian			
FO <i>Contusotruncana fornicata</i>		88.0	3
Turonian			
FO <i>Dicarinella concavata</i>	<i>Dicarinella concavata</i> (KS23)	89.5	2, 4, 5
LO <i>Helvetoglobotruncana helvetica</i>	<i>Marginotruncana sigali</i> (KS22)	90.7	2, 4, 6
FO <i>Marginotruncana</i> spp. (<i>Marginotruncana renzi</i>)		92.5	3
FO <i>Helvetoglobotruncana helvetica</i>	<i>Helvetoglobotruncana helvetica</i> (KS21)	93.0	2, 4, 6
Cenomanian			
LO <i>Rotalipora cushmani</i>	<i>Whiteinella archaeocretacea</i> (KS20)	94.0	2, 4, 6
FO <i>Dicarinella algeriana</i>		95.4	3
FO <i>Whiteinella</i> spp. (<i>Whiteinella baltica</i>)		95.4	3
FO <i>Rotalipora cushmani</i>	<i>Rotalipora cushmani</i> (KS19)	96.6	2, 4, 6
FO <i>Rotalipora reicheli</i>	<i>Rotalipora reicheli</i> (KS18)	96.8	2, 4, 6
Albian			
FO <i>Rotalipora globotruncanoides</i>	<i>Rotalipora globotruncanoides</i> (KS17)	99.1	2, 4, 6
FO <i>Planomalina buxtorfi</i>		100.2	7
FO <i>Rotalipora appenninica</i>	<i>Rotalipora appenninica</i> (KS16)	100.4	2, 4, 6
FO <i>Rotalipora ticinensis</i>	<i>Rotalipora ticinensis</i> (KS15)	101.7	2, 4, 6
FO <i>Heterohelix</i> spp. (<i>Heterohelix moremani</i>)		102.0	3, 7
FO <i>Rotalipora subticinensis</i>		102.4	2, 4, 6
FO <i>Biticinella breggiensis</i>	<i>Biticinella breggiensis</i> (KS14)	105.0	2, 4, 6
FO <i>Ticinella primula</i>	<i>Ticinella primula</i> (KS13)	109.5	2, 4, 6
Aptian			
LO <i>Ticinella bejaouaensis</i>	<i>Heterohelix planispira</i> (KS12)	112.4	2, 4, 6, 7
LO <i>Planomalina cheniourensis</i>		112.6	2, 4, 6, 7
FO <i>Ticinella bejaouaensis</i>	<i>Ticinella bejaouaensis</i> (KS11)	114.3	2, 4, 6, 7
LO <i>Globigerinelloides algerianus</i>	<i>Heterohelix trocoidea</i> (KS10)	115.2	2, 4, 6
FO <i>Globigerinelloides algerianus</i>	<i>Globigerinelloides algerianus</i> (KS9)	117.1	2, 4, 6
LO <i>Leupoldina cabri</i>	<i>Globigerinelloides ferreolensis</i> (KS8)	118.2	2, 4, 6
FO <i>Leupoldina cabri</i>	<i>Leupoldina cabri</i> (KS7)	119.2	2, 4, 6

Notes: LO = last occurrence, FO = first occurrence. References: 1 = Berggren et al. (1995b), 2 = Sliter (1989), 3 = Premoli Silva and Sliter (1999), 4 = Caron (1985), 5 = Erba et al. (1995), 6 = Bralower et al. (1997), 7 = Leckie (1984).

Table T5. Radiolarian datum events for the Cenozoic. (See table notes. Continued on next three pages.)

Epoch/ age (Ma)	Standard tropical zonation	Code number	Event	Age* (Ma)	Reference
Pleistocene	<i>B. invaginata</i>	RN17	FO <i>Buccinosphaera invaginata</i>	0.18	1
	<i>C. tuberosa</i>	RN16	LO <i>Stylatractus universus</i>	0.42	2
	<i>S. universus</i>	RN15	FO <i>Collosphaera tuberosa</i>	0.61	2
	<i>A. ypsilon</i>	RN14	LO <i>Pterocorys campanula</i>	0.80	3
			FO <i>Pterocorys hertwigii</i>	0.75	3
LO <i>Anthocyrtdium angulare</i>			1.12	2	
<i>A. angulare</i>	RN13	FO <i>Lamprocyrtis nigrinia</i>	1.55	3	
		LO <i>Lamprocyrtis heteroporos</i>	1.30	3	
1.77			LO <i>Pterocanium prismatium</i>	1.74	2
late Pliocene	<i>P. prismatium</i>	RN12	FO <i>Anthocyrtdium angulare</i>	1.80	3
			LO <i>Theocorythium vetulum</i>	1.40	3
			LO <i>Anthocyrtdium jenghisi</i>		
			FO <i>Cycladophora davisiana</i>		
			FO <i>Lamprocyrtis heteroporos</i>		
			FO <i>Theocorythium trachelium trachelium</i>	1.60	3
			LO <i>Stichocorys peregrina</i>	2.74	2
			<i>Didymocyrtis avita</i> → <i>D. tetrathalamus</i>		
3.58	<i>L. audax</i>	RN1	LO <i>Phormostichoartus fistula</i>	3.35	3
			LO <i>Lychnodictyum audax</i>	3.60	3
			LO <i>Phormostichoartus doliolum</i>	3.87	2
early Pliocene	<i>P. doliolum</i>	RN10	FO <i>Amphirhoptum ypsilon</i>	4.00	3
			<i>Spongaster pentas</i> → <i>S. tetras tetras</i>	4.10	3
			LO <i>Spongaster berminghami</i>	4.70	3
			LO <i>Didymocyrtis penultima</i>	4.19	2
			<i>Didymocyrtis penultima</i> → <i>D. avita</i>		
5.32	<i>S. peregrina</i>	RN9	FO <i>Pterocanium prismatium</i>	4.90	3
			LO <i>Solenosphaera omnitubus procera</i>	5.30	3
			LO <i>Solenosphaera omnitubus omnitubus</i>	5.30	3
			<i>Spongaster berminghami</i> → <i>S. pentas</i>		
			LO <i>Siphostichartus corona</i>	5.60	3
			FO <i>Pterocorys campanula</i>		
			LO <i>Acrobotrys tritubus</i>	6.00	3
			LO <i>Calocyclella (Calocyclus) caepa</i>	6.20	3
			LO <i>Stichocorys johnsoni</i>	6.60	3
			LO <i>Calocyclella (Calocyclella) cladara</i>		
			<i>Stichocorys delmontensis</i> → <i>S. peregrina</i>	6.71	2
			FO <i>Solenosphaera omnitubus omnitubus</i>	7.30	3
FO <i>Solenosphaera omnitubus procera</i>	7.30	3			
<i>Didymocyrtis antepenultima</i> → <i>D. penultima</i>					
late Miocene	<i>D. penultima</i>	RN8	LO <i>Diartus hughesi</i>	7.70	2
<i>D. antepenultima</i>	RN7	LO <i>Dictyocoryne ontongensis</i>			
		FO <i>Acrobotrys tritubus</i>	7.90	3	
		LO <i>Botryostrobus miralestensis</i>	8.20	3	
		FO <i>Spongaster berminghami</i>	8.30	3	
		<i>Didymocyrtis laticonus</i> → <i>D. antepenultima</i>			
			<i>Diartus petterssoni</i> → <i>D. hughesi</i>	8.77	2
11.19	<i>D. petterssoni</i>	RN6	<i>Lithopera neotera</i> → <i>L. bacca</i>	8.80	3
			LO <i>Stichocorys wolffii</i>	8.80	3
			LO <i>Cyrtocapsella japonica</i>	9.80	3
			LO <i>Lithopera thornburgi</i>		
			LO <i>Cyrtocapsella cornuta</i>	12.10	3
			LO <i>Cyrtocapsella tetrapera</i>	12.10	3
			LO <i>Carpocanopsis cristata</i>	10.60	3
			FO <i>Phormostichoartus doliolum</i>	8.80	3
			LO <i>Dorcadospyris alata</i>	13.60	3
			LO <i>Liriospyris parkerae</i>		
FO <i>Cyrtocapsella japonica</i>					
<i>Calocyclella virginis</i> → <i>C. cladara</i>					
middle Miocene	<i>D. alata</i>	RN5	FO <i>Diartus petterssoni</i>	[11.95]	2
			LO <i>Carpocanopsis bramlettei</i>	14.70	3
			<i>Lithopera renzae</i> → <i>L. neotera</i>	12.10	3
			<i>Didymocyrtis mammifera</i> → <i>D. laticonus</i>		
			FO <i>Lithopera thornburgi</i>		
			FO <i>Phormostichoartus corbula</i>		
			FO <i>Dictyocoryne ontongensis</i>		
			LO <i>Calocyclella costata</i>	15.00	3
			LO <i>Didymocyrtis tubaria</i>		
			LO <i>Didymocyrtis violina</i>		
			FO <i>Lithopera renzae</i>		

Table T5 (continued).

Epoch/ age (Ma)	Standard tropical zonation	Code number	Event	Age* (Ma)	Reference
middle Miocene	<i>D. alata</i>	RN5	LO <i>Dorcadospyris forcipata</i> <i>Dorcadospyris dentata</i> → <i>D. alata</i>]	15.68	2
16.4	<i>C. costata</i>	RN4	LO <i>Eucyrtidium diaphanes</i> <i>Liriospyris stauropora</i> → <i>L. parkerae</i> <i>Carpocanopsis favosa</i> LO <i>Didymocyrtis prismatica</i> LO <i>Carpocanopsis cingulata</i>] FO <i>Carpocanopsis cristata</i>] LO <i>Lychnocanoma elongata</i>] FO <i>Calocycletta costata</i>]	17.03	4
	<i>S. wolfii</i>	RN3	FO <i>Didymocyrtis mammifera</i> FO <i>Calocycletta caepa</i> FO <i>Dorcadospyris dentata</i> FO <i>Liriospyris stauropora</i> LO <i>Dorcadospyris ateuchus</i>] FO <i>Siphostichartus corona</i>] FO <i>Stichocorys wolfii</i>]	17.92	4
early Miocene	<i>S. delmontensis</i>	RN2	FO <i>Didymocyrtis tubaria</i> FO <i>Didymocyrtis violina</i> FO <i>Stichocorys delmontensis</i> FO <i>Carpocanopsis bramlettei</i>] LO <i>Theocyrtis annosa</i>]	20.53	4
	<i>C. tetrapera</i>	RN1	LO <i>Calocycletta serrata</i> LO <i>Calocycletta robusta</i> FO <i>Carpocanopsis favosa</i> FO <i>Cyrtocapsella cornuta</i> FO <i>Calocycletta serrata</i>] FO <i>Calocycletta virginis</i>] FO <i>Botryostrobos miralestensis</i>] FO <i>Cyrtocapsella tetrapera</i>]	23.62	5
23.80			LO <i>Artophormis gracilis</i>	23.94	6
	<i>L. elongata</i>	RP22	FO <i>Eucyrtidium diaphanes</i> LO <i>Dorcadospyris papilio</i> FO <i>Carpocanopsis cingulata</i>] FO <i>Lychnocanoma elongata</i>]	23.94	6
late Oligocene			FO <i>Dorcadospyris forcipata</i>] LO <i>Lychnocanomma trifolium</i>]		
	<i>D. ateuchus</i>	RP21	FO <i>Calocycletta robusta</i> LO <i>Dorcadospyris circulus</i> FO <i>Dorcadospyris papilio</i> LO <i>Lithocyelia angusta</i> <i>Tristylospyris tricerus</i> → <i>D. ateuchus</i>	5	7
28.5			FO <i>Theocyrtis annosa</i>] LO <i>Theocyrtis tuberosa</i>]	~28.80	7
			FO <i>Dorcadospyris circulus</i>		5
			LO <i>Lithocyelia crux</i> FO <i>Lychnocanoma trifolium</i> FO <i>Didymocyrtis prismatica</i> LO <i>Dorcadospyris pseudopapilio</i> <i>Centrobotrys petrushevskayae</i> → <i>C. thermophila</i> FO <i>Lychnodictyum audax</i> <i>Centrobotrys gravida</i> → <i>C. petrushevskayae</i>]		
early Oligocene	<i>T. tuberosa</i>	RP20	FO <i>Dorcadospyris pseudopapilio</i>] FO <i>Lithocyelia crux</i>] <i>Artophormis barbadensis</i> → <i>A. gracilis</i>] FO <i>Centrobotrys gravida</i>] LO <i>Dictyoprora pirus</i>] FO <i>Phormostichoartus fistula</i>] LO <i>Cryptocarpium ornatum</i>] LO <i>Dictyoprora mongolfieri</i>] LO <i>Lychnocanoma amphitrite</i>] <i>Lithocyelia aristotelis</i> → <i>L. angusta</i>]	~32.80	7

Table T5 (continued).

Epoch/ age (Ma)	Standard tropical zonation	Code number	Event	Age* (Ma)	Reference
33.7	<i>C. ornatum</i>	RP19	LO <i>Dictyoprora armadillo</i>	~34.90	7
			LO <i>Lophocyrtis jacchia</i>		
LO <i>Calocyclus turris</i>					
LO <i>Thyrsoyrtis bromia</i>					
LO <i>Thyrsoyrtis rhizonon</i>					
LO <i>Cryptocarpium azyx</i>					
LO <i>Thyrsoyrtis lochites</i>					
LO <i>Calocyclus bandyca</i>					
LO <i>Calocyclus hispida</i>					
LO <i>Lychnocanoma bellum</i>					
LO <i>Podocyrtis papalis</i>					
late Eocene			LO <i>Thyrsoyrtis tetracantha</i>		
	<i>C. bandyca</i>	RP18	LO <i>Thyrsoyrtis triacantha</i>	~36.40	7
			FO <i>Theocyrtis tuberosa</i>		
			LO <i>Eusyringium fistuligerum</i>		
			LO <i>Podocyrtis goetheana</i>		
			FO <i>Calocyclus bandyca</i>		
			LO <i>Podocyrtis chalara</i>		
37.0	<i>C. azyx</i>	RP17	FO <i>Lychnocanoma amphitrite</i>	~37.70	7
			<i>Calocyclus hispida</i> → <i>Calocyclus turris</i>		
			FO <i>Cryptocarpium azyx</i>		
			LO <i>Spongoatractus pachystylus</i>		
			FO <i>Thyrsoyrtis bromia</i>		
			FO <i>Thyrsoyrtis tetracantha</i>		
	<i>P. goetheana</i>	RP16	FO <i>Dictyoprora pirum</i>		
			LO <i>Theocotylissa ficus</i>		
			LO <i>Sethochytris triconiscus</i>		
			FO <i>Dictyoprora armadillo</i>		
			FO <i>Podocyrtis goetheana</i>	~38.80	7
			LO <i>Podocyrtis trachodes</i>		
			LO <i>Phormocyrtis striata striata</i>		
	<i>P. chalara</i>	RP15	FO <i>Tristylopyris triceris</i>	~39.50	7
			Podocyrtis mitra → <i>P. chalara</i>		
			FO <i>Cryptocarpium ornatum</i>		
			LO <i>Podocyrtis ampla</i>		
			LO <i>Eusyringium lagena</i>		
	<i>P. mitra</i>	RP14	FO <i>Artophormis barbadensis</i>	~42.80	7
			FO <i>Thyrsoyrtis lochites</i>		
			FO <i>Sethochytris triconiscus</i>		
			LO <i>Podocyrtis fasciolata</i>		
			LO <i>Podocyrtis helenae</i>		
			Podocyrtis sinuosa → <i>P. mitra</i>		
			FO <i>Podocyrtis trachodes</i>		
			LO <i>Podocyrtis dorus</i>		
			<i>Eusyringium lagena</i> → <i>E. fistuligerum</i>		
	<i>P. ampla</i>	RP13	FO <i>Podocyrtis fasciolata</i>	~44.50	7
			FO <i>Podocyrtis helenae</i>		
			LO <i>Theocotyle venezuelensis</i>		
			Podocyrtis phyxis → <i>P. ampla</i>		
			FO <i>Eusyringium fistuligerum</i>		
			LO <i>Theocotyle nigrinia</i>		
			LO <i>Theocotyle conica</i>		
			<i>Podocyrtis diamesa</i> → <i>P. phyxis</i>		
	<i>T. triacantha</i>	RP12	LO <i>Theocorys anaclasta</i>	~47.50	7
			LO <i>Lamptonium fabaeforme constrictum</i>		
			LO <i>Lamptonium fabaeforme chaunothroax</i>		
			LO <i>Thyrsoyrtis hirsuta</i>		
			LO <i>Thyrsoyrtis robusta</i>		
			<i>Thyrsoyrtis tensa</i> → <i>T. triacantha</i>		
			FO <i>Eusyringium lagena</i>		
			LO <i>Lamptonium fabaeforme fabaeforme</i>		
			FO <i>Podocyrtis dorus</i>		
			<i>Theocotyle cryptocephala</i> → <i>T. conica</i>		
	<i>D. mongolfieri</i>	RP11	LO <i>Calocycloma castum</i>	~48.50	7
			FO <i>Dictyoprora mongolfieri</i>		

Table T5 (continued).

Epoch/ age (Ma)	Standard tropical zonation	Code number	Event	Age* (Ma)	Reference
middle Eocene	<i>T. cryptocephala</i>	RP10	<i>Podocyrtis acalles</i> → <i>P. sinuosa</i>	~49.00	7
			FO <i>Thyrsocyrtis robusta</i> FO <i>Theocotyle venezuelensis</i> LO <i>Buryella clinata</i> FO <i>Theocotyle nigrinia</i> → <i>T. cryptocephala</i>		
49.0					
early Eocene			<i>Spongoatractis bablis</i> → <i>S. pachystylus</i> LO <i>Lamptonium sanfilippoae</i> FO <i>Thyrsocyrtis rhizodon</i> FO <i>Podocyrtis diamesa</i> FO <i>Lamptonium fabaeforme constrictum</i> <i>Phormocyrtis striata exquisita</i> → <i>P. striata striata</i> FO <i>Podocyrtis acalles</i> LO <i>Phormocyrtis cubensis</i> FO <i>Lychnocanoma bellum</i> FO <i>Theocorys anaclasta</i>	~50.30	7
	<i>P. striata striata</i>	RP9			
early Eocene	<i>B. clinata</i>	RP8	LO <i>Pterocodon</i> (?) <i>ampla</i> LO <i>Bekomma bidartensis</i> LO <i>Buryella tetradica</i> LO <i>Thyrsocyrtis tarsipes</i> FO <i>Lithocyclia ocellus</i> gp. FO <i>Thyrsocyrtis tensa</i> <i>Theocotylissa alpha</i> → <i>T. ficus</i> FO <i>Calocyclus hispida</i> FO <i>Spongoatractus balbis</i> FO <i>Lamptonium sanfilippoae</i> FO <i>Theocotyle nigrinia</i> FO <i>Thyrsocyrtis hirsuta</i> <i>Pterocodon</i> (?) <i>antclinata</i> → <i>Buryella clinata</i>	~52.85	7
			FO <i>Theocotylissa alpha</i> FO <i>Lamptonium fabaeforme chaunothorax</i> FO <i>Pterodocon</i> (?) <i>anteclinata</i> FO <i>Lophocyrtis jacchia</i> FO <i>Calocyclus castum</i> <i>Lamptonium pennatum</i> → <i>L. fabaeforme fabaeforme</i> FO <i>Podocyrtis papalis</i> LO <i>Bekomma campechensis</i> FO <i>Bekomma bidartensis</i>	~56.90	7
55.0	<i>B. bidartensis</i>	RP7			
late Paleocene	<i>B. campechensis</i>	RP6	FO <i>Phormocyrtis cubensis</i> LO <i>Buryella pentadica</i> FO <i>Pterocodon</i> (?) <i>ampla</i> FO <i>Bekomma campechensis</i>	~60.20	8
		RP5	FO <i>Buryella tetradica</i>	~60.90	9
61.0		RP4	FO <i>Buryella foremanae</i>	~62.80	9
early Paleocene		RP3	FO <i>Stichomitra granulata</i>	~63.90	9
		RP2	FO <i>Amphisphaera kina</i>	~64.60	9
		RP1	FO <i>Amphisphaera aotea</i>	~65.10	9

Notes: FO = first morphotypic occurrence, LO = last morphotypic occurrence. → = an evolutionary transition. * = Cande and Kent (1995). The age for the morphotypic first occurrence of *Diartus petterssoni* (base RN7) is a demonstrably diachronous event (Johnson and Nigrini, 1985). Brackets = approximately synchronous events. Bold = taxa that define the base of radiolarian zones. The assigned numerical ages should be used with caution because they are approximations only. For the Paleogene record, a combination of data from Sanfilippo and Nigrini (1995, 1996) and an integrated compilation chart (unpublished) based on published data from DSDP/ODP Legs 1–135 have been used to approximate the ages of zonal boundaries. References: 1 = Johnson et al. (1989), 2 = Shackleton et al. (1995), 3 = Lazarus et al. (1995), 4 = Sanfilippo and Nigrini (1996), 5 = Sanfilippo and Nigrini (1995), 6 = Sanfilippo and Nigrini (1995) (an integrated compilation based on published DSDP/ODP Legs 1–135), 7 = Nishimura (1992), 8 = Hollis (1993), 9 = Nigrini and Sanfilippo (2001).

Table T6. Late Cretaceous radiolarian datums and zones.

Species event	Marker species	Age (Ma)	Reference
Campanian			
FO <i>Amphipyndax tylotus</i>	<i>Amphipyndax tylotus</i>	75.0–77.0	1
FO <i>Amphipyndax pseudoconulus</i>	<i>Amphipyndax pseudoconulus</i>	~83.5	1
Coniacian			
FO <i>Theocampe urna</i>	<i>Theocampe urna</i>	~87.5	1
Turonian			
FO <i>Crucella cachensis</i>	<i>Crucella cachensis</i>	~93.5	2
FO <i>Pseudodictyomitra nakasekoi</i>	<i>Pseudodictyomitra nakasekoi</i>	~98.0	2
FO <i>Obesacapsula somphedia</i>	<i>Obesacapsula somphedia</i>		
Albian			
FO <i>Dorypyle? anisa</i>	<i>Dorypyle? anisa</i>	~99.0	2
FO <i>Pseudodictyomitra pseudomacrocephala</i>	<i>Pseudodictyomitra pseudomacrocephala</i>	~102.0	2
FO <i>Mita spoletensis</i>	<i>Mita spoletensis</i>	107.0–105.0	2
FO <i>Mita gracilis</i>	<i>Mita gracilis</i>	112.2	2
FO <i>Obesacapsula somphedia</i>	<i>Obesacapsula somphedia</i>	~99.0	1
Aptian			
FO <i>Pseudodictyomitra lodogaensis</i>	<i>Pseudodictyomitra lodogaensis</i>	116.0–115.0	2
LO <i>Sphaerostylus lanceola</i>	<i>Acaeniotyle umbilicata</i>	116.0–115.0	1

Notes: FO = first occurrence, LO = last occurrence. References: 1 = Sanfilippo and Riedel (1985), 2 = Erbacher and Thurow (1998).

Table T7. Magnetic polarity timescale for the Late Cretaceous and Cenozoic. (See table notes. Continued on next page.)

Polarity chron/ subchron	Normal polarity interval (Ma)		Epoch, stage (approximate)	Reference	Comments
	Top	Bottom			
C1n	0.000	0.780	Pleistocene	1	Brunhes (Chron C1r–Matuyama)
C1r.1n	0.990	1.070	Pleistocene	1	Jaramillo
C1r.2n	1.201	1.211	Pleistocene	1	Cobb Mountain
C2n	1.770	1.950	Pliocene, Piacenzian	1	Olduvai
C2r.1n	2.140	2.150	Pliocene, Piacenzian	Adjusted 5	Reunion
C2An.1n	2.581	3.040	Pliocene, Piacenzian	1, 2	Gauss Normal (all Chron C2An); subdivided by brief reversed polarity intervals Kaena (Subchron 2An.1r) and Mammoth (Subchron 2An.2r)
C2An.2n	3.110	3.220	Pliocene, Piacenzian	2	
C2An.3n	3.330	3.580	Pliocene, Piacenzian	2	
C3n.1n	4.180	4.290	Pliocene, Zanclean	2	Cochiti Normal (in Gilbert Reversed, which spans Chrons C2Ar–C3r)
C3n.2n	4.480	4.620	Pliocene, Zanclean	2	Nunivak Normal
C3n.3n	4.800	4.890	Pliocene, Zanclean	2	Sidufjall Normal
C3n.4n	4.980	5.230	Pliocene, Zanclean	2, 4	Thvera Normal
C3An.1n	5.875	6.122	Miocene, Messinian	4	5 has slightly different ages for the set calibrated by 4
C3An.2n	6.256	6.555	Miocene, Messinian	4	
C3Bn	6.919	7.072	Miocene, Messinian	4	
C3Br.1n	7.135	7.170	Miocene, Tortonian	4	
C3Br.2n	7.341	7.375	Miocene, Tortonian	4	
C4n.1n	7.406	7.533	Miocene, Tortonian	4	
C4n.2n	7.618	8.027	Miocene, Tortonian	4	
C4r.1n	8.174	8.205	Miocene, Tortonian	4	
C4An	8.631	8.945	Miocene, Tortonian	4	
C4Ar.1n	9.142	9.218	Miocene, Tortonian	4	
C4Ar.2n	9.482	9.543	Miocene, Tortonian	4	
C5n.1n	9.639	9.880	Miocene, Tortonian	4	
C5n.2n	9.920	10.839	Miocene, Tortonian	4	
C5r.1n	10.943	10.991	Miocene, Tortonian	4	
C5r.2n	11.343	11.428	Miocene, Serravalian	4	
C5An.1n	11.841	11.988	Miocene, Serravalian	4	
C5An.2n	12.096	12.320	Miocene, Serravalian	4	
C5Ar.1n	12.605	12.637	Miocene, Serravalian	4	
C5Ar.2n	12.705	12.752	Miocene, Serravalian	4	
C5AAn	12.929	13.083	Miocene, Serravalian	4	
C5ABn	13.252	13.466	Miocene, Serravalian	4	
C5ACn	13.666	14.053	Miocene, Serravalian	4	
C5ADn	14.159	14.607	Miocene, Serravalian	4	
C5Bn.1n	14.800	14.888	Miocene, Langhian	4, 5	14.8 Ma for base of Chron C5ADr is an age control point of 5
C5Bn.2n	15.034	15.155	Miocene, Langhian	5	
C5Cn.1n	16.014	16.293	Miocene, Langhian	5	
C5Cn.2n	16.327	16.488	Miocene, Langhian	5	
C5Cn.3n	16.556	16.726	Miocene, Burdigalian	5	
C5Dn	17.277	17.615	Miocene, Burdigalian	5	
C5En	18.281	18.781	Miocene, Burdigalian	5	
C6n	19.048	20.131	Miocene, Burdigalian	5	
C6An.1n	20.518	20.725	Miocene, Aquitanian	5	
C6An.2n	20.996	21.320	Miocene, Aquitanian	5	
C6AAn	21.768	21.859	Miocene, Aquitanian	5	
C6AAr.1n	22.151	22.248	Miocene, Aquitanian	5	
C6AAr.2n	22.459	22.493	Miocene, Aquitanian	5	
C6Bn.1n	22.588	22.750	Miocene, Aquitanian	5	
C6Bn.2n	22.804	23.069	Miocene, Aquitanian	5	
C6Cn.1n	23.353	23.535	Miocene, Aquitanian	5	
C6Cn.2n	23.677	23.800	Miocene, Aquitanian	5	23.8 Ma (Eocene/Oligocene boundary) at base of Subchron C6Cn.2n is an age control point of 5
C6Cn.3n	23.999	24.118	Oligocene, Chattian	5	
C7n.1n	24.730	24.781	Oligocene, Chattian	5	
C7n.2n	24.835	25.183	Oligocene, Chattian	5	
C7An	25.496	25.648	Oligocene, Chattian	5	
C8n.1n	25.823	25.951	Oligocene, Chattian	5	
C8n.2n	25.992	26.554	Oligocene, Chattian	5	
C9n	27.027	27.972	Oligocene, Chattian	5	
C10n.1n	28.283	28.512	Oligocene, Chattian	5	
C10n.2n	28.578	28.745	Oligocene, Rupelian	5	
C11n.1n	29.401	29.662	Oligocene, Rupelian	5	
C11n.2n	29.765	30.098	Oligocene, Rupelian	5	
C12n	30.479	30.939	Oligocene, Rupelian	5	
C13n	33.058	33.545	Oligocene, Rupelian	5	33.7 Ma for Subchron C13r.85 is an age control point of 5

Table T7 (continued).

Polarity chron/ subchron	Normal polarity interval (Ma)		Epoch, stage (approximate)	Reference	Comments
	Top	Bottom			
C15n	34.655	34.940	Eocene, Priabonian	5	Chron C14 does not exist
C16n.1n	35.343	35.526	Eocene, Priabonian	5	
C16n.2n	35.685	36.341	Eocene, Priabonian	5	
C17n.1n	36.618	37.473	Eocene, Priabonian	5	
C17n.2n	37.604	37.848	Eocene, Bartonian	5	
C17n.3n	37.920	38.113	Eocene, Bartonian	5	
C18n.1n	38.426	39.552	Eocene, Bartonian	5	
C18n.2n	39.631	40.130	Eocene, Bartonian	5	
C19n	41.257	41.521	Eocene, Lutetian	5	
C20n	42.536	43.789	Eocene, Lutetian	5	
C21n	46.264	47.906	Eocene, Lutetian	5	46.8 Ma at upper Chron C21n (Subchron C21n.67) is an age control point of 5
C22n	49.037	49.714	Eocene, Ypresian	5	
C23n.1n	50.778	50.946	Eocene, Ypresian	5	
C23n.2n	51.047	51.743	Eocene, Ypresian	5	
C24n.1n	52.364	52.663	Eocene, Ypresian	5	
C24n.2n	52.757	52.801	Eocene, Ypresian	5	
C24n.3n	52.903	53.347	Eocene, Ypresian	5	
C25n	55.904	56.391	Paleocene, Thanetian	5	
C26n	57.554	57.911	Paleocene, Thanetian	5	Selandian stage is approximately equivalent to Chron C26r (6)
C27n	60.920	61.276	Paleocene, Danian	5	
C28n	62.499	63.634	Paleocene, Danian	5	
C29n	63.976	64.745	Paleocene, Danian	5	65.0 Ma at Subchron C29r.7 (Maastrichtian/Paleocene boundary) is an age control of 5
C30n	65.578	67.610	Maastrichtian	5	
C31n	67.735	68.737	Maastrichtian	5	
C32n.1n	71.071	71.338	Maastrichtian	5	
C32n.2n	71.587	73.004	Campanian	5	
C32r.1n	73.291	73.374	Campanian	5	
C33n	73.619	79.075	Campanian	5	
C34n	83.000		Santonian to Aptian	5	83.0 Ma at base of Chron C33r (base of Campanian) is an age control of 5

Notes: Ages of polarity chrons are from compilations published before 1995 but were retained to be consistent with the biostratigraphic age scales during Leg 207 (see "Biostratigraphy," p. 8). References: 1 = Shackleton et al. (1990), 2 = Hilgen (1991a), 3 = Hilgen (1991b), 4 = Shackleton et al. (1995), 5 = Cande and Kent (1995), 6 = Berggren et al. (1995b).

Table T8. Example of composite depth table found in each site chapter.

Core	Depth (mbsf)	Offset (m)	Depth (mcd)	Moved
207-1258A-				
1R	0.0	0.00	0.00	N
2R	5.1	0.00	5.10	N
3R	14.2	0.00	14.20	N
4R	23.8	0.00	23.80	N
5R	33.2	4.50	37.70	Y
6R	42.8	0.52	43.32	Y
7R	52.5	0.99	53.49	Y
8R	62.2	1.85	64.05	Y
9R	71.9	0.25	72.15	Y
10R	81.6	0.63	82.23	Y
11R	91.3	-0.30	91.00	Y
12R	100.9	0.39	101.29	Y
13R	110.5	0.61	111.11	Y
207-1258B-				
1R	0.0	2.90	2.90	Y
2R	14.1	0.00	14.10	N
3R	23.1	0.00	23.10	N
4R	32.1	0.00	32.10	N
5R	41.1	0.10	41.20	Y
6R	50.8	-0.57	50.23	Y
7R	60.5	-0.01	60.49	Y
8R	70.1	-0.47	69.63	Y
9R	79.7	-0.83	78.87	Y
10R	89.3	-0.67	88.63	Y
11R	99.0	-0.37	98.63	Y
12R	108.6	0.60	109.20	Y

Note: N = no, Y = yes.

Table T9. Example of splice tie point table found in each site chapter.

Hole, core, section, interval (cm)	Depth			Hole, core, section, interval (cm)	Depth	
	(mbsf)	(mcd)			(mbsf)	(mcd)
207-				207-		
1258B-4R-5, 5	38.15	38.15	Tie to	1258A-5R-1, 45	33.65	38.15
1258A-5R-4, 7.5	37.78	42.28	Tie to	1258B-5R-1, 107.5	42.18	42.28
1258B-5R-4, 52.5	46.13	46.23	Tie to	1258A-6R-2, 139.5	45.71	46.23
1258A-6R-6, 80	51.10	51.62	Tie to	1258B-6R-1, 138.5	52.19	51.62
1258B-6R-3, 127.5	55.08	54.51	Tie to	1258A-7R-1, 101	53.52	54.51
1258A-7R-6, 7.5	59.78	60.77	Tie to	1258B-7R-1, 27.5	60.78	60.77
1258B-7R-5, 50	67.00	66.99	Tie to	1258A-8R-2, 147	65.14	66.99
1258A-8R-5, 20	68.37	70.22	Tie to	1258B-8R-1, 58.5	70.69	70.22
1258B-8R-3, 25	73.35	72.88	Tie to	1258A-9R-1, 72.5	72.63	72.88
1258A-9R-7, 35	81.25	81.50	Tie to	1258B-9R-2, 112.5	82.33	81.50
1258B-9R-3, 145	84.15	83.32	Tie to	1258A-10R-1, 108.5	82.69	83.32
1258A-10R-6, 15	89.25	89.88	Tie to	1258B-10R-1, 125	90.55	89.88
1258B-10R-3, 95	93.25	92.58	Tie to	1258A-11R-2, 7.5	92.88	92.58
1258A-11R-6, 90	99.65	99.35	Tie to	1258B-11R-1, 71	99.72	99.35
1258B-11R-4, 45	103.95	103.58	Tie to	1258A-12R-2, 78.5	103.19	103.58
1258A-12R-6, 117.5	109.58	109.97	Tie to	1258B-12R-1, 76	109.37	109.97
1258B-12R-2, 95	111.05	111.65	Tie to	1258A-13R-1, 53.5	111.04	111.65
1258A-13R-5, 140	117.90	118.51	Tie to	1258B-13R-1, 91	119.12	118.51

Table T10. Reproducibility for analytical determinations, Leg 207.

Parameter	Method	Reproducibility
Alkalinity	Gran titration	±1.5%
Cl ⁻	Titration with AgNO ₃	±0.1%
K ⁺	ICP-AES	±0.02%
Mg ²⁺	ICP-AES	±0.1%
Ca ²⁺	ICP-AES	±0.2%
SO ₄ ²⁻	Ion chromatography	±0.1%
Si(OH) ₄	Spectrophotometry	±2 mM
NH ₄ ⁺	Spectrophotometry	±4 mM
HPO ₄ ²⁻	Spectrophotometry	±0.2 mM
Fe ²⁺	ICP-AES	±2.3%
Mn ²⁺	ICP-AES	±2.3%
B	ICP-AES	±2.4%
Li ⁺	ICP-AES	±4.4%
Sr ²⁺	ICP-AES	±1.0%
Ba ²⁺	ICP-AES	±1.1%

Note: ICP-AES = inductively coupled plasma–atomic emission spectroscopy.

Table T11. MST sampling frequencies, Leg 207.

Hole, core, section	Sensor data frequency (cm)				
	MS	GRA	PWL	NCR	NGR
207-					
1257A-1H-5H	2.5	2.5	2.5	2.5	NM
1257A-6X-31X	2.5	2.5	NM	2.5	15.0
1257B-1R-27R	2.5	2.5	NM	2.5	7.5
1257C-1R-16R	2.5	2.5	NM	2.5	7.5
1258A-1R-50R	2.5	2.5	NM	2.5	7.5
1258B-1R-57R	2.5	2.5	NM	2.5	7.5
1258C-1R-34R	2.5	2.5	NM	2.5	7.5
1259A-1R-60R	2.5	2.5	NM	2.5	7.5
1259B-1R-25R	2.5	2.5	NM	NM	7.5
1260A-1R-27R-3	2.5	2.5	NM	2.5	7.5
1260A-27R-4-54R	2.5	2.5	NM	NM	7.5
1260B-1R-2R	2.5	2.5	NM	2.5	7.5
1260B-3R-12R-2	2.5	2.5	NM	2.5	15.0
1260B-12R-3-46R	2.5	2.5	NM	2.5	7.5
1261A-1R-51R	2.5	2.5	NM	2.5	7.5
1261B-1R-16R	2.5	2.5	NM	2.5	7.5

Note: MS = magnetic susceptibility, GRA = gamma ray attenuation bulk density, PWL = P-wave logger, NCR = noncontact resistivity, NGR = natural gamma ray. NM = not measured.

Table T12. Salinity standards used for the NCR calibration, Leg 207.

Salinity standards	Average NCR sensor output (mV)	Resistivity (Ωm)	
		NaCl solution resistivity at 20°C*	Leg 204 calibration curve†
35.5	0.64464	0.1986	0.1863
30.5	0.56268	0.2290	0.2169
25.0	0.44268	0.2760	0.2838
18.5	0.35228	0.3661	0.3660
15.0	0.25822	0.4457	0.5191

Notes: NCR = noncontact resistivity. * = resistivity calculated from power curve relating salinity of NaCl solutions to resistivity (data taken Carmichael, 1982). † = power curve calibration calculated during Leg 204 (see Tréhu, Bohrmann, Rack, Torres, et al., 2003 for a full description of the Leg 204 calibration curve). Resistivity (Ωm) = $261 \times (\text{mV} \times 1000)^{-1.12}$.

Table T13. Calibration of NCR sensor.

Distance from core liner (mm)	NCR output (mV)
2.5	0.286
6.0	0.199
8.0	0.438
10.2	0.390
12.8	0.337
14.5	0.449
16.9	0.284
24.2	0.195

Note: NCR = noncontact resistivity; resistivity changes as an inverse of the mV response of the sensor.

Table T14. Measurements made by the wireline tool strings.

Tool string	Tool	Measurement	Sampling interval (cm)	Approximate vertical resolution (cm)
Triple combination	HNGS	Spectral gamma ray	15	51
	APS	Porosity	5 and 15	43
	HLDT	Bulk density	2.5 and 15	38
	DIT	Resistivity	15	76, 150, 200
	TAP	Temperature	1 per s	NA
		Tool acceleration	4 per s	NA
		Pressure	1 per s	NA
	MGT	Gamma ray	15	15
Formation MicroScanner (FMS)-sonic combination	FMS	Microresistivity	0.25	0.5
	GPIT	Tool orientation	0.25 and 15	NA
	SGT	Total gamma ray	15	NA
	LSS	Acoustic velocity	15	61
WST (stationary measurement)	WST*	Sonic traveltime	Variable	NA

Notes: All tool and tool string names (except the TAP and MGT) are trademarks of Schlumberger. For the complete list of acronyms used in the ODP and for additional information about tool physics and use consult ODP Logging Services at www.ideo.columbia.edu/BRC/ODP. See Table T15, p. 94, for explanation of acronyms used to describe tool strings and tools. NA = not applicable. * = not included on every run.

Table T15. Acronyms and units used for wireline logging tools.

Tool	Output	Tool name/Explanation of output	Unit
APS		Accelerator Porosity Sonde	
	APLC	Near array porosity (limestone calibrated)	%
	SIGF	Formation capture cross section (Σ_p)	Capture units
	STOF	Tool standoff (computed distance from borehole wall)	in
DIT		Dual Induction Tool	
	IDPH	Deep induction resistivity	Ωm
	IMPH	Medium induction resistivity	Ωm
	SFLU	Spherically focused resistivity	Ωm
FMS		Formation MicroScanner	
	C1, C2	Orthogonal hole diameters	in
	P1AZ	Pad 1 azimuth	Degrees
		Spatially oriented resistivity images of borehole wall	
GPIT		General Purpose Inclinerometer Tool	
	DEVI	Hole deviation	Degrees
	HAZI	Hole azimuth	Degrees
	F_x, F_y, F_z	Earth's magnetic field (three orthogonal components)	Oersted
	A_x, A_y, A_z	Acceleration (three orthogonal components)	m/s^2
HLDT		Hostile Environment Litho-Density Tool	
	RHOM	Bulk density	g/cm^3
	PEFL	Photoelectric effect	b/e^-
	LCAL	Caliper (measure of borehole diameter)	in
	DRH	Bulk density correction	g/cm^3
HNGS		Hostile Environment Gamma Ray Sonde	
	HSGR	Standard (total) gamma ray	gAPI
	HCGR	Computed gamma ray (HSGR minus uranium contribution)	gAPI
	HFK	Potassium	wt%
	HTHO	Thorium	ppm
	HURA	Uranium	ppm
LSS		Long Spacing Sonic tool	
	DT	Short-spacing delay time (Δt)	$\mu\text{s/ft}$
	DTL	Long-spacing delay time (Δt)	$\mu\text{s/ft}$
MGT		Multi-Sensor Spectral Gamma Ray Tool	
	GR	Total gamma ray	gAPI
	POTA	Potassium	wt%
	THOR	Thorium	ppm
	URAN	Uranium	ppm
SGT		Scintillation Gamma Ray Tool	
	ECGR	Environmentally corrected gamma ray	gAPI
TAP		Temperature/Acceleration/Pressure tool	$^{\circ}\text{C}$, m/s^2 , psi
WST		Well Seismic Tool	
		Acoustic arrival times	ms

Notes: All tool and tool string names (except the TAP and MGT) are trademarks of Schlumberger. For the complete list of acronyms used in the ODP and for additional information about tool physics and use consult ODP Logging Services at www.ideo.columbia.edu/BRG/ODP.